MODELING THE RESPONSE OF PREMIXED FLAMES TO FLOW DISTURBANCES

A Dissertation
Presented to
The Academic Faculty

by

Preetham

In Partial Fulfillment
of the Requirements for the Degree
Doctor of Philosophy in
Aerospace Engineering

Georgia Institute of Technology

December 2007

MODELING THE RESPONSE OF PREMIXED FLAMES TO FLOW DISTURBANCES

Approved By:

Dr. Tim Lieuwen, Advisor
Associate Professor
School of Aerospace Engineering
Georgia Institute of Technology

Dr. Ben T. Zinn
Regents Professor, David S. Lewis Chair
School of Aerospace Engineering
Georgia Institute of Technology

Dr. Suresh Menon
Professor
School of Aerospace Engineering
Georgia Institute of Technology

Dr. Lakshmi Sankar
Regents Professor, Associate Chair for Undergraduate Programs
School of Aerospace Engineering
Georgia Institute of Technology

Dr. Fei Han
Combustion Dynamics Group
G. E. Global Research Centre

Date Approved: 19 September 2007

To my parents

"Do, or do not. There is no try."

--*Jedi Master Yoda*

ACKNOWLEDGEMENTS

I would like to express my deepest gratitude to my advisor, Dr. Tim Lieuwen for his invaluable guidance and mentoring throughout this research work. Besides all the research experience which I have gained, Tim has also provided me with every bit of encouragement possible to fructify my career plans. It has been an honor to work with him.

I would also like to thank Dr. Suresh Menon, Dr. B.T. Zinn, Dr. Lakshmi Sankar and Dr. Fei Han for their helpful comments and for taking an active part in my thesis committee. Thanks are also due to Dr. Shiva Srinivasan, Dr. Kwanwoo Kim, Dr. Kapil Singh and Dr. Fei Han for giving me an opportunity to work on exciting projects as an intern at GE Energy and GE Global Research.

I would like to thank the following in the Ben T. Zinn Combustion Lab for their help, friendship and support: Santosh H., Santosh S., Jayaprakash, Bobba, Jackie, Nelson, Satish, Rajesh, Qingguo, Priya, Antonio, Ben, Sai, Bobby, Yash, Arun, Shashvat, Murgi, Suraj, Nori, Shreekrishna, Tom and Thao. I would also like to thank my friends: Kapil, Rajeev, Mudhakar, Karan, Tunga and Vishwas for making my stay in Atlanta memorable.

Finally, I am forever indebted to my parents, Kanthi Subramanyam and L. Balasubramanyam, for their love and concern, which encouraged me at every step in my life. Everything I am today is due to the sacrifices that my parents made, the constant encouragement I received and the confidence they had in me. Special thanks are also due to my sister, Preethi, for her encouragement and good humour and to Deepika, for her love and support.

TABLE OF CONTENTS

LIST OF FIGURES

NOMENCLATURE

A_c', A_w'	fluctuating conical/wedge flame area
$\bar{A}_c$, $\bar{A}_w$	steady state conical/wedge flame area
G_c,G_w	conical/wedge flame area -velocity transfer function
k	convective wave number $\equiv \omega_o/u_c$
K	parameter$\equiv u_o/u_c$
L_f	steady state flame length
L_{avg}	time averaged (nondimensionalized) flame length
M_a	Markstein length
$\bar{Q}$	steady state heat release
Q'	fluctuating heat release
r	instantaneous (dimensionless) radial location
R	burner radius
St	Strouhal number$\equiv \omega_o L_f/u_o$
St_2	reduced Strouhal number, Eq. (42)
St_c	convective Strouhal number, Eq. (44)
$S_{L,o}$	Unstretched laminar burning velocity
t	nondimensional time
u_o	mean axial flow velocity at the inlet
u_c	disturbance propagation velocity
u	axial velocity
u'	fluctuating axial velocity

Greek Symbols

α parameter, defined in Eq. (37)

β flame aspect ratio$\equiv L_f/R$

ε nondimensionalized fluctuating (axial) velocity amplitude$\equiv u'/u_o$

ε_f ε value at flashback, defined in Eq. (31)

η parameter$\equiv K\alpha$

$\sigma_{c,s}$ nondimensionalized Markstein length related to curvature and strain, see Eqs. (65) and (66)

τ acoustic time period

ω_o excitation frequency

ρ density

ζ instantaneous flame position (nondimensionalized), Eq. (33)

ζ_o, ζ_1, ζ_2, ζ_3 functions, defined in Eq. (33)

SUMMARY

Low emissions combustion systems for land based gas turbines rely on a premixed or partially premixed combustion process. These systems are exceptionally prone to combustion instabilities which are destructive to hardware and adversely affect performance and emissions. The success of dynamics prediction codes is critically dependent on the heat release model which couples the flame dynamics to the system acoustics. So the principal objective of the current research work is to predict the heat release response of premixed flames and to isolate the key non-dimensional parameters which characterize its linear and nonlinear dynamics.

This thesis addresses three outstanding issues in the course of providing a systematic treatment of the linear and nonlinear dynamics of laminar premixed flames. Specifically, this study elucidates the role of the *disturbance field characteristics* in determining the *nonlinear* flame response. From a theoretical point of view, this is important as most models to date have assumed a uniform disturbance velocity field while studying non-linear effects (in contrast to experimental evidence) and as such are missing a key component of the physics. It is shown that the linear and nonlinear characteristics of the flame dynamics are controlled by the superposition of two sources of flame disturbances: those originating at the flame anchoring point due to boundary conditions and from flow non-uniformities along the flame. Consequently, they may either constructively or destructively superpose, so that the overall linear flame response depends upon two Strouhal numbers, St_2 and St_c, related to the amount of time taken for a flow (St_c) and flame front (St_2) disturbance to propagate the flame length, normalized by

the acoustic period. Because the overall flame response is a *superposition* of the two flame disturbance contributions, the flame's nonlinear response exhibits two qualitatively different behaviors. For parameter values where these disturbances *constructively interfere*, the nonlinear flame response *saturates*. When the flame disturbances *destructively interfere*, the nonlinear transfer function may actually *exceed its linear value* before *saturating*. This result explains the experimentally observed variation of the nonlinear flame response with frequency and has implications of the type of *bifurcations* which may be observed in *unstable* combustors. In situations where the nonlinear gain is always less than one, only *supercritical bifurcations* will occur leading to a single *stable limit cycle* amplitude. In situations where the gain exceeds, then is less than, the linear gain, *multiple stable solutions* for the instability amplitude may exist, and *sub-critical bifurcations* are possible. Such a system will manifest characteristics such as *hysteresis* and *triggering* (i.e., the destabilization of a linearly stable system by a sufficiently large disturbance).

Secondly, this study presents the *first analytical model* which captures the effects of *unsteady flame stretch* on the heat release response. Prior analytical studies were limited to planar flames and as such were inadequate to understand the dynamics of anchored flames. Since acoustic forcing introduces flame wrinkles whose length inversely scales with disturbance frequency, stretch induced flame speed variations become significant at high frequencies. Flame stretch effects, characterized by the non-dimensionalized Markstein length (σ_c^*), are found to become important as the disturbance frequency satisfies $\sigma_c^* St_2^2 \sim O(1)$, i.e. $St_2 \sim O\left((\sigma_c^*)^{-1/2}\right)$. Specifically, for disturbance frequencies below this order, stretch effects are small such that the flame acts

as an unstretched one. When the disturbance assumes $O(1)$ of this frequency, the transfer function, defined as the ratio of the normalized fluctuation of the heat release rate to that of velocity, is contributed mostly from fluctuations of the *flame surface area*, which is *now affected by stretch*. As the disturbance frequency increases to that of $St_2 \sim O\left((\sigma_c^*)^{-1}\right)$, i.e. $\sigma_c^* St_2 \sim O(1)$, the direct contribution from the *stretch-affected flame speed fluctuation* to the transfer function becomes *comparable* to that of the *flame surface area*. The present study qualitatively explains the *experimentally* observed "*filtering effect*" in which the flame wrinkles developed at the flame base decay along the flame surface for thermal-diffusively stable mixtures and for large frequencies disturbances.

Finally, there have been limited studies to explicitly understand as to how the *temperature jump across the flame* (resulting in a coupling between the flame and the unsteady flow field) alters the approach flow disturbance characteristics, as well as those of the flame dynamics itself. This issue has been addressed by developing an unsteady, compressible, coupled Euler-G-equation solver with a Ghost Fluid Method (GFM) module for applying the jump conditions across the flame. The analysis yields insight into the significant spatial dependence of the perturbation velocity field induced by the coupling between the flame and the flow field. Moreover, the acceleration of the mean flow due to gas expansion causes the effective residence time of the flame wrinkles to vary with T_b/T_u although the flame has the same frequency of forcing, approach flow velocity and mean flame length. These factors cause the heat release transfer function gains to show a strong dependence on T_b/T_u when the flame base excitation amplitude is used as the reference velocity and the Strouhal number is based on the mean inlet

velocity. To understand this significant variation with T_b/T_u, a theoretical analysis is developed to capture the effect of spatial non-uniformity of the mean and disturbance flow-field characteristics on the flame response. An explicit analytical expression is obtained for the *effective Strouhal number* controlling the flame response. It also yields insight to determine an effective *reference velocity* for defining heat release transfer functions which can then be *consistently compared across* T_b/T_u. Once the gains across T_b/T_u are corrected for the effective Strouhal number and reference velocity magnitude, good agreement is obtained with the gain predictions from constant density theory.

CHAPTER 1

INTRODUCTION

1.1 Motivation

Modern land based gas turbine manufacturers are increasingly moving towards a premixed mode of combustor operation. This operational shift and the subsequent design changes have been primarily driven by the strict emission guidelines on pollutants like NO_x and CO. One of the principal strategies adopted to satisfy these emission norms is to burn the fuel-air mixture at lean equivalence ratios. At lean conditions, the production of thermal NO_x is greatly reduced due to the lowered temperatures. However, one major drawback of lean, premixed operation is that these combustors are especially prone to self excited oscillations. This dynamic phenomenon generally occurs when the unsteady combustion process couples with the natural acoustic modes of the combustor. These instabilities are destructive to hardware (see Figure 1) and adversely affect performance and emissions [1,2,3,4,5].

1.2 Background

The condition under which acoustic oscillations are amplified by a fluctuating source of heat release was first postulated by Lord Rayleigh [6]. Rayleigh's criterion essentially states that the instabilities in a combustor are driven when the unsteady combustion processes add energy in phase to the acoustic oscillations. In general, this instability is sustained if the rate at which the energy is added to the acoustic oscillations is greater than the rate at which the acoustic energy is absorbed. Essentially, a perturbation in a

flow variable causes a change in the flame heat release rate. Subsequently, this unsteadiness in the flame heat release generates acoustic waves. The feedback loop is completed when these acoustic waves cause further changes in the flow variables. In a typical combustor, this feedback mechanism can be completed by a variety of driving processes [4] (see Figure 2) like equivalence ratio oscillations, velocity oscillations, flame extinction, vortex dynamics, flame wall interaction etc. Depending on the operating conditions, one or more of these mechanisms may be driving the oscillations. The current approach has been to develop simple experiments/models in order to isolate and highlight the key physics behind each of these driving processes [7].

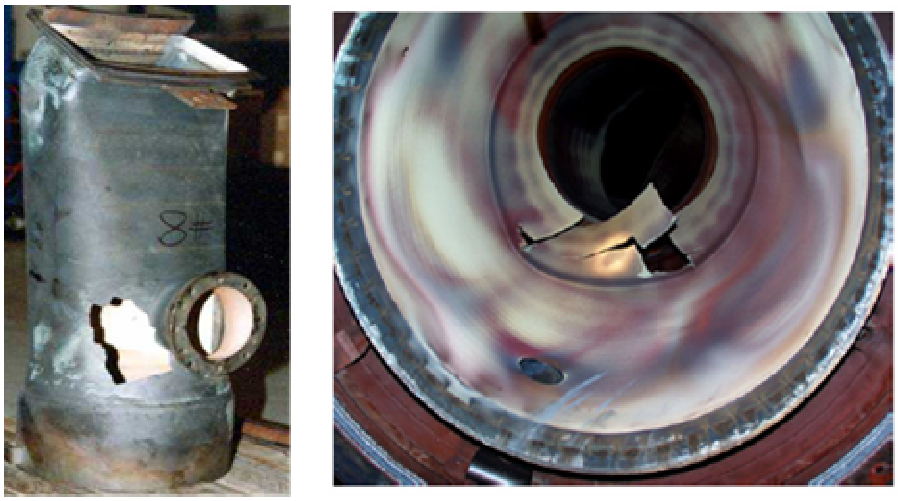

Figure 1 Illustration of the detrimental effects caused by combustion instabilities. The image on the left corresponds to a damaged transition piece while the one on the right is a failed combustion liner.

When the perturbations are infinitesimally small, the system dynamics can be analyzed using linear acoustics. Apart from predicting the frequency and growth rate of the oscillations, the linearized analysis also provides information about the operating conditions under which the system may be unstable. From a practical standpoint, gas turbine manufacturers are not only interested in the unstable frequencies but also in the

limit cycle amplitude of the instability. This is because an "acceptable/unacceptable threshold" of the instability amplitude (based on the potential to damage hardware or affect performance) is strongly dependent on the frequency. For example, a 2 psi peak to peak instability amplitude may have greater potential to cause hardware damage at 1000 HZ than at 100 Hz.

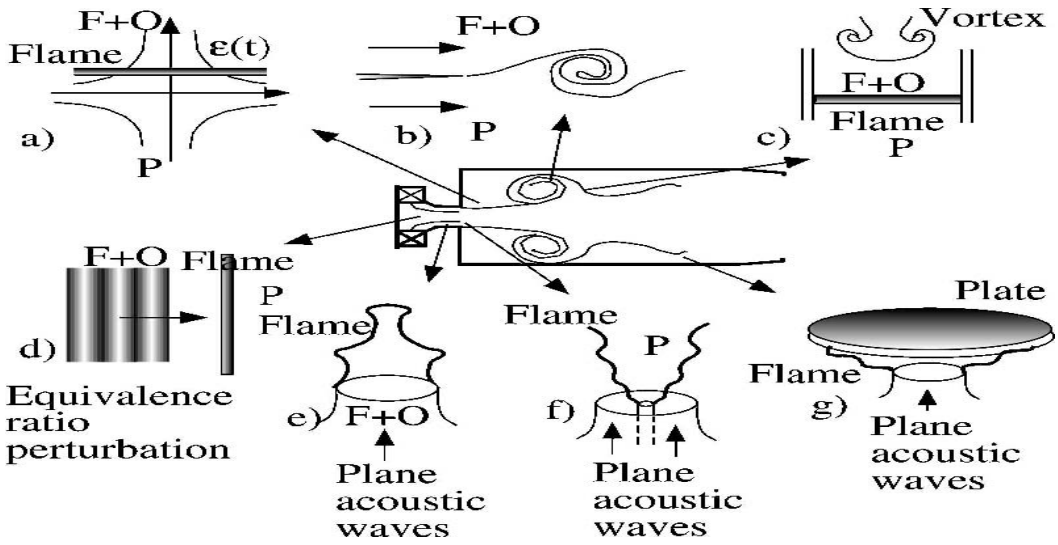

Figure 2 Illustration of the elementary processes responsible for driving combustion instabilities [4].

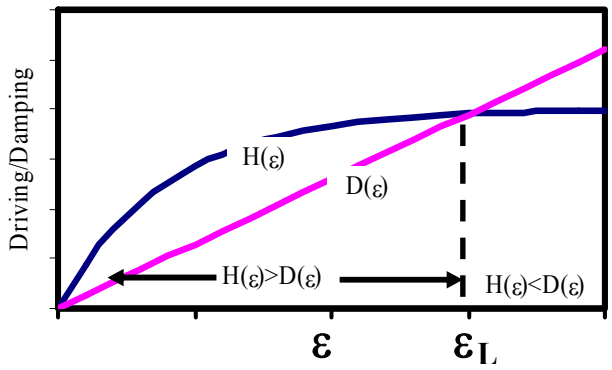

Figure 3 Qualitative description of the dependence of acoustic driving, $H(\varepsilon)$ and damping, $D(\varepsilon)$, processes upon amplitude, ε. Figure reproduced from Lieuwen [21].

However, the limit cycle amplitude attained in an unstable combustor is determined by

nonlinear processes and hence cannot be captured by a linear analysis. To illustrate this point, consider an acoustic disturbance with amplitude, ε. Referring to Figure 3, note that this disturbance amplitude stays the same, decreases, or increases depending upon the relative magnitudes of the driving, $H(\varepsilon)$, and damping, $D(\varepsilon)$, processes; i.e., whether $H(\varepsilon)=D(\varepsilon)$, $H(\varepsilon)<D(\varepsilon)$, or $H(\varepsilon)>D(\varepsilon)$, respectively. Linear combustor processes generally control the balance between driving and damping processes at low amplitudes of oscillation and, thus, determine the growth rate of inherent disturbances in the combustor. Nonlinear combustor processes control the finite amplitude dynamics of the oscillations. Predicting the limit cycle amplitude of self-excited oscillations requires an understanding of the nonlinear characteristics of $H(\varepsilon)$ and $D(\varepsilon)$. To illustrate, Figure 3 depicts a situation where $H(\varepsilon)$ saturates and the two curves cross at the limit cycle amplitude, ε_{LC}.

The focus of this thesis is on the heat release dynamics, i.e., to understand the characteristics of $H(\varepsilon)$ in both the linear and nonlinear regime. This focus on heat release dynamics is motivated by observations that the nonlinear gas dynamical processes are less significant in many premixed combustors. For example, Dowling [8] suggests that gas dynamic processes essentially remain in the linear regime, even under limit cycle operation, and that it is the relationship between flow and heat release oscillations that provides the dominant nonlinear dynamics in premixed combustors, i.e., $H(\varepsilon)$. The primary point of these observations have been confirmed by several experimental studies [9,10,11], which show that substantial nonlinearities in the heat release response to acoustic disturbances occur, even at amplitudes as low as $p'/p_o \sim 1\%$ and $u'/u_o \sim 20\%$.

A variety of mechanisms exist for causing nonlinearities in heat release dynamics; e.g., local or global flame extinction [8,12], pressure sensitivity of the mass burning rate [13,14,15,16], flame holding and/or nonlinear boundary conditions (e.g., the point where the flame anchors depending upon amplitude, [17]), equivalence ratio oscillations [11,18], and flame kinematics [17, 19, 20, 21]. For example, at high amplitudes of flow oscillations, strain rates may reach the extinction limit and consequently extinguish the flame locally. Unsteady extinction and re-ignition of local or global regions of the flame causes the unsteady heat release amplitude to vary nonlinearly with velocity. Dowling [8] developed a phenomenological model to emphasize the role of global flame extinction on the finite amplitude response of a ducted flame to velocity perturbations. The key source of nonlinearity in the model is the relationship between flow velocity and heat release rate. Essentially, the model assumes a linear relation between the heat release, Q, and velocity perturbation when the total velocity ($u=u_o+u'$) lies between 0 and 2. When $u<0$, the heat release goes to zero and when it is greater than $2u_o$ it saturates at $2Q_o$. Specifically, nonlinearity lies in the fact that the lowest amplitude of heat release oscillation cannot achieve negative values and consequently cannot decrease monotonically with perturbation amplitude.

The oscillatory flow field, especially when the flow disturbances are comparable to the mean flow, introduces another potential source of non linearity in terms of the flame holding characteristics. This issue was first analyzed by Dowling [17], who introduced a nonlinear boundary condition at the flame anchoring point. In the model, the instantaneous flame anchoring point was fixed when the total velocity exceeded the flame speed. When the instantaneous velocity was lower than the flame speed, the flame was

allowed to propagate upstream (perpendicular to the duct walls). The flame shape predictions using this nonlinear boundary condition were found to be consistent with experimental observations.

Perturbations in equivalence ratio, which are generated due to flow oscillations in the premixing section, have been recognized as an important source of combustion instability [19,7,4]. Peracchio and Proscia [18] derived a nonlinear equation ($\phi(t) = \frac{\phi_o}{1 + u'(t)/u_o}$) relating the velocity disturbance and equivalence ratio amplitude. In addition, they introduced a nonlinear relationship relating the heat release per unit mass of mixture to the instantaneous equivalence ratio. Later, Stow and Dowling [22] developed a phenomenological model to account for the nonlinearities in the equivalence ratios when the fluctuating velocities are comparable to the mean flame. In their model, if a fluid particle had previously crossed the flame (assumed compact) at least once in an acoustic cycle, then the instantaneous equivalence ratio (ϕ(t)) was set to zero. Another source of nonlinearity in the model was the change in nominal equivalence ratio when a fluid particle crossed the fuel injector location more than once (due to reverse flow during part of the acoustic cycle). However, this model can not apply to the instantaneous flame sheet location, as the flow passes through the flame-it can apply to the time averaged flame location.

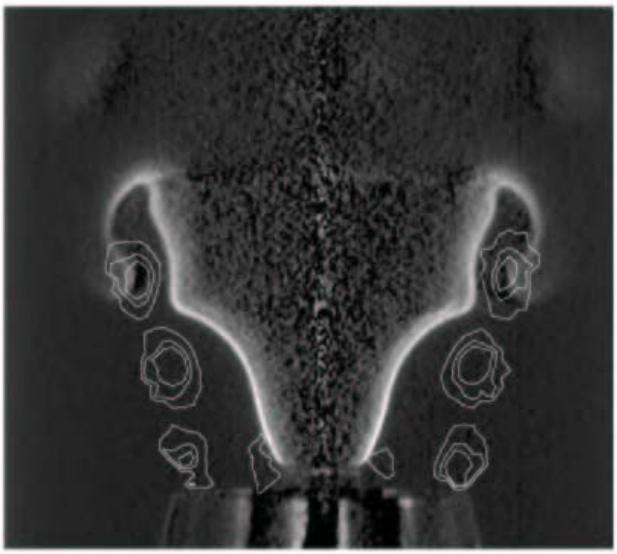

Figure 4 Vorticity field superposed with the flame front. Image reproduced with permission from Durox *et al.* [23]

The *kinematic mechanism*, i.e., the response of the flame front position as it adjusts to perturbations in flow velocity, *is the focus of this thesis*. Because the flame's position and orientation depends upon the local burning rate and flow characteristics, velocity perturbations cause wrinkling and movement of the flame front. In turn, this modifies its local position and curvature, as well as its overall area or volume. These velocity disturbances can be acoustic or vortical in nature and, thus, propagate at the sound speed or with the flow, respectively. To illustrate the excitation of a flame by a velocity disturbance, Figure 4 shows a photograph from Durox *et al*. [23] of a Bunsen flame disturbed by flow oscillations generated by a loudspeaker placed upstream of the flame. The figure clearly shows the large distortion of the flame front. This flame disturbance is convected downstream by the mean flow, so that it varies spatially over a convective wavelength.

A variety of experimental observations have been made of similar flames which will be reviewed next. Baillot and co-workers performed a systematic experimental and

theoretical study of the response of laminar Bunsen flame to velocity perturbations of varying amplitude and frequency [24,25,26]. While their principal observations are quite similar to those previously observed by Blackshear [27], they appear to be the first systematic characterization of the flame response as a function of perturbation amplitude. Figure 5 (reproduced from Bourehla & Baillot [24]) summarizes the response of the oscillating Bunsen flame as a function of the forcing frequency and amplitude. Similar to the illustration in Figure 4, they found that at low frequencies (f<200 Hz) and velocity amplitudes (u'/u_o<0.3), the flame front wrinkles symmetrically about the burner axis due to a convected wave traveling from the burner base to its tip. At higher frequencies, but similar low amplitudes, (region 2 in Figure 5) they observed a phenomenon which they refer to as "filtering" wherein the flame wrinkles are only evident at the flame base and decay with axial location downstream. They did not postulate any mechanisms for this behavior. Unfortunately, they did not publish any photographs of the phenomenon. In Chapter 5, it will be shown that this high frequency behavior is due to the increased importance of the flame's curvature dependent burning velocity and the very short convective wavelengths of the imposed disturbances.

Bourehla & Baillot [24] also found that laminar, conical Bunsen flames subjected to high amplitude, low frequency velocity perturbations exhibited a variety of transient flame holding behavior, such as flashback, asymmetric blow off, unsteady lifting and re-anchoring of the flame (see Figure 5). In addition, they note that its response is asymmetric and extremely disordered. However, at high frequencies and forcing amplitudes, the flame remains firmly attached, but its overall shape dramatically changes. They found that the flame becomes "collapsed" with a rounded off tip region (see regions

6 and 8 in Figure 5), and for sufficiently high forcing intensities ($u'/u_o>1$), the flame's mean shape becomes hemispherical [24]. They also characterized the disturbance velocity field using Laser Doppler Velocimetry (LDV). They measured the phase speed of the convected velocity disturbances and noted its complicated dependence on the Strouhal number and the shear layer characteristics at the base of the flame. Recently, Birbaud *et al.* [28] characterized the upstream flow field of a conical Bunsen flame using Particle Image Velocimetry (PIV) measurements and showed that the upstream flow propagation transitioned from a convective to acoustic mode at low and high Strouhal numbers respectively. By considering a velocity potential associated with the flame motion, this transition in the flow field characteristics was attributed to the upstream influence of the flame wrinkling.

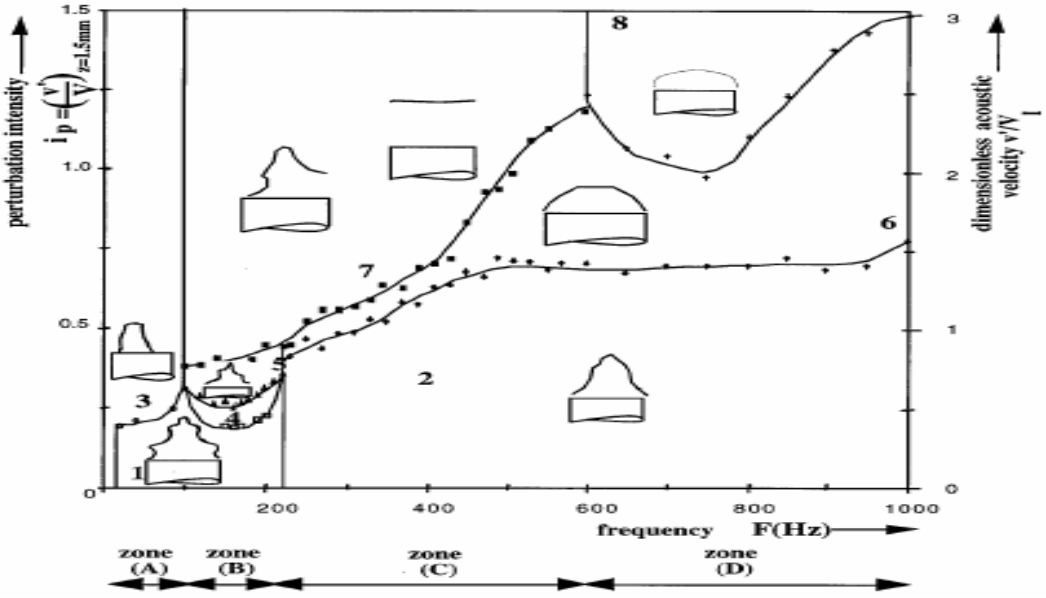

Figure 5 Response chart of oscillating Bunsen flame as a function of forcing amplitude and frequency. Image reproduced from Bourehla & Baillot [24]

Durox *et al*. [23] reported an experimental investigation of the heat release response of unconfined axisymmetric wedge flames to velocity perturbations. They showed that the

flame response was strongly influenced by the vortical structures generated at the shear layer at the flame base. These convecting vortical structures (see Figure 4) interacted strongly with the flame front and controlled the speed with which the cusps moved along the flame front. It was also shown that, in contrast to conical flames, wedge flames could behave as an amplifier at certain frequencies. In a more recent study, Birbaud *et al.* [29] studied the effect of confinement by varying the diameter of the duct bounding an axisymmetric wedge flame. On progressively decreasing the duct diameter (i.e. going from an unconfined to a fully confined flame configuration), the dominant mechanism controlling the flame dynamics shifted from that of flame-vortex interaction to flame-wall interaction. Significantly, in the confined case, the gain was approximately constant (close to unity) regardless of the frequency and amplitude of excitation. This behavior was attributed to the strong interaction of the vortical structures with the wall.

Baillot *et al.* [26] also reported a theoretical study, where they solved the *G*-equation and showed good agreement between predicted and measured flame shapes, even at larger amplitudes of forcing where the flame front becomes strongly cusped. The so-called *G*-equation is a front tracking equation for the flame position, given by:

$$\frac{\partial G}{\partial t} + \vec{u} \bullet \nabla G - S_L \left| \nabla G \right| = 0 \quad (1)$$

where $G(x,t)=0$ is an implicit expression defining the instantaneous flame position, $\vec{u}$ is the velocity field and S_L is the laminar burning velocity.

Solution of the *G*-equation is a key analytical approach used in this thesis for quantitative analysis of this problem. This approach for treating unsteady flame problems was apparently first introduced by Markstein [30] and, in the context of acoustically

forced flames, by Marble & Candel [31]. It has subsequently been extensively developed [32] and is used in a variety of flame dynamic studies. The key assumption behind its application is the separation of acoustic/hydrodynamic scales of the flow field, and the flame thickness. Given the disparity between flame and acoustic length scales, the flame front essentially appears as a discontinuity to the flow. As such, the fluid dynamics of the flows up and downstream of the flame can often be treated separately from that of the flame structure. However, it should be emphasized that there is not necessarily a *corresponding disparity in time scales*; e.g. forming a flame response time scale, τ_M, from the ratio of the laminar flame thickness and flame speed leads to values of τ_M~0.002 - .07 s for methane/air flames. These are of similar magnitude of perturbations with frequencies between 20-500 Hz. Thus, the interior flame structure and, consequently, quantities such as the flame speed, do not respond in a quasi-steady manner to flow perturbations.

Because of the mutual interaction between the flame position and the flow field, free boundary problems such as this are extremely difficult to handle analytically. Initial studies used an integral technique [31,12,33] to make it analytically tractable. More recently, researchers have skirted these analytical difficulties encountered in the fully coupled flame-flow problem by neglecting the coupling of flow perturbations across the flame. For example, recent work in Ref [34,23,35,28] complements the studies of Baillot and co-workers discussed previously, by quantifying the *global* heat release response, Q', of the flame. These workers obtained high speed images and transfer functions, $(Q'/Q_o)/(u'/u_o)$, of acoustically forced Bunsen and inverted wedge flames. Significantly, all these studies showed that most of the key flame response characteristics could be

quantitatively predicted by assuming that the flame's heat release was directly proportional to its instantaneous area. The flame area was calculated using the *G*-equation, where measured velocity fields were used as inputs. As such, they calculated the response of the flame from an imposed velocity disturbance of given amplitude and phase upstream of the flame. Nonetheless, the substantially reduced complexity of the approach facilitates a much more transparent analysis; moreover, their results give excellent agreement with experiments in many instances.

Lieuwen [21] analyzed the exact, implicit solutions to the *G*-equation for understanding the nonlinear flame response to uniform velocity disturbances. It was shown that due to nonlinearities, the amplitude of the heat release transfer function relative to its linear (i.e., when $u'/u_o \ll 1$) value decreased with increasing amplitude of velocity oscillation, u'/u_o. Specifically, the velocity amplitude where nonlinearity in the transfer function became significant was shown to be strongly dependent on the Strouhal number, $St = \omega L_f/u_o$ (where L_f is the flame length), the ratio of the flame length to width, $\beta = L_f/R$, and the flame shape in the absence of perturbations (i.e., conical, inverted wedge, etc.). Also, it was demonstrated that the response of conical flames remained much more linear at comparable disturbance amplitudes than for "V" or wedge shaped flames.

1.3 Overview of Present Work

There are three key areas wherein our understanding of laminar flame dynamics is limited. The first is the role of the disturbance field characteristics in determining the *nonlinear* flame response. Most of the analytical models to date have assumed a uniform disturbance velocity field while studying non-linear effects (in contrast to experimental evidence) and as such are missing a key component of the physics. Secondly, there is no

theoretical framework to characterize the effect of variable flame propagation speed (due to *unsteady stretch* effects) on the flame dynamics. This is critical to understanding the "filtering" phenomenon observed by Bourehla & Baillot [24]. Most of the theoretical studies on flame stretch effects are currently limited to planar flames and are inadequate to understand the dynamics of anchored flames. Finally, there have been limited studies to explicitly understand as to how the *temperature jump across the flame* (resulting in a coupling between the flame and the unsteady flow field) alters the approach flow disturbance characteristics, as well as those of the flame dynamics itself. In all, this thesis will address these three outstanding issues in the course of providing a systematic treatment of linear and nonlinear dynamics of laminar premixed flames.

The remainder of this thesis is divided as follows: Chapter 2 describes the key processes impacting the flame dynamics and the disturbance field. In particular, the principal assumptions of the analysis are identified and the phenomena which can and cannot be captured by the analysis are discussed. In Chapter 3, the mathematical formulation and details about the flame geometry is presented. An analytical model is developed in Chapter 4 which captures the effects of flame geometry, disturbance field characteristics and perturbation frequency on the linear and nonlinear heat release response of premixed flames. The response of the flame at the perturbation frequency and its harmonics are analyzed as well as changes in the mean flame length. Next, a theoretical investigation of the impact of variable flame propagation speed (due to unsteady strain and curvature effects) on the linearized flame response is presented in Chapter 5. An explicit analytical criterion is deduced to determine the frequencies at which flame stretch effects become important and the key non-dimensional parameters

which characterize its impact on the flame dynamics. Details of the numerical approach wherein an unsteady compressible Euler flow solver is developed and coupled to a *G*-equation module are given in Chapter 6. The effect of coupling between the unsteady disturbance velocity field and the flame on the heat release response is discussed in Chapter 7. The effect of flame feedback on the upstream flow field and its impact on the flame dynamics is analyzed. Finally, Chapter 8 presents the conclusions of this research and recommendations for future work.

CHAPTER 2

FLAME RESPONSE: THEORETICAL CONSIDERATIONS

In this chapter, the key processes impacting the heat release dynamics and the disturbance velocity field are discussed. In particular, the origins of the wrinkles propagating along the flame, which play a key role in controlling the flame response, are discussed in detail. The characteristics of the disturbance velocity field and its impact on the linear/nonlinear response is analyzed. Experimental evidence of the importance of flame stretch on the flame dynamics is presented, which forms the foundation for the analysis in Chapter 5. Finally, the chapter ends with a discussion on the effect of gas expansion effects on the flame response and key aspects which need to be considered when comparing the heat release response for different T_b/T_u across the flame.

2.1 Flame Dynamics

The fundamental problem of interest is this: Given a disturbance velocity field, $u'(\vec{x},t)$, determine the response of the flame position, $\zeta(\vec{x},t)$, and in particular, the total heat release rate of the flame. The global heat release rate of the flame is given by:

$$Q(t) = \int_S \rho_1 S_L \Delta h_R dA_{FL} \quad (2)$$

where the integral is performed over the flame surface, A_{FL}, and Δh_R is the heat release per unit mass of reactant. Equation (2) shows the three fundamentally different ways of generating heat release disturbances in a premixed flame: fluctuations in mass burning rate ($\rho_1 S_L$), heat of reaction, or flame area. As noted by Clanet [36], they can be classified

based upon either their modification of the local internal structure of the flame (such as the local burning rate) or its global geometry (such as its area).

In order to focus upon the flame response to flow perturbations, Δh_R and mixture density, ρ_1; are assumed to be constant in the ensuing discussion. Analysis of the effects of these perturbations are given in Cho & Lieuwen [37] and McIntosh [14]. Of course, if the flow perturbation is acoustic in origin, a density disturbance will accompany the velocity fluctuation. However, their relative impacts differ greatly, on the order of the flame speed Mach number [37,38]. As such, attention is focused upon the quantity:

$$\frac{Q'}{\bar{Q}} = \frac{\int S_L' d\bar{A}_{FL}}{\int \bar{S}_L d\bar{A}_{FL}} + \frac{A_{FL}'}{\bar{A}_{FL}} \quad (3)$$

Flame speed perturbations are generated by the oscillating stretch rate, proportional to $\nabla^2 G$, and are discussed in Chapter 5. Flame area fluctuations are directly related to perturbations in the flame position through the relation:

$$A_{FL}(t) = \int 2\pi f(r)\,\delta\left(G - G_o\right)\left|\nabla G\right| d\Omega \quad (4)$$

where G_o denotes the flame surface and $f(r)$ is determined by the flame configuration (i.e. conical/wedge). This equation shows that the quantity of interest is not G itself, but its gradient ∇G - a very important observation. Another key observation is that only the velocity component normal to the flame, $\vec{u}\cdot\vec{n} = u_n$, a scalar quantity, impacts the flame dynamics. This can be seen by rewriting Eq. (1) as:

$$\frac{\partial G}{\partial t} + \left(u_n - S_L\right)\left|\nabla G\right| = 0 \quad (5)$$

This necessarily implies that the full three dimensional details of the velocity field are not significant; it is only the component that is normal to the flame. As such a detailed

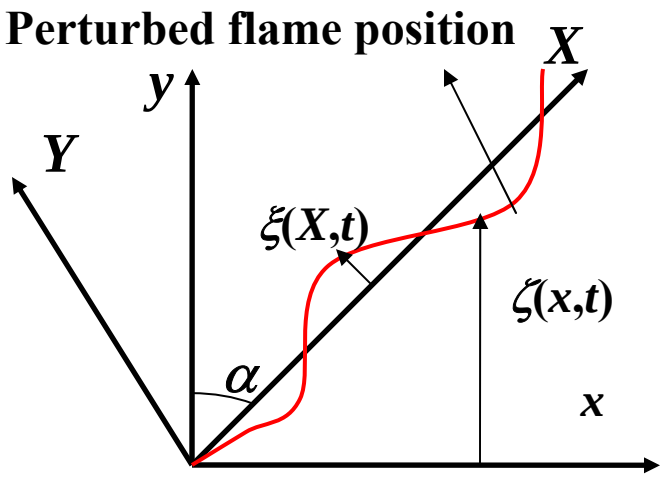

Figure 6 Coordinate system illustrating the perturbed flame shape

specification of the velocity field is not necessary for an understanding of the flame dynamics and, furthermore, a variety of different velocity fields can give an essentially identical flame response. This is the reason a relatively simple form of the disturbance velocity field is assumed for the theoretical analysis, as will be detailed in Chapter 3. However, for large amplitude oscillations, this point must be conditioned with the fact that the flame normal exhibits large fluctuations, so the relative contribution of each vector component of the velocity field varies throughout the cycle.

Several general comments can be made regarding the dynamics of the flame position gradient, which is directly related to its surface area through Eq (4); these will provide a great deal of insight into the flame dynamics. From a mathematical point of view, the linear solution to the equation for flame surface area can be decomposed into two canonical components: the homogeneous solution and the particular solution. The linearized version Eq. (1) can be written in a coordinate system aligned normal to the mean flame position as (see Figure 6)

$$\frac{\partial \xi}{\partial t} + U_o \frac{\partial \xi}{\partial X} = U'(X,t) \quad (6)$$

where X denotes the coordinate along the mean flame position, U_o is the mean velocity component along the X axis (i.e. the tangential velocity at the mean flame front) and $\xi(X,t)$ is the perturbed flame position normal to this coordinate, and the flame is flat. The dynamics of $\partial\xi / \partial X$, which is directly related to that of the flame area itself, is described by the following solution (see Appendix A for the derivation)[†]:

$$\frac{\partial \xi(X,t)}{\partial X} = \underbrace{\frac{1}{U_o}\int_0^X \left(\frac{\partial U'(X,t)}{\partial X}\right)_{X\to x', t\to\left(t-\frac{X-x'}{U_o}\right)} dx'}_{Flow\ non-uniformity\ (particular\ solution)} + \underbrace{\frac{1}{U_o}\left(U'\left(X=0, t-\frac{X}{U_o}\right) - U'_{base}\left(t-\frac{X}{U_o}\right)\right)}_{Boundary\ condition\ (homogeneous\ solution)} \quad (7)$$

The homogeneous and particular solutions have a clear physical significance which can be understood as follows. A spatially uniform velocity disturbance only excites the homogeneous solution (second term in Eq (7)). This can be understood by first assuming that the flame edge moves exactly in step with the particle velocity, i.e., $U'_{base} = U'(X=0, t-\frac{X}{U_o})$. In this case, the entire flame simply moves up and down in a bulk motion without a change in shape or area [39]. However, if a flame anchoring boundary condition is imposed ($U'_{base} = 0$), such that the flame remains fixed, the flow disturbance excites a flame front disturbance that originates at the boundary (X=0) and propagates along the mean flame front (i.e. along X axis) at a speed that is proportional to the mean flow velocity (U_o). These "homogeneous solution" flame dynamics were

[†] In Eq (7), after evaluating the velocity gradient $\partial U'/\partial X$, the integration has to be performed with respect to dx' after replacing the variable X by x' and t by t-(X-x')/U_o

extensively analyzed by Fleifel *et al.* [40]. If the disturbance flow field is spatially non-uniform, i.e., $\partial U'/\partial X \neq 0$, the particular solution is excited (first term in Eq (7)). This results in waves originating at the spatial location(s) of flow non-uniformity that also propagate along the flame at roughly the mean flow velocity.

Because the *G*-equation is first order in time, the flame acts as a low pass filter to flow disturbances, so that the amplitude of the two canonical solutions individually decay with increases in frequency as *1/f*. As such, the transfer function relating the response of the flame area to a spatially uniform velocity disturbance (where only the homogeneous solution is excited), $(A'/A_o)/(u'/u_o)$ has a value of unity at zero frequency, decays monotonically with frequency, but generally is not identically zero[‡]. In contrast, when the flame is perturbed by a spatially non-uniform disturbance (so that both the homogeneous and particular solution are excited), the flame area consists of a superposition of the two solutions. As such, though each solution decreases with frequency, their sum has oscillatory behavior and, in cases where they constructively interfere can even cause the transfer function, $(A'/A_o)/(u'/u_o)$ to exceed unity. This result was first predicted by Schuller *et al*. [35] and experimentally observed by Durox *et al*. [23]. In addition, the two solutions can destructively interfere, and in certain cases, exactly cancel each other so that the resulting transfer function $(A'/A_o)/(u'/u_o)$ identically equals zero.

Consider next several basic features of the nonlinear flame dynamics. The key mechanism of nonlinearity is illustrated in Figure 7. In this illustration, a flame is perturbed by a transient disturbance so that it has a corrugated shape, but then allowed to

[‡]An exception occurs in two-dimensional flames at frequencies where the flame tip motion is zero. In this case, the flame's linear area response is also zero.

relax back to its steady state, planar position. Flame propagation normal to itself smoothens out the wrinkle, so that its area eventually returns to being constant in time. As such, kinematic processes work to destroy flame area, as shown by the dashed lines in the bottom sketch. The rate of these area destruction processes depends nonlinearly upon the amplitude and length scale of the flame front disturbance. Large amplitude corrugations are smoothed out at a relatively faster rate than small amplitude perturbations. In the same way, short length scale corrugations are smoothed out faster than long length scales of the same disturbance magnitude. As discussed further below, this is the reason that nonlinearity is enhanced at higher disturbance frequencies, which generate shorter length scale flame corrugations.

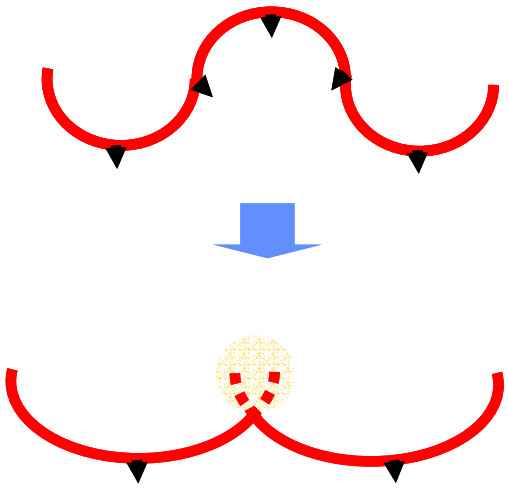

Figure 7. Sketch of a flame that is initially wrinkled (top), showing the destruction of flame area by kinematic restoration processes (bottom)

If the disturbance velocity field is spatially uniform (so that only the homogeneous solution is excited), nonlinear effects cause the nonlinear transfer function relating flame area and velocity perturbations, $(A'/A_o)/(u'/u_o)$, to monotonically decrease with disturbance amplitude [21]. In other words, the linear transfer function is larger than the

nonlinear transfer function. Since the scale of flame wrinkling is inversely proportional to frequency (scaling roughly as u_o/f), this reduction in finite amplitude transfer function relative to its linear value grows with frequency. As such, the flame area response to a velocity disturbance exhibits saturation characteristics, quite similar to the $H(\varepsilon)$ curve plotted in Figure 3.

In the general nonlinear case, as in the linear case, the effect of the superposition of the homogeneous and particular solutions upon the overall flame response depends upon whether the two solutions lie in a region of constructive or destructive interference. In particular, it can be anticipated that if the two solutions lie in a region of destructive interference and are affected unequally by nonlinearity, their superposition may cause the nonlinear transfer function to actually exceed its linear value. In Chapter 4, it will be shown that this occurs in some cases and, furthermore, has been experimentally observed.

2.2 Disturbance Field

The prior section touched upon the influence of the velocity field upon the flame dynamics. It showed that it is the normal component of the velocity, and not the velocity itself, that is significant in determining the flame response. Also implicit in Eq. (7) is that the detailed structure of these flow non-uniformities at each axial location is less significant than their integrated effect from the flame attachment point to that axial location. This section considers in more detail the character of the velocity field.

The velocity field can be decomposed into an irrotational, compressible component (the acoustic field) and a solenoidal, rotational component (vorticity field). Acoustic disturbances propagate with a characteristic velocity equal to the speed of sound. In a uniform flow, vorticity disturbances are convected at the bulk flow velocity, u_o. Acoustic

properties vary over an acoustic length scale, given by $\lambda_a=c/f$, while vortical disturbances vary over a convective length scale, given by $\lambda_c=u_o/f$. Consequently, in low Mach number flows, these disturbances have substantially different length scales. The vortical mode "wavelength" is shorter than the acoustic wavelength by a factor equal to the mean flow Mach number, $\lambda_c/\lambda_a=u_o/c=M$.

Vorticity disturbances propagate with the mean flow and diffuse from regions of high to low concentration. In contrast, acoustic disturbances, being true waves, reflect off boundaries, are refracted at property changes, and diffract around obstacles. The reflection of acoustic waves from multi-dimensional flame fronts generally results in a complex, multi-dimensional acoustic field in the vicinity of the flame [41].

Experiments have highlighted the significance of both acoustic and vorticity wave interactions with the flame front. These vorticity oscillations are generally manifested as large scale, coherent structures that arise from the growth of intrinsic flow instabilities. The phase velocity and growth rate of the flow instabilities is strongly affected by the amplitude of forcing and the relationship between the acoustic forcing frequency and the intrinsic flow instability. Acoustic excitation often causes their shedding rate to "lock-in" to the forcing frequency or one of its harmonics. For example, visualizations from the study of Durox *et al*. [23], clearly indicate that these convected vortical disturbance are excited at the shear layer of the burner exit by the imposed acoustic oscillations. Figure 4 obtained from this study superposes an image of the instantaneous wrinkled flame front and the convected vorticity field. By incorporating the convective phase variation into the disturbance velocity field, they show that the modeled flame area response agrees quite well with their data.

The characteristics of the instability waves that grow and merge to form these large scale structures are a function of the specific characteristics of the burner exit shear layer, such as co-flow velocity, and specifically upon the receptivity of this shear layer to external disturbances. In addition, the phase speed of the convected vortical instability waves are not equal to the flow velocity, but vary with frequency and shear layer characteristics. The shear layer instability wave growth rate similarly varies with frequency and the shear layer characteristics. To illustrate, Figure 8 plots Michalke's [42] theoretical curves of the dependence of the phase speed, u_c, of shear layer instability waves in a jet flow upon Strouhal number, $S_\theta = f\theta/u_o$, for several values of the momentum thickness, θ, to jet radius, R, ratio, R/θ. The figure shows that, for all R/θ values, the ratio of u_c/u_o equals unity and 0.5 for low and high Strouhal numbers. For thin boundary layers, e.g., R/θ =100, the phase velocity actually exceeds the maximum axial flow velocity in a certain S_θ range. This ultra-fast phase velocity prediction has been experimentally verified by Bechert & Pfizenmaier [43] and may explain a similar measurement in a Bunsen flame by Ferguson *et al*. [44]. The dispersive character of the instability wave convection velocity has been confirmed by a variety of measurements in acoustically forced flames. For example, Baillot *et al*. [19] measured u_c/u_o values of 1.13 and 1.02 at 35 and 70 Hz, respectively, on a conical Bunsen flame. Durox *et al*. [23] measured u_c/u_o =0.5 values at 150 Hz in an axisymmetric wedge flame.

In general, the disturbance field may have both acoustic and vortical components, whose relative magnitude depends strongly upon the vortex shedding dynamics at the burner shear layer. For example, Ferguson *et al*. [44] found that the disturbance field transitioned from a convected character to one with an acoustic character at "low" and

"high" frequencies, respectively. Similar results were obtained by Birbaud *et al.* [28], who characterized the upstream flowfield of a conical flame using PIV measurements. By considering a velocity potential associated with the flame motion, this transition in the flow field characteristics was attributed to the upstream influence of the flame wrinkling. These points show that the character of the disturbance field can vary significantly between its relative acoustic and vortical components, as well as their spatial structure (such as phase speed) – these characteristics will change with experimental configuration, frequency, and amplitude of perturbation. This point is a key motivator for the development of a general theory for arbitrary phase speed velocity disturbances in Chapter 4.

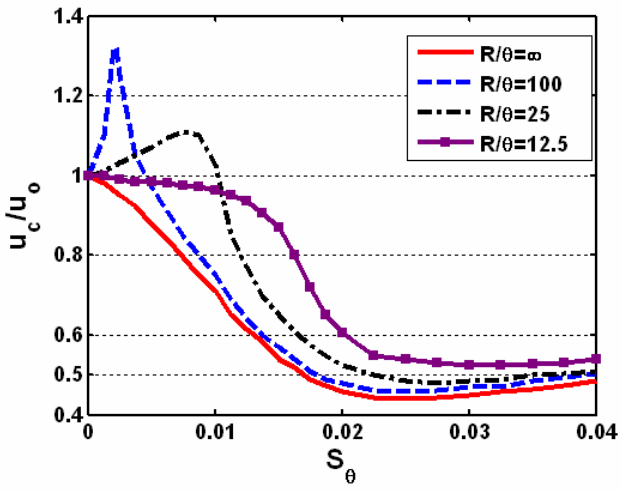

Figure 8 Dependence of shear wave convection velocity and growth rate in a jet flow upon Strouhal number and ratio of jet radius to momentum thickness. Figure reproduced from Michalke [42]

The amplitude dependence of the disturbance field characteristics should be noted. Even in the absence of convected vorticity waves, the impact of the fluctuating flame position upon the acoustic field should cause the acoustic disturbance field to have a

"convected" character. This is due to the fact that the flame response to the acoustic field and the acoustic field disturbing the flame are coupled. For large amplitude disturbances, the flame develops large corrugations, such as can be seen in Figure 4, that convect with a phase speed proportional to the axial flow velocity. These convecting flame wrinkles impact the character of the interior acoustic field. It can be anticipated that this mechanism causes the acoustic field structure to revert from being nearly uniform (assuming a compact flame) to having some convected characteristics at low and high amplitude disturbances, respectively. This issue requires further clarification, as the effects of amplitude and frequency on the acoustic field structure have not been measured or calculated in the large amplitude case.

2.3 Flame Stretch Effects

Prior studies related to flame dynamics have assumed that the burning velocity was constant, so that the flame speed is independent of the flow field (several analyses [45,37] have included mixture ratio perturbation effects on the flame speed, however). In reality, hydrodynamic strain and flame curvature introduced by the flow oscillations leads to perturbations in flame speed. In flames that are thermo-diffusively stable, these unsteady stretch effects act to smooth out the flame front corrugation. This causes the amplitude of the flame wrinkle to diminish as it propagates along the flame. As the radius of flame wrinkling is approximately proportional to the inverse of the squared frequency, it can be anticipated that this effect grows in significance with frequency.

Some experimental results that demonstrate and extend the "filtering" phenomenon mentioned in Bourehla & Baillot [24] are discussed next, which show that these observations are consistent with the concept of stretch. The theoretical analysis that

yields the appropriate nondimensional parameters and assessments of the flame response are presented in Chapter 5.

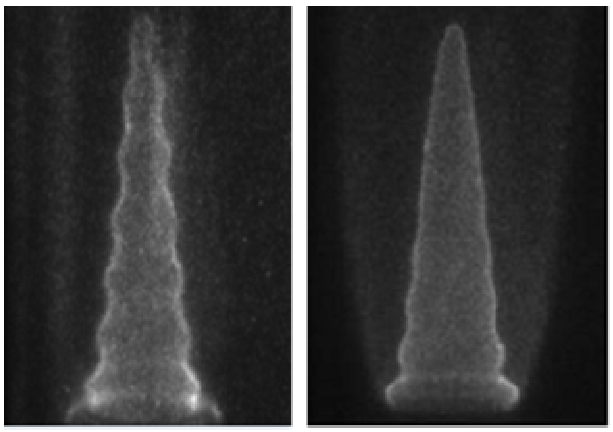

Figure 9 Visualization of (a) a 130 Hz acoustically excited lean methane flame (Equivalence ratio = 0.8, u_o= 0.65 m/s) and (b). a 140 Hz acoustically excited rich methane flame (Equivalence ratio = 1.4, u_o= 0.7 m/s) Images show flame wrinkles that propagate the entire length of the flame and that are quickly damped, respectively.

Flame images of the "filtering" phenomenon were obtained with a 2.54 cm diameter Bunsen burner, previously described in Rajaram and Lieuwen [46, 47]. Acoustic oscillations were excited with a loudspeaker placed at the bottom of the burner tube. The flame was stabilized with a methane-fueled (ϕ=1.15) annular pilot. Experiments were performed with two fuels, methane and propane, which are respectively thermal-diffusively stable under rich and lean conditions, and unstable otherwise, when subjected to spatial perturbations through the action of stretch. The controlling Lewis numbers (*Le*) for the stable and unstable cases are respectively greater and smaller than unity, with methane being only weakly nonequidiffusive because its *Le* deviates just slightly from unity.

Figure 9 shows images of the lean and rich methane flames under disturbances of similar frequencies. It is seen that while the wrinkling decays in the downstream direction

for the rich flame, it persists for the lean flame. Figure 10 shows images of two lean propane flames, with the frequency of the right image being twice that of the left, resulting in wrinkles with smaller and larger wavelengths, respectively. It is seen that while the wrinkles persist along the flame front for the smaller frequency, similar to previous observations (Bourehla & Baillot [24]), they decay rather rapidly for the larger frequencies. The latter situation, apparently, is the "filtering" phenomenon reported by Bourehla & Baillot [24].

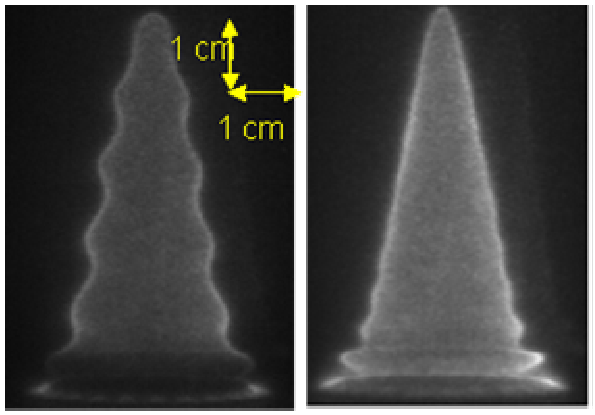

Figure 10 Visualization of a 100 Hz (left) and 190 Hz (right) acoustically excited propane flame. Images show flame wrinkles that propagate the entire length of the flame and that are quickly damped, respectively. Equivalence ratio = 0.7, u_o= 0.8 m/s

The above observations demonstrate the two crucial parameters governing the evolution of the imposed wrinkles on the flame surface, namely *curvature-induced stretch* coupled through the action of mixture nonequidiffusion, and the *frequency* of the disturbance. In particular, Figure 9 shows that, when the mixture is thermal-diffusively more stable as characterized by a larger Lewis number for the rich methane flame, the wrinkles are smoothed more rapidly as they propagate downstream along the flame surface. In addition, Figure 10 shows that, for the thermal-diffusively stable lean propane flames, the efficiency of stabilization is also promoted with decreasing wavelength and

thereby increasing curvature of the wrinkles. These arguments suggest that the fundamental mechanism governing the persistence or decay of the imposed wrinkles is that of stretch in the presence of mixture nonequidiffusion. The analysis which quantitatively describes this phenomenon is presented in Chapter 5.

2.4 Effect of Gas Expansion

In most theoretical studies, the velocity field is prescribed, rather than solved for. In general, it should be emphasized that the thermal expansion of gases at the flame front causes the flame to influence the velocity field upstream of it; this coupling is responsible for the Darrius-Landau flame instability. In this section, attention is focused on the very important issue of the manner in which these mutual interactions impact the results, the conditions under which the constant density analysis is appropriate, and the conditions where additional physics qualitatively influences the flame dynamics.

First it should be noted that imposing the velocity field is a rigorously valid approximation in the limit of low dilatation flames; i.e., in the limit where $T_b/T_u \rightarrow 1$. This is also the limit considered by other authors for studies of the thermal-diffusive instability and is the basis of the Sivashinsky-Kuramoto equation [48, 49]. Besides being of academic interest in allowing one to analytically handle the problem, this is actually a useful limit for many practical devices. It is often pointed out in the combustion literature that practical flames have temperature ratios on the order of 6-10. This is true for flame's consuming reactants at *room temperature* but not, however, for the conditions encountered in most practical devices. Due to the need for high efficiencies (e.g., devices utilizing regenerative heating or high compression ratios such as industrial boilers or gas turbines) or because the devices are using vitiated air (duct burners or jet engine

augmentors), unburned gas temperatures are substantially higher. Correspondingly, the requirement for low NOx emissions implies lower burned gas temperatures. As such, typical temperature ratios for practical premixed combustion devices are in the range of 2-3, and even as low as 1.5 in certain industrial applications with large amounts of regenerative pre-heating.

Clearly, however, as T_b/T_u deviates from unity, there will be an impact upon the approach flow characteristics. It can readily be shown that the impact of the flame on the acoustic field scales as $(T_b/T_u)^{1/2}$, which is the ratio of the gas impedances across the flame. Based upon the discussion in the prior section it can be anticipated that, at least for low amplitude perturbations, the alteration of the local acoustic field by the flame does not introduce qualitative changes into the flame dynamics, although it may certainly exert quantitative impacts that increase as $(T_b/T_u)^{1/2}$. This assertion has been previously confirmed by Lee & Lieuwen [39], who computationally determined the flame's acoustic nearfield for various T_b/T_u values, determined the flame area response, and compared the results to the constant density analyses [40,34].

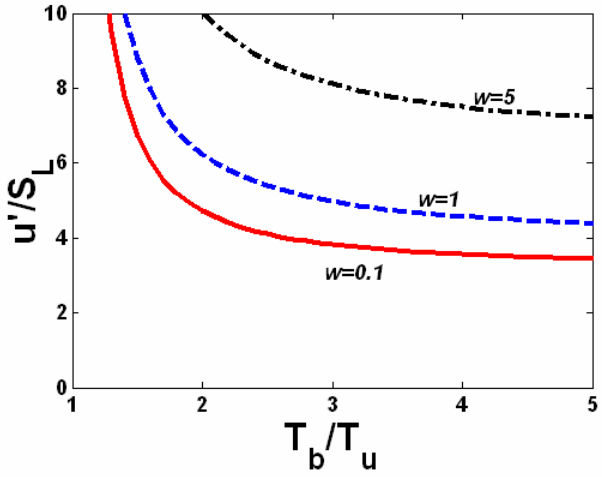

Figure 11 Parametric stability limits of flat flame (unity Lewis and Prandtl number, no gravity).

Similarly, it is known (see Searby & Clavin [50]) that the effect of a stable flame on the vortical approach flow velocity scales approximately as T_b/T_u. As in the acoustic case, there is clearly also a frequency-wavenumber dependence, as well as an inverse dependency upon proximity to flame stability boundaries.

The qualitative similarities between fully coupled flame dynamics and that determined using an imposed velocity field break down when both T_b/T_u and perturbation velocity amplitudes are large; i.e., new dynamics appear that cannot be captured with the constant density analysis. This is due to the appearance of a parametric flame instability [51,52,53], manifested by cellular structures that oscillate at half the period of the disturbance. This parametric acoustic instability is due to the periodic acceleration of the flame front by the unsteady velocity field, which separates two regions of differing densities. With increased amplitudes, these organized cellular structures break down into a highly disordered, turbulent front. The regimes in T_b/T_u vs u'/S_L space where this instability occurs can be determined from Eq. (1) in [53], for a given dimensionless frequency, defined as $w = \dfrac{\omega \delta_f}{S_L}$ where ω is the forcing frequency and δ_f is the flame thickness. The results are plotted in Figure 11. This graph illustrates the regions (above the curve) where application of a prescribed velocity theory is inappropriate. As could be anticipated, it shows that the range of disturbance amplitudes diminishes with increasing temperature ratio across the flame. As such, it is concluded that the qualitative linear dynamics of the flame are captured by this analysis for all T_b/T_u values, although the quantitative accuracy of the results deteriorates as T_b/T_u increases. These issues will be

considered in Chapter 7 wherein the flame dynamics is numerically simulated by coupling the G-equation to an Euler solver in order to capture the effect of T_b/T_u.

Finally, comparing transfer functions across different T_b/T_u cases requires some care as the mean and perturbation velocity magnitude varies along the flame. To demonstrate this point, consider the flame coordinate system in Figure 12. In the context of Eqs (6) and (7), the discussion was specific to flame dynamics in a uniform mean flow with a non-uniform disturbance field. For a general non-uniform mean velocity field denoted by $\bar{u},\bar{v}$, the governing equations for the mean (denoted by bar quantities) and perturbed flame position (prime) can be expressed as (see Appendix B for derivation):

$$\bar{u} - \beta\bar{v}\bar{\zeta}_r - S_L(r)\sqrt{1+\beta^2\bar{\zeta}_r^2} = 0 \qquad (8)$$

$$\zeta_t' = u' - \beta\bar{v}\zeta_r' - \beta v'\bar{\zeta}_r - \frac{\beta^2 S_L(r)\bar{\zeta}_r\zeta_r'}{\sqrt{1+\beta^2\bar{\zeta}_r^2}} \qquad (9)$$

In Eqs (8) and (9), (u,v) has been non-dimensionalized using the *inlet* mean flow velocity (u_o) , ζ by mean flame length L_f and r by the burner radius R. The flame aspect ratio, L_f/R, is denoted as β. Equation (9) can be rewritten in terms of the fluctuating normal velocity and mean tangential velocity (at the flame) as:

$$\zeta_t' = u_n'\sqrt{1+\beta^2\bar{\zeta}_r^2} + \frac{\beta\bar{u}_t}{\sqrt{1+\beta^2\bar{\zeta}_r^2}}\zeta_r' \qquad (10)$$

where the subscripts n,t denote normal and tangential respectively. Note the fact that the *flame position is controlled exclusively by the normal perturbation velocity and the mean tangential velocity along the flame front.*

The general solution for the *fluctuating flame area* (two-dimensional case) in a non uniform mean velocity field ($\bar{u},\bar{v}$), can be expressed as (see Appendix B for derivation and Figure 12 for the schematic):

$$\frac{\hat{A}}{A_o}=\frac{\beta^2}{\sqrt{1+\beta^2}}e^{-iStH(0)}\frac{\bar{\zeta}_r(0)}{P(0)}\chi(0)+\frac{\beta}{\sqrt{1+\beta^2}}\int_0^1\left(e^{-iStH(r)}\kappa(r)\chi(r)\right)dr \qquad (11)$$

where

$$\begin{aligned}
\chi(r)&=\int_1^r\left(e^{iStH(\theta)}\frac{P(\theta)\hat{u}_n(\theta)}{F(\theta)}\right)d\theta\\
F(r)&=\frac{\beta\bar{u}_t}{\sqrt{1+\beta^2\bar{\zeta}_r^2}}\\
P(r)&=\sqrt{1+\beta^2\bar{\zeta}_r^2}\\
\kappa(r)&=\beta\left(\frac{\bar{\zeta}_r}{P(r)}\right)_r=\frac{\beta\bar{\zeta}_{rr}}{\left(1+\beta^2\bar{\zeta}_r^2\right)^{3/2}}\\
H(r)&=\int_1^r\frac{1}{F(r)}dr
\end{aligned} \qquad (12)$$

Equation (12) *explicitly* brings out the characteristic frequency controlling the flame response as:

$$-StH(0)=St\int_0^1\frac{1}{F(r)}dr=St\int_0^1\frac{\sqrt{1+\beta^2\bar{\zeta}_r^2}}{\beta\bar{u}_t}dr=\frac{St}{\beta}\int_0^1\frac{dl_F}{\bar{u}_t} \qquad (13)$$

Note that in Eq (13), $dl_F/\bar{u}_t$ corresponds to the time it takes for the wrinkle to propagate a distance , dl_F , along the mean flame front with the flame tangential velocity $\bar{u}_t$. So the characteristic frequency is essentially an integrated measure of the time it takes for the wrinkle to propagate from the flame base to the tip. For a uniform axial mean flow, (i.e. $v=0,\bar{\zeta}_r=-1$), the characteristic frequency given by Eq. (13) reduces to:

$$St\int_0^1\frac{\sqrt{1+\beta^2}}{\beta}\frac{\sqrt{1+\beta^2}}{\beta}dr=St\frac{1+\beta^2}{\beta^2}=St_2 \qquad (14)$$

For the special case of uniform axial mean flow, Eq (11) reduces to:

$$\frac{\hat{A}}{A_o} = \int_0^1 \sqrt{1+\beta^2}\, e^{irSt_2}\ \hat{u}_n(r)dr \qquad (15)$$

In this simplified situation, the flame response is driven by the correlation between the perturbation velocity normal to the flame ($\hat{u}_n$) and the harmonic term, e^{irSt_2}. Note that in the limit of *low Strouhal numbers, the flame response is driven by the integral of the normal perturbation velocity over the flame front,* i.e.,

$$\frac{\hat{A}}{A_o} \approx \int_0^1 \sqrt{1+\beta^2}\ \hat{u}_n(r)dr$$

Next, for the general case of a non-uniform mean velocity field, consider the individual terms which contribute to the total flame response (see Eq (11)). The first term is composed of quantities which have been integrated over the entire flame while the second term is strongly dependent on the spatial variation of the mean flame/flow parameters. Essentially, the first term is controlled by the quantity, $\chi(0)$:

$$\chi(0) = -\int_0^1 \left(e^{iStH(r)} \frac{P(r)\hat{u}_n(r)}{F(r)} \right) dr$$

which is the integral (over the entire flame) of the normal perturbation velocity weighted by the harmonically oscillating term $e^{iStH(r)}$ and the mean flow/flame parameters. Significantly, the second term in Eq (11) is directly proportional to the *local curvature of the mean flame*, $\kappa(r)$. For the case of a uniform axial mean flow (see Eq (15)), the contribution from this term is identically zero due to the absence of curvature in the mean flame. The contribution from this term will become significant when the velocity field due to the combined effect of gas expansion and confinement causes the mean flame front to have curvature. Note that the mean flame front will have curvature if ($\overline{u}, \overline{v}$) have

radial non-uniformity.

From Eq (11), it can be clearly inferred that the flame response is driven by the *normal component of the velocity fluctuation* (as was pointed out earlier in the context of Eq (5)). Even if the velocity excitation amplitude at the flame base is the same, the spatial variation of u_n' along the flame will vary with T_b/T_u. Then, defining the transfer function based upon the perturbation velocity at the flame base will lead to physically misleading results. So it is critical to define a physically useful reference velocity, u'_{ref}, for the transfer function in order to meaningfully compare flame transfer functions across cases where the spatial structure of the perturbation velocity is different; see also the discussion in Ref. [39]. For example, if the perturbation velocity magnitude is near zero at the base of the flame, but has much larger values everywhere else, then the transfer function based on the flame base velocity fluctuations will be unacceptable. Similarly, the appropriate definition of reference velocity is different for conical and wedge flames, because of the significantly different spatial distribution in flame area. Another key parameter is the *mean flow velocity component which is tangential to the mean flame front*. This is because the mean tangential velocity, $\overline{u}_t$, (see Eqs (11), (13) and (14)) controls the speed with which the wrinkles propagate from the flame base to the tip (see the flame images in Figure 9 and Figure 10). Since $\overline{u}_t$ strongly varies with T_b/T_u (see Chapter 7 for details), there is a considerable change in the wrinkle residence time. As shown in Eq (14) for a uniform mean axial flow field, the flame response is strongly controlled by the reduced Strouhal number, St_2, which is defined to be the time it takes for a wrinkle to propagate from the flame base to the tip normalized by the acoustic time period. So, although the flame might be excited at the same frequency and have the same mean flame length, the

effective Strouhal number (see Eq (13)) is different due to the mean tangential velocity having a strong spatial dependence for T_b/T_u.>1. This discussion highlights the need for careful consideration of reference velocity and the effective Strouhal number when comparing transfer functions for different T_b/T_u across the flame.

CHAPTER 3

THEORETICAL FORMULATION

In this chapter the general mathematical formulation and the subsequent non-dimensionalization is presented. The flame geometry under consideration is illustrated and the applicable boundary conditions are defined. Following the formulation presented here, the linear and non-linear flame dynamics of constant burning velocity flames is analyzed in Chapter 4. Subsequently, the linear response of premixed flames with variable flame speed due to stretch effects is studied in Chapter 5.

3.1 Mathematical Model

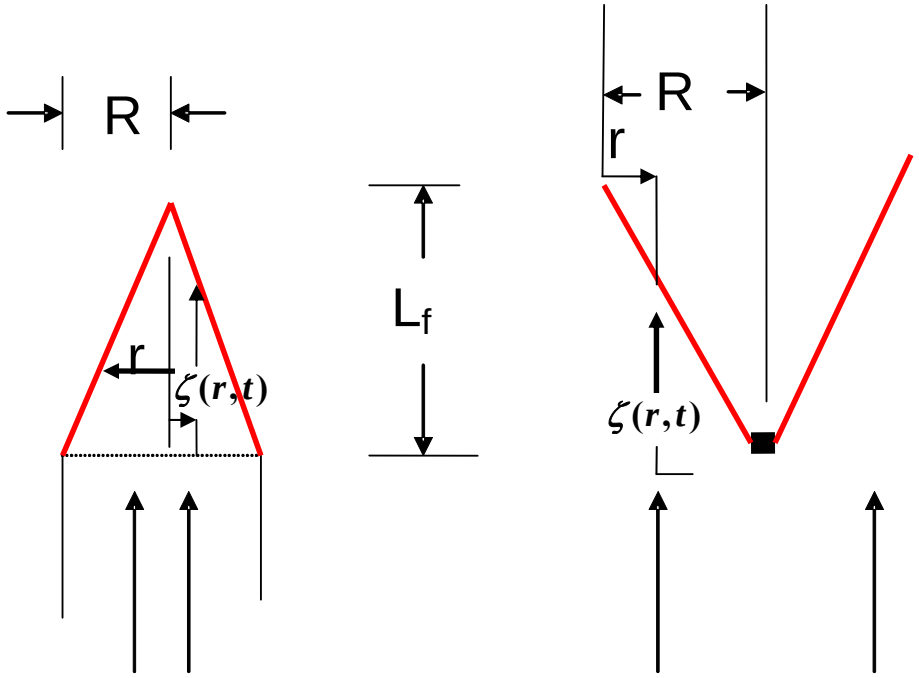

Figure 12. Illustration of conical (left) and wedge shaped (right) flame geometries

The analytical approach used here closely follows Baillot *et al*. [20], Ducruix *et al*. [34] and Fleifel *et al*.[40]. The flame's dynamics are modeled with the front tracking equation:

$$\frac{\partial \zeta}{\partial t} = u - v\frac{\partial \zeta}{\partial r} - S_L\sqrt{\left(\frac{\partial \zeta}{\partial r}\right)^2 + 1} \quad (16)$$

where u and v denote the axial and radial velocity components, and S_L is the local (stretch affected) flame speed.

The variables t, r, u and ζ are non-dimensionalized by u_o/L_f, R, u_o and L_f. (note that the value of L_f and R refer to their nominal values without imposed oscillations), where u_o is the mean axial velocity. They are related to the unstretched flame speed and average flow velocity by:

$$\frac{u_o}{S_{L,o}} = \sqrt{\left(\frac{L_f}{R}\right)^2 + 1} \quad (17)$$

The ratio of the flame length to radius plays an important role in the flame's dynamics and is denoted by β.

$$\beta = \frac{L_f}{R} \quad (18)$$

Given these assumptions, the flame dynamics are given by (from this point the same symbol will be used for the dimensionless variable):

$$\frac{\partial \zeta}{\partial t} + \frac{S_L}{S_{L,o}}\sqrt{\frac{1+\beta^2\zeta_r^2}{1+\beta^2}} = u(\zeta,t) - \beta\, v(\zeta,t)\zeta_r \quad (19)$$

The flame speed can be expressed as [54]

$$S_L / S_{L,o} = 1 - \delta \nabla \cdot n + \frac{Ze}{2}\left(\frac{1}{Le} - 1\right)\delta \frac{\kappa}{S_{L,o}} \quad (20)$$

where $S_{L,o}$ is the constant, laminar flame speed, $\boldsymbol{n}$ the local normal on the flame front pointing toward the unburned mixture, δ the flame thermal thickness, Ze the Zel'dovich number, and κ the flame stretch rate given by

$$\kappa = -n \cdot \nabla \times \left(v \times n\right) + (V \cdot n)(\nabla \cdot n) \quad (21)$$

where $\mathbf{v} = (u, v)$ is the flow velocity at the flame front on the unburned side and $V = dx/dt$ the local velocity of the flame front. Throughout this chapter, the study will be limited to the case of weak stretch, namely $\delta \to 0$, and assume $Ze\left(Le^{-1} - 1\right) \sim O(1)$. It is seen from the second and third terms of Eq. (20) that the modification of the flame speed by stretch is given by the sum of pure curvature effect and nonequidiffusion-related stretch effect.

Following prior studies [19,40], the flame is assumed to be anchored at the base; i.e.,

$$\zeta\left(r = 1, t\right) = 0 \quad (22)$$

In this analysis a two-dimensional wedge flame stabilized by a bluff body is considered (see Figure 12 for the schematic). The instantaneous flame-sheet location at the radial location, r, is given by $\zeta(r,t)$ and is assumed to be a single-valued function of r.

For wedge flames, apart from the flame anchoring condition (see Eq (22)), the second boundary condition (required only when the flame speed varies with stretch) comes from the requirement that all information should flow out of the flame – this implies a boundary condition with characteristics flowing out of, and not into, the

domain. An intuitive way of thinking of this boundary condition is that it requires that the flame tip is free to move around (see Figure 12), i.e.

$$\frac{\partial^2 \zeta(r=0,t)}{\partial r^2} = 0 \qquad (23)$$

3.2 Specification of Velocity Field

The axial velocity field is specified as:

$$u(\zeta,t) = u_o + u' \, Cos\left(k\zeta - \omega_o t\right) \quad (24)$$

Assuming an incompressible disturbance field, appropriate for a vortical or long wavelength (λ/L_f>>1) acoustic disturbance, the radial velocity is then:

$$v(\zeta,t) = \frac{u'k\,\tilde{r}}{2} \, Sin\left[k\zeta - \omega_o t\right] \qquad (25)$$

where $\tilde{r} = r$ for conical and $\tilde{r} = 1 - r$ for wedge flames.

Here the wave number k is defined as:

$$k = \frac{\omega_o}{u_c} = \left(\frac{\omega_o}{u_o}\right)\left(\frac{u_o}{u_c}\right) = K\left(\frac{\omega_o}{u_o}\right) \qquad (26)$$

where u_c is defined as the phase velocity of the disturbance and ω_o denotes the angular frequency of the velocity disturbance. K is a parameter which denotes the ratio of the mean flow velocity to the phase velocity of the disturbances. The two key impacts of the flow field on the flame front, given by the term $\partial u'/\partial X$ in Eq (7) are captured here by the perturbation amplitude, ε, and the velocity length scale, u_c/ω_o.

The non-dimensionalized velocity field is given by:

$$u(\zeta,t) = 1 + \varepsilon Cos\left[St\left(K\zeta - t\right)\right] \quad (27)$$

$$v(\zeta,t) = \frac{\varepsilon KSt\,\tilde{r}}{2} Sin\left[St\left(K\zeta - t\right)\right] \quad (28)$$

where

$$\text{Strouhal number, } St = \frac{\omega_o L_f}{u_o} \quad (29)$$

$$\text{Velocity perturbation: } \varepsilon = \frac{u'}{u_o} \quad (30)$$

Note that the boundary condition given by Eq (22) cannot be used for disturbance velocity magnitudes where the instantaneous flow velocity is lower than the flame speed. In this case, the flame will flash back and Eq. (22) must be replaced by a different condition; e.g., see Dowling [17]. In this study, calculations are performed for velocity magnitudes up to this critical value. We define the following parameter, ε_f, which is the velocity magnitude at flashback for an axial flow.

$$\varepsilon_f = 1 - \frac{1}{\sqrt{1+\beta^2}} \quad (31)$$

CHAPTER 4

FLAME RESPONSE: EFFECT OF DISTURBANCE FIELD CHARACTERISTICS

In this chapter, the dynamics of constant burning velocity premixed flames responding to harmonic velocity disturbances is investigated. Results are derived from analytical and computational solutions of the nonlinear *G*-equation and compared with available experimental data. It is shown that the linear and nonlinear characteristics of the flame dynamics are controlled by the superposition of two sources of flame disturbances: those originating at the flame anchoring point due to boundary conditions and from flow non-uniformities along the flame. These disturbances do not generally propagate along the flame at the same speed. Consequently, they may either constructively or destructively superpose, so that the overall linear flame response depends upon two Strouhal numbers, St_2 and St_c, related to the amount of time taken for a flow (St_c) and flame front (St_2) disturbance to propagate the flame length, normalized by the acoustic period. The nonlinear flame response is controlled by flame propagation normal to itself, which smoothens out the wrinkles induced by the forcing at an amplitude dependent rate. Because the overall flame response is a superposition of the two flame disturbance contributions, the flame's nonlinear response exhibits two qualitatively different behaviors. For parameter values where these disturbances constructively interfere, the nonlinear flame response saturates. When the flame disturbances destructively interfere, the nonlinear transfer function may actually exceed its linear value before saturating. This result explains Durox *et al's*.[23] experimentally observed variation of the nonlinear

flame response with frequency. The analysis also predicts the impact of flow forcing on the average flame length. It is shown that in most cases, the flame length decreases with increasing perturbation amplitude, as has been experimentally observed by Bourehla and Baillot [24] and Durox *et. al.* [25].

4.1 Analysis Procedure

Two approaches were used to analyze the properties of Eq (19) with the flame speed assumed to be a constant. Analytical expressions for the linear and nonlinear flame response were obtained from a perturbation analysis carried out to third order in ε. Terms of $O(\varepsilon^3)$ are required to determine the leading order nonlinear corrections to the flame transfer function at the forcing frequency, and the first order result for the flame response at the third harmonic, $3\omega_0$. Nonlinear corrections to the average flame length and the flame response at the first harmonic, $2\omega_0$, are obtained at $O(\varepsilon^2)$.

For the fully nonlinear case, Eq.(19) is solved numerically. A robust numerical scheme is necessary which can accurately capture the formation of sharp gradients and cusps in the distorted flame front. Spatial derivatives are discretized using a Weighted Essentially Non-Oscillatory (WENO) scheme designed specifically for Hamilton-Jacobi equations [55]. This scheme is uniformly fifth order accurate in regions wherein the spatial gradients are smooth and third order accurate in discontinuous regions. Derivatives at the boundary nodes are calculated using fifth order accurate upwind-differencing schemes so that only the nodes inside the computational domain are utilized. A Total Variation Diminishing (TVD) Runge-Kutta scheme [56], up to third order accurate, is used for time integration. The non-dimensionalized spatial and temporal resolution in all the simulations is 10^{-3} and 10^{-4} respectively. The flame front perturbation is tracked and the

corresponding change in the flame surface area is calculated as a function of time for a given upstream flow velocity perturbation. The transfer function relating the flame area at the forcing frequency to the convective velocity perturbation is then evaluated.

4.2 Results and Discussion

4.2.1 Linear Flame Dynamics

In this section, expressions for the flame area-velocity transfer function that generalize the result of Schuller *et al*. [35], by determining the response of a flame to a disturbance with an arbitrary phase velocity are derived. This transfer function is defined as :

$$G = \frac{A'/\bar{A}}{u'_{ref}/u_o} \quad (32)$$

where u'_{ref} is the reference perturbation velocity. The analytical expressions obtained using the velocity field in Model A and Model B are presented in Sections 4.2.1.1 and 4.2.1.2 respectively.

Two velocity models are considered for further analytical development. In Model A, the velocity is assumed to be purely axial and thus the radial velocity component (Eq. (28)) is neglected. In Model B, the two-dimensional velocity field (i.e. both Eqs (27) and (28)) is considered.

4.2.1.1 Velocity Model A

4.2.1.1.1 *Flame Shape*

The flame position is expanded as [19]:

$$\zeta(r,t) = \zeta_o(r) + \zeta_1(r,t)\ \varepsilon\ +\ \zeta_2(r,t)\ \varepsilon^2 + \zeta_3(r,t)\ \varepsilon^3 + O\left(\varepsilon^4\right) \quad (33)$$

The evolution equation for $\zeta_1(r,t)$ is computed here and the $\zeta_2(r,t)$, $\zeta_3(r,t)$ terms are computed in Section 4.2.2. The mean flame shape in the absence of perturbations is given by

$$\zeta_o(r) = 1 - r \quad (34)$$

Substituting Eqs (33) and (34) into Eq (19), the evolution equation for ζ_1 (using Model A for the velocity field) is:

$$\frac{\partial \zeta_1}{\partial t} - \frac{\beta^2}{1+\beta^2}\frac{\partial \zeta_1}{\partial r} - Cos\left[St\left\{K(1-r) - t\right\}\right] = 0 \quad (35)$$

The solution of Eq. (35), given the boundary condition in Eq. (22) is

$$\begin{aligned}\zeta_1 &= \zeta_{1,BC} + \zeta_{1,Flow} \\ &= \frac{Sin\left[\dfrac{St\ \left(r - 1 + \alpha t\right)}{\alpha}\right]}{(\eta - 1)\ St} - \frac{Sin\left[St\left(K(r-1) + t\right)\right]}{(\eta - 1)\ St}\end{aligned} \quad (36)$$

where

$$\alpha = \frac{\beta^2}{\beta^2 + 1} \quad (37)$$

$$\eta = K\alpha \quad (38)$$

This equation explicitly decomposes the solution into contributions from boundary conditions and flow forcing non-uniformities. Note that this expression is valid for both

conical and wedge flames. The limit where $\eta \to 1$ (corresponding to instances where the two disturbances propagate along the flame at the same speed), is given by:

$$\lim_{\eta \to 1} \zeta_1 = \frac{(r-1)}{\alpha} Cos\left(St\left\{ \frac{(r-1)}{\alpha} + t \right\} \right) \quad (39)$$

4.2.1.1.2 *Flame Area-Velocity Transfer Function: Relative Contribution of Different Sources*

The surface area for a conical flame is given by:

$$\frac{A_c(t)}{\bar{A}_c} = 2 \frac{\int_0^1 r \sqrt{1 + \beta^2 \left(\frac{\partial \zeta}{\partial r} \right)^2} \, dr}{\sqrt{1+\beta^2}} \quad (40)$$

Substituting Eqs. (33), (34) and (36) in Eq. (40) and defining $G_c = \frac{A_c' / \bar{A}_c}{u'(y=0)/u_o}$ (i.e., $u'_{ref} = u'(y=0)$) yields:

$$\begin{aligned} G_c(St_2, \eta) &= G_{c,BC} + G_{c,Flow} \\ &= 2\left(\frac{e^{iSt_2} - 1 - iSt_2}{(\eta - 1)\, St_2^2} \right) + 2\left(\frac{1 - e^{i\eta St_2} + i\eta St_2}{\eta(\eta-1) St_2^2} \right) \quad (41) \\ &= 2\left(\frac{\eta\left(1 - e^{iSt_2}\right) + e^{i\eta St_2} - 1}{\eta(1-\eta) St_2^2} \right) \end{aligned}$$

where

$$St_2 = \frac{St}{\alpha} = \frac{St\left(1+\beta^2\right)}{\beta^2} \quad (42)$$

Following a similar procedure, the following result can be obtained for wedge flames:

$$G_w(St_2,\eta) = G_{w,BC} + G_{w,Flow}$$
$$= 2\left(\frac{1+i(i+St_2)e^{iSt_2}}{(\eta-1)\ St_2^2}\right) + 2\left(\frac{(1-i\eta St_2)e^{i\eta St_2}-1}{\eta(\eta-1)St_2^2}\right) \quad (43)$$
$$= 2\left(\frac{\eta-1+i(i+St_2)\eta e^{iSt_2}+(1-i\eta St_2)e^{i\eta St_2}}{\eta(\eta-1)St_2^2}\right)$$

Eqs (41) and (43) reduce to the expressions previously developed by Schuller *et al*. [35] when the phase speed of the disturbances is equal to that of the mean flow (i.e. K=1) (note that they refer to St_2 as ω_* and α as $\mathrm{Cos}^2\alpha$). Thus, the linear flame transfer functions for both the conical and wedge flames, Eqs. (41) and (43), depend upon two parameters: St_2 and η. It is useful to define a new Strouhal number based upon the convective velocity, u_c, of the flow disturbances, St_c, which naturally arises in the two transfer functions (Eqs. (41) and (43)) and equals ηSt_2:

$$\eta St_2 = KSt = \left(\frac{u_o}{u_c}\right)\left(\frac{\omega_o L_f}{u_o}\right) = \frac{\omega_o L_f}{u_c} = St_c \quad (44)$$

These two Strouhal numbers are related to the amount of time taken for a flow (St_c) and flame front (St_2) disturbance (which is ultimately created by a flow disturbance) to propagate the flame length, normalized by the acoustic period.

Before looking at the total flame transfer function, it is useful to understand the relative contribution from the boundary condition and flow forcing non-uniformities. Their ratio is given by:

$$\frac{G_{c,Flow}}{G_{c,BC}} = \frac{1-e^{i\eta St_2}+i\eta St_2}{\eta\left(e^{iSt_2}-1-iSt_2\right)} \quad (45)$$

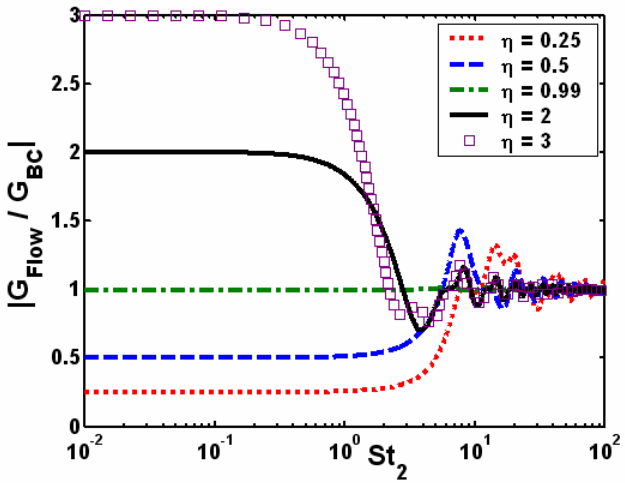

Figure 13 Strouhal number dependence of the magnitude of the ratio of the transfer functions due to the flow non-uniformity and boundary condition terms for different values of η

$$\frac{G_{w,Flow}}{G_{w,BC}} = \frac{(1-i\,\eta\,St_2)e^{i\eta St_2}-1}{\eta\left(1-(1-i\,St_2)e^{iSt_2}\right)} \qquad (46)$$

The magnitude of this ratio is identical for both wedge and conical flames, see Figure 13. The phase of this ratio is different for conical (not shown here) and wedge flames (plotted in Figure 14).

It is instructive to analyze the characteristics of this ratio for limiting values of the parameters η and St_2. First, note that in the $\eta \to 0$ limit (i.e., a spatially uniform disturbance), the flame dynamics for both the wedge and conical flames is controlled exclusively by the boundary condition term, irrespective of the Strouhal number.

$$\lim_{\eta->0}\left(\frac{G_{c,Flow}}{G_{c,BC}}\right) = \lim_{\eta->0}\left(\frac{G_{w,Flow}}{G_{w,BC}}\right) = 0 \qquad (47)$$

This result can be anticipated from the discussion in the Introduction section and reflects

the fact that only the homogeneous solution is excited when the flow disturbance is uniform.

In the $St_2 \rightarrow 0$ limit, the relative contribution of the two terms is determined by the value of the parameter η:

$$\lim_{St_2 \rightarrow 0} \left(\frac{G_{c,Flow}}{G_{c,BC}} \right) = \left(\frac{G_{w,Flow}}{G_{w,BC}} \right) = -\eta \quad (48)$$

The boundary condition and flow forcing terms dominate when $\eta<1$ and $\eta>1$, respectively. For long flames ($\beta>>1$), this physically corresponds to situations where the disturbance phase velocity is greater than and less than the mean flow velocity, respectively. The two terms tend toward equal magnitudes when $\eta = 1$[§]. These points can be clearly observed in Figure 13. Note also that the flow disturbance and boundary condition terms are 180º out of phase for low St_2 values (see Figure 14). In the intermediate Strouhal number range, say $1<St_2<10$, either the flow forcing or the boundary condition may dominate depending upon η and St_2.

In the limit of $St_2>>1$, the contribution from both the boundary conditions and flow forcing term are equal, as shown in Figure 13:

$$\lim_{St_2 \rightarrow \infty} \left(\frac{G_{c,Flow}}{G_{c,BC}} \right) = -1$$

$$\lim_{St_2 \rightarrow \infty} \left(\frac{G_{w,Flow}}{G_{w,BC}} \right) = -e^{i(\eta-1)St_2} \quad (49)$$

[§] Some care is required in analyzing this η=1 result, as the two terms tend to have equal magnitudes and are 180 degrees out of phase. The overall response is not zero, however, as the common denominator (η-1) in Eqs. (41) and (44), which has been cancelled out when taking their ratio, causes their sum to have a non-zero value.

Equation (49) also shows that, in this limit, the relative magnitude contribution of these two terms is independent of η (assuming that the ηSt_2 product does not simultaneously go to zero). Furthermore in the limit of St_2>>1, the two terms are always out of phase for conical flames, irrespective of the Strouhal number and η. In contrast, for wedge flames the phase difference between the two contributions monotonically increases with St_2, as shown in Figure 14 (the shaded bands in the figure indicate regions of constructive interference).

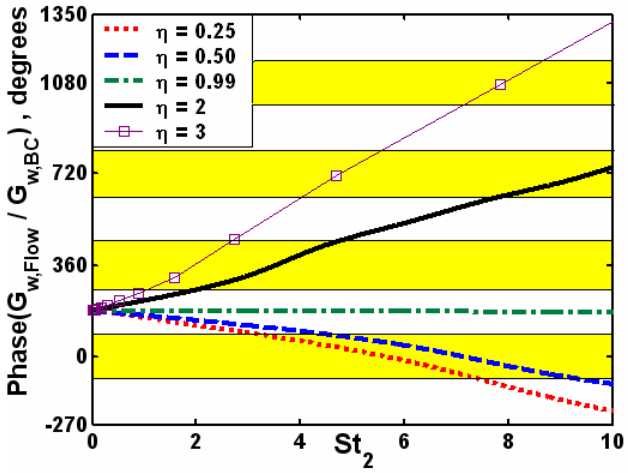

Figure 14 Strouhal number dependence of the phase of the ratio of the transfer functions due to the flow forcing and boundary condition terms for wedge flames. Shaded regions indicate points where boundary condition and flow non-uniformity terms are in phase

4.2.1.1.3 *Flame Area-Velocity Transfer Function: Overall Features*

The dependence of the magnitude and phase of the total conical flame transfer function $G_c\left(St_2,\eta\right)$ upon St_2 at several η values is plotted in Figure 15 and Figure 16, respectively. Consider the magnitude results first. As previously noted by Schuller *et al.* [35], the transfer function gain is identical in the cases where η = 0 or 1. Physically, this

corresponds to cases where the disturbance velocity is uniform, η=0 or its phase speed matches the flame front disturbance velocity, η=1. The gain transfer function differs for all other disturbance phase velocity cases. Note also that the gain value is always less than one and generally decreases monotonically with St_2, although there is some ripple at higher St_2 values due to constructive and destructive interference between $G_{c,Flow}$ and $G_{c,BC}$. The transfer function phase starts at zero degrees at low St_2 and initially increases monotonically with St_2. For the η=0 case, the phase tends to a limiting value of 90º for large St_2 (see Figure 16). In all other cases, the phase monotonically increases and for high values of η and St_2 the phase curves collapse into a single line.

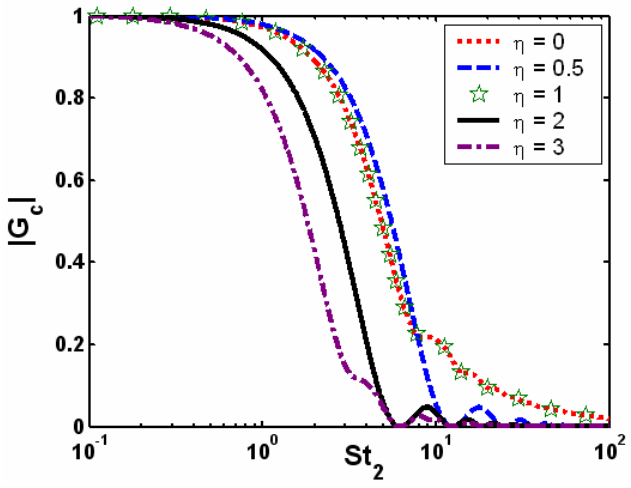

Figure 15 Axisymmetric conical linear transfer function $G_c(St_2,\eta)$ magnitude dependence upon the reduced Strouhal number (St_2) for different values of η

For wedge flames, the gain and phase of the flame transfer function $G_w(St_2,\eta)$ are shown in Figure 17 and Figure 18 respectively. Note that, similar to conical flames, all gain values tend toward values of unity at low St_2. However, only in the uniform velocity case, η=0, does the gain then decrease with increases in St_2, as might be expected. In all other cases, the gain increases to values of greater than unity, due to the constructive

superposition of $G_{w,Flow}$ and $G_{w,Bc}$. This amplification of the flame response over its quasi-steady value was previously predicted by Schuller *et al*. [35] and confirmed in measurements by Durox *et al*. [23]. The magnitude and St_2 value of the peak value of this amplification region is controlled by η. As shown in Figure 17, the magnitude of the peak value of G_w initially increases from unity as η increases with zero, reaches a maximum at η=1, and then decreases back to unity with further η increases. Turning to the phase in Figure 18, note that the phase increases with St_2 with similar characteristics for all η values. To summarize, η (along with St_2) plays a significant role in determining the effect of superposition between flow disturbance non-uniformity and boundary conditions. This point is key to understanding the effect of these parameters on the nonlinear flame dynamics, discussed in Section 4.2.2.

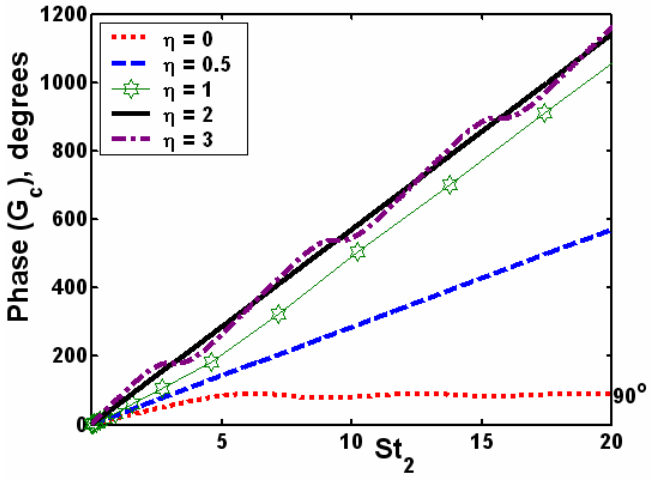

Figure 16 Axisymmetric conical linear transfer function $G_c(St_2,\eta)$ phase dependence upon the reduced Strouhal number (St_2) for different values of η

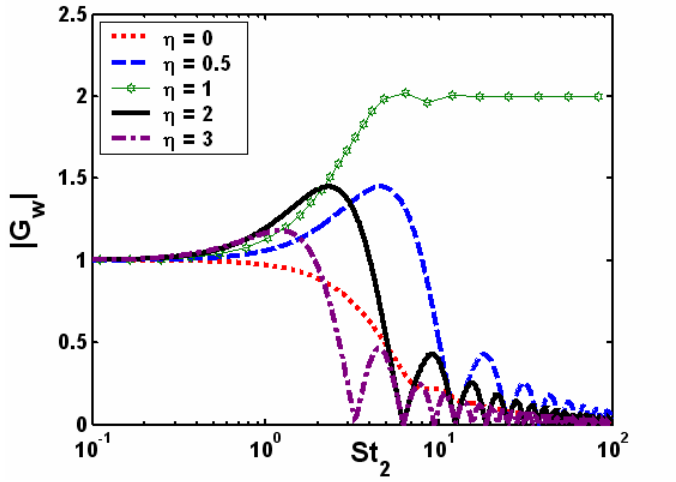

Figure 17 Axisymmetric wedge linear transfer function $G_w(St_2, \eta)$ amplitude dependence upon the reduced Strouhal number (St_2) for different values of η

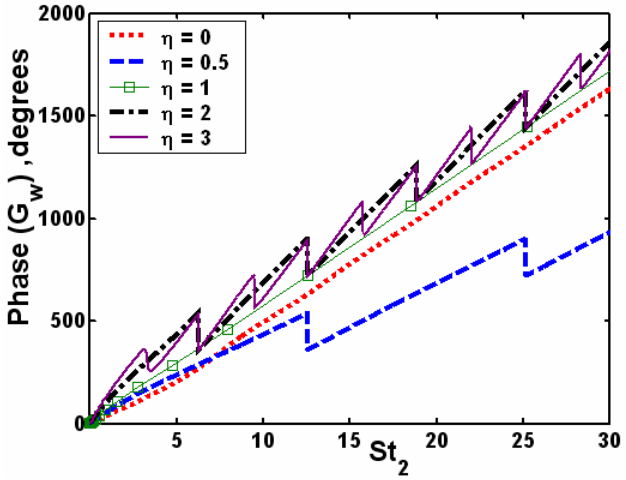

Figure 18 Axisymmetric wedge linear transfer function $G_w(St_2, \eta)$ phase dependence upon the reduced Strouhal number (St_2) for different values of η

4.2.1.2 Velocity Model B

In this section, the analysis for the flame-area transfer function based on the velocity field specified in Model B (which has an additional radial velocity component) is presented. Following the same approach as in Section 4.2.1.1, the conical flame area transfer function can be expressed as:

$$G_c = 4i\left(\frac{\eta\left(1-e^{iSt_2}\right)+e^{i\eta St_2}-1}{\eta(1-\eta)\left(2i+\beta\eta St_2\right)St_2^2}\right)$$
$$+2\beta\left(\frac{i(2\eta-1)e^{i\,\eta\,St_2}+\eta^2\left(-i+(\eta-1)St_2\right)e^{i\,St_2}-(\eta-1)^2\left(-i+\eta St_2\right)}{\eta\ (\eta-1)^2\left(2i+\beta\eta St_2\right)\ St_2^2}\right) \tag{50}$$

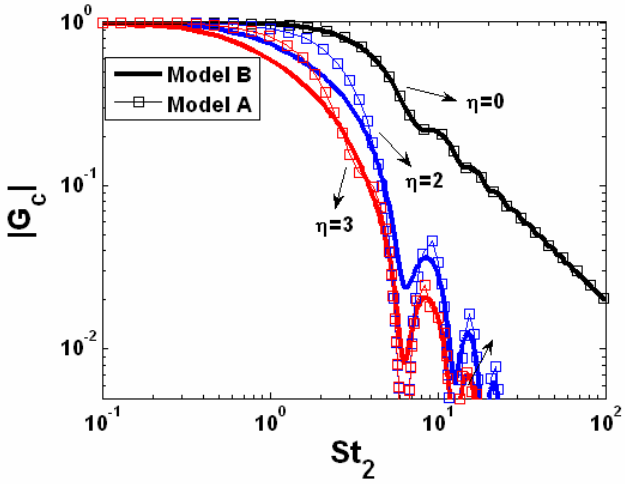

Figure 19 Axisymmetric conical linear transfer function (G_c) amplitude dependence upon the reduced Strouhal number (St_2) for different values of η, β=1

where the reference velocity for the transfer function is based upon the normal velocity at the flame base, $u'_{ref} = u'_n(y=0)\sqrt{1+\beta^2}$. In order to compare with Model A, the normal velocity is also scaled by the function of the flame aspect ratio, $\sqrt{1+\beta^2}$, so that the axial flow velocity in the two models is the same at St=0 (alternatively, u'_{ref} for model A could be defined as $u'_n(y=0)$).

Note that, similar to Eq (41), G_c can in turn be expressed as contributions from boundary conditions and flow non-uniformity as shown below.

$$G_c = \underbrace{2\left(\frac{\left(e^{iSt_2}-1-iSt_2\right)\left(2+i\beta\eta^2 St_2+\eta\left(-2+\beta-i\beta St_2\right)\right)}{\left(\eta-1\right)^2\left(-2+i\beta\eta St_2\right)\ St_2^2}\right)}_{\textit{Boundary conditions}} + \underbrace{2\left(\frac{e^{i\eta St_2}\left(2-2\eta+\beta\left(2\eta-1\right)\right)+2\left(\eta-1\right)\left(1+i\eta St_2\right)+\beta\left(1+\eta^3 St_2^2+\eta\left(i-\eta St_2\right)\left(2i+St_2\right)\right)}{\eta\left(\eta-1\right)^2\left(2-i\beta\eta St_2\right)St_2^2}\right)}_{\textit{Flow non uniformity}}$$

(51)

The transfer function gains based on Models A and B are compared in Figure 19. It can be seen that the results are identical for η=0, but differ for other η values. However, these differences are not substantive – note the similar qualitative behavior of the cases for Model A and B for all η values. Similarly, the phase predictions are very similar for both the velocity models (see Figure 20). Furthermore, as will be shown in the next section, see Figure 21, the nonlinear flame response for Model A and B are also quite similar.

The perturbation velocity magnitude for Model B varies along the flame, in contrast to Model A. In this case, some care is required in defining a physically useful reference velocity, u'_{ref}, for the transfer function, see also the discussion in Ref. [39]. For example, if the perturbation velocity magnitude is near zero at the base of the flame, but has much larger values everywhere else, then clearly defining the transfer function based upon the perturbation velocity at the flame base will lead to physically misleading results. In the same way, if only the axial velocity were used in the transfer function in Eq (50), G_c would initially grow with St_2 because of the corresponding increase in radial velocity (see Eq (28)). Such behavior does not reflect any new physical phenomenon, but is only an artifact of the choice in normalization velocity. Similarly, the appropriate definition of

reference velocity is different for conical and wedge flames, because of the significantly different spatial distribution in flame area. This point emphasizes the need for careful consideration of reference velocity when comparing flame transfer functions across different perturbation velocity fields or geometries.

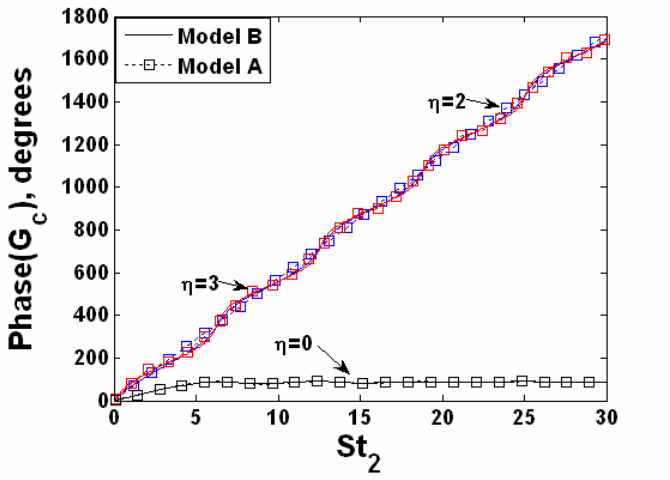

Figure 20 Axisymmetric conical linear transfer function (G_c) phase dependence upon the reduced Strouhal number (St_2) for different values of η, β=1

The close similarities between the results of Model A and B provides a very helpful insight for modeling flame dynamics. Specifically, it shows that a detailed spatial characterization of the perturbation velocity field is not needed in order to obtain a reasonable quantitative and qualitative description of the flame response (assuming appropriate normalization velocities for the transfer function are used for comparisons, as detailed above). This result can be understood from Eq (7), which shows that the flame area dynamics are controlled by (1) the perturbation velocity normal to the flame and (2) the spatial scale over which the perturbation velocity varies. As long as the two disturbance velocity fields are similar in these two respects, this discussion shows that the resulting flame area response is also similar. This is a helpful result for the present study,

whose goal is not to simulate the exact disturbance field of any particular experimental setup, but rather to elucidate the key physical processes and non-dimensional parameters that influence the flame's dynamics. This shows that such insight can be gained from simplified representations of the velocity field, as long as they retain the two critical components noted above.

4.2.2 Nonlinear Flame Dynamics

Before considering specific results in the nonlinear case, several general conclusions can be drawn from analysis of the governing equation. Note that nonlinearities in the flame area response arise from three sources. The first is the nonlinear flame dynamics, through the term $\sqrt{1+\beta^2\left(\partial\zeta/\partial r\right)^2}$ in Eq. (19). The second is the static nonlinearity introduced through the dependence of the flame area upon flame position gradient through a term with the same form, $\sqrt{1+\beta^2\left(\partial\zeta/\partial r\right)^2}$ (see Eq. (40)). In both of these cases, the nonlinearity is purely geometric in origin and is introduced by the relationship between the instantaneous flame front normal and flame position gradient. The third nonlinearity is due to the flow forcing itself, and is due to the dependence of the disturbance velocity at the flame front upon the flame position, $u(\zeta,t)$.

The fact that the first two sources of nonlinearity are identical can be used to write the final expressions for the flame area in a revealing form. By substituting Eq. (19) in the expressions for flame area, the term $\sqrt{\left(1+\beta^2\left(\partial\zeta/\partial r\right)^2\right)/\left(1+\beta^2\right)}$ which appears in both the area integrals can be written as:

$$\sqrt{\frac{1+\beta^2\left(\frac{\partial\zeta}{\partial r}\right)^2}{1+\beta^2}} = u(\zeta,t) - \frac{\partial\zeta}{\partial t} \qquad (52)$$

Thus, *the explicit form of the nonlinearity disappears*. Nonlinearities in flame front dynamics are included in the $\partial\zeta/\partial t$ term (note that the flow forcing nonlinearities also effect $\partial\zeta/\partial t$, as shown in Eq. (19)), while those due to the flow forcing nonlinearity noted above are included in the *u(ζ,t)* term. Based upon Eq. (52), the following observations can be made regarding the effects of various parameters upon nonlinearity in the flame's response to flow perturbations.

Strouhal Number: At low Strouhal numbers, *St*, the unsteady term in Eq. (52) is negligible. Moreover, the ζ dependence of the velocity field, *u(ζ,t)*, is weak, at least for the velocity fields considered here. Thus, the flame area's velocity response remains linear for low Strouhal numbers, as *St* is the dimensionless ratio of the flame response time to perturbation period. This point shows that the flame's *nonlinear area response is an intrinsically dynamic phenomenon; its quasi-steady response is linear*.

Flow Uniformity: Nonlinearities in the *u(ζ,t)* term are directly due to non-uniformity in flow disturbances. Thus, the contribution of this term to flame area nonlinearities is suppressed in the $\eta\rightarrow 0$ limit.

Boundary conditions: If the flame remains anchored at the attachment point, as it is in this study, then $\partial\zeta/\partial t$ is identically zero at this point for all time. As such, the flame area perturbations in the vicinity of the attachment point (where $\zeta\approx 0 \Rightarrow u\approx u(0,t)$) exhibit a linear dependence upon velocity amplitude. Nonlinearities grow monotonically in

magnitude with downstream distance from the attachment point. As such, the axisymmetric conical flame exhibits a more linear response than the axisymmetric wedge flame for comparable values of ε, since most and very little, respectively, of the flame area is concentrated near the attachment point, where the flame dynamics are linear. This discussion also shows the potential coupling between the flame kinematic and flame holding sources of nonlinearity.

Flame Aspect Ratio: β is an important nonlinearity parameter for this problem since the flame dynamics become linear when β>>1; i.e., when the flame is very long. This can be seen by noting that the left side of Eq. (19) becomes linear in this case: $\sqrt{1+\beta^2\left(\partial\zeta/\partial r\right)^2} = \pm\beta\,\partial\zeta/\partial r$. In this case, the flame dynamics are linear, although the flow forcing term need not be.

As discussed in Sec. 4.1.2 in the context of linear flame dynamics, different velocity fields with similar spatial scales of variation and surface area weighted normal velocities will give similar flame responses. This point also carries over to the nonlinear flame dynamics, as illustrated in Figure 21, which plots the dependence of the flame area response upon perturbation velocity amplitude for Model A and B, showing that the results are almost identical.

Next, we derive an expression for the lowest order nonlinear correction to the flame area-velocity transfer function using Model A. Returning to the perturbation expansion for the flame position in Eq. (33), the following equations describe the dynamics of the second and third order correction terms, ζ_2 and ζ_3:

$$\frac{\partial \zeta_2}{\partial t} - \alpha \frac{\partial \zeta_2}{\partial r} + \frac{\alpha(1-\alpha)}{2}\left(\frac{\partial \zeta_1}{\partial r}\right)^2 + \zeta_1 KSt \;\; Sin[\, St\{\, K(1-r) - t\,\}] = 0$$

$$\frac{\partial \zeta_3}{\partial t} - \alpha \frac{\partial \zeta_3}{\partial r} + \frac{\alpha^2(1-\alpha)}{2}\left(\frac{\partial \zeta_1}{\partial r}\right)^3 + \alpha(1-\alpha)\left(\frac{\partial \zeta_1}{\partial r}\right)\left(\frac{\partial \zeta_2}{\partial r}\right) + \frac{{\zeta_1}^2 K^2 St^2}{2} \;\; Cos[\, St\{\, K(1-r) - t\,\}]$$
$$+\zeta_2 KSt \; Sin[\, St\{\, K(1-r) - t\,\}] = 0 \tag{53}$$

The solution of Eq. (53), subject to the boundary condition in Eq. (22), is given in Appendix C. In the ensuing discussion, we focus upon the total heat release response. Defining the conical flame area-velocity transfer function at the fundamental frequency as $G_{c,\omega_o} = \dfrac{A_c'(\omega_o)/\bar{A}_{c,o}}{u'(\omega_o)/u_o}$ yields:

$$G_{c,\omega_o} = G_{c,Lin} + \varepsilon^2 \left(\frac{\tilde{A}_{c,\omega_o} \;\; e^{i\,K\alpha\,St_2}}{8 \;\; K\alpha^3 \;\; (K\alpha-1)^5 \, St_2^2} + \frac{\tilde{B}_{c,\omega_o} \;\; e^{i\,St_2}}{8 \;\; \alpha^2 \;\; (K\alpha-1)^5 \, St_2^2} + \right.$$
$$\frac{\tilde{C}_{c,\omega_o} \;\; K \;\; (\alpha-1) \;\; e^{i\,(2-K\alpha)\,St_2}}{8 \;\; (K\alpha-2)^3 \;\; (K\alpha-1)^5 \, St_2^2} + \frac{\tilde{D}_{c,\omega_o} \;\; K^2 e^{i\,(2K\alpha-1)\,St_2}}{8 \;\; (2K\alpha-1)^2 \;\; (K\alpha-1)^5 \, St_2^2} \tag{54}$$
$$\left. + \; \frac{\tilde{E}_{c,\omega_o}}{2K\alpha^3 (K\alpha-2)^3 (2K\alpha-1)^2 \;\; St_2^2} \right)$$

where $G_{c,Lin}$ refers to the linear transfer function, Eq. (41). The coefficients $\tilde{A}_{c,\omega o}$ - $\tilde{E}_{c,\omega o}$ in this expression are defined in Appendix D.

Similarly, the wedge flame area transfer function is:

$$G_{w,\omega_o} = G_{w,Lin} + \varepsilon^2 \left(\frac{\tilde{A}_{w,\omega_o} \;\; e^{i\,K\alpha\,St_2}}{8 \;\; K\alpha^3 \;\; (K\alpha-1)^5 \, St_2^2} + \frac{\tilde{B}_{w,\omega_o} \;\; e^{i\,St_2}}{8 \;\; \alpha^2 \;\; (K\alpha-1)^5 \, St_2^2} + \right.$$
$$\left. \frac{\tilde{C}_{w,\omega_o} \;\; K \;\; (\alpha-1) \;\; e^{i\,(2-K\alpha)\,St_2}}{8 \;\; (K\alpha-2)^3 \;\; (K\alpha-1)^5 \, St_2^2} + \frac{\tilde{D}_{w,\omega_o} \;\; K^2 e^{i\,(2K\alpha-1)\,St_2}}{8 \;\; (2K\alpha-1)^2 \;\; (K\alpha-1)^5 \, St_2^2} \right.$$

$$+ \frac{\tilde{E}_{w,\omega_o}}{2K\alpha^3(K\alpha-2)^3(2K\alpha-1)^2 \ St_2^2}\Bigg) \tag{55}$$

The conical transfer functions evaluated using the analytical result, Eq. (54), are compared with numerical simulations for a representative case in Figure 21. Although not shown, comparable results are obtained for wedge flames using Eq. (55). Non-linearity is enhanced as the velocity amplitude or the Strouhal number increases. As expected, the perturbation analysis is accurate at higher velocity amplitudes when the Strouhal number is low.

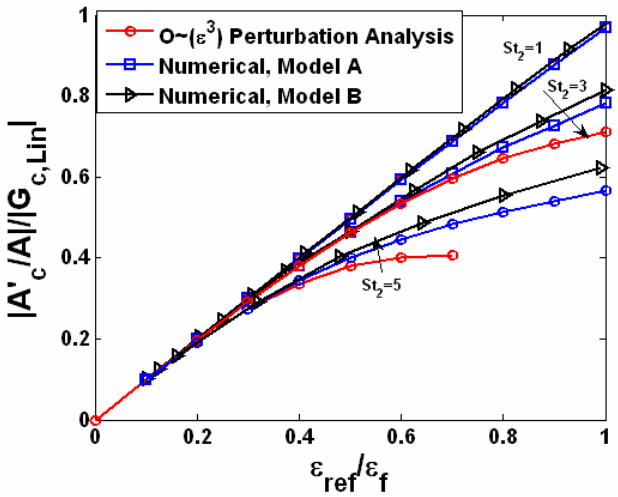

Figure 21 Dependence of flame area fluctuations upon disturbance velocity amplitude for axisymmetric conical flames at η=1, where $\varepsilon_{ref} = u'_{ref} / u_o$.

The linear component of the transfer function in Eq. (54) and (55) is described by only two parameters; i.e. $G_{Lin} = G(St_2, \eta)$. For the general nonlinear case, the gain G is also a function of ε and β; i.e., $G = G(St, K, \varepsilon, \beta)$. Also, as can be seen from the contribution of the non-linear terms to the transfer function in Eqs. (54) and (55), two new characteristic

time scales arise which are represented by the non-dimensional terms: $(2-K\alpha)St_2 = 2St_2 - St_c$ and $(2K\alpha-1)St_2 = 2St_c - St_2$. As discussed in the previous section, the linear transfer function can be explicitly decomposed into contributions from boundary conditions and flow forcing non-uniformities. The boundary conditions and flow non-uniformities give rise to the characteristic times represented by the terms containing St_2 and St_c, respectively. When the analysis is extended to the non-linear regime, the same conclusions can be reached regarding the origin of the time scales represented by the terms St_2 and St_c (the terms with the coefficients $\tilde{B}_{\omega_o}$ and $\tilde{A}_{\omega_o}$ in Eqs. (54) and (55)). In addition, the time scale represented by the terms $(2K\alpha-1)St_2$ and $(2-K\alpha)St_2$ arises as a result of the nonlinear interaction between these two sources of flame disturbance. Hence, to the order of approximation considered here, the nonlinear characteristics of the flame dynamics are controlled by the superposition of the flame disturbances represented by the terms: St_2, St_c, $2St_2-St_c$ and $2St_c-St_2$.

As anticipated earlier, the nonlinear flame dynamics is qualitatively different depending upon whether the flame disturbances have a single or multiple characteristic time scale. The ensuing discussion will consider the former case first, and the multiple time scale case next.

Consider the two limiting cases, $\eta=0$ and $\eta=1$, wherein all the above discussed time scales (albeit for different reasons) reduce to a single one represented by the term St_2. Recall from the prior discussion that the flame dynamics in the uniform velocity case ($\eta=0$) is exclusively controlled by the boundary condition. In this case, the transfer function expressions reduce to:

$$\lim_{\eta\to 0} G_{c,\omega_o} = \frac{2\left(1-e^{i\,St_2}+iSt_2\right)}{St_2{}^2} - \varepsilon^2(1-\alpha)\left(\frac{6\alpha+iSt_2+2i\alpha St_2+e^{i\,St_2}(-6\alpha-iSt_2+4i\alpha St_2+(\alpha-1)St_2^2)}{4St_2^2\alpha^2}\right) \tag{56}$$

$$\lim_{\eta\to 0} G_{w,\omega_o} = \frac{2\left(-1+e^{i\,St_2}(1-iSt_2)\right)}{St_2^2} - \varepsilon^2(1-\alpha)\left(\frac{6\alpha(-1+e^{i\,St_2}-iSt_2e^{i\,St_2})-3\alpha St_2^2e^{i\,St_2}+i(\alpha-1)St_2^3e^{i\,St_2}}{4St_2^2\alpha^2}\right) \tag{57}$$

Note that in the limit of long flames ($\beta>>1 \Rightarrow \alpha\to 1$), the non-linear contribution to the transfer function disappears for both conical and wedge flames. This result was anticipated in the discussion at the beginning of this section.

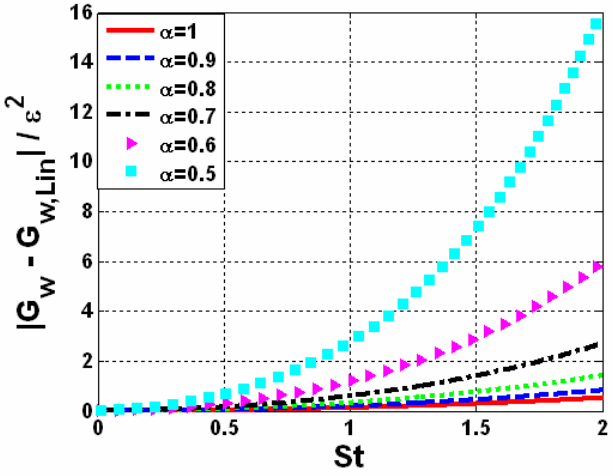

Figure 22 Dependence of non-linear part of the transfer function for axisymmetric wedge flames at η=1

Figure 22 shows the variation of the non-linear part of the transfer function for wedge flames as a function of the Strouhal number when η=1 for different values of α. As expected, for low Strouhal numbers ($St\to 0$), the contribution from the non-linearities

goes to zero. This is due to the absence of any destructive interference effect leading to a monotonic increase in the nonlinear contribution with increasing Strouhal number. Moreover, the contribution to the gain is substantially enhanced as the flame gets shorter (i.e. lower values of α) consistent with the *Flame Aspect Ratio* argument in the introduction of this section.

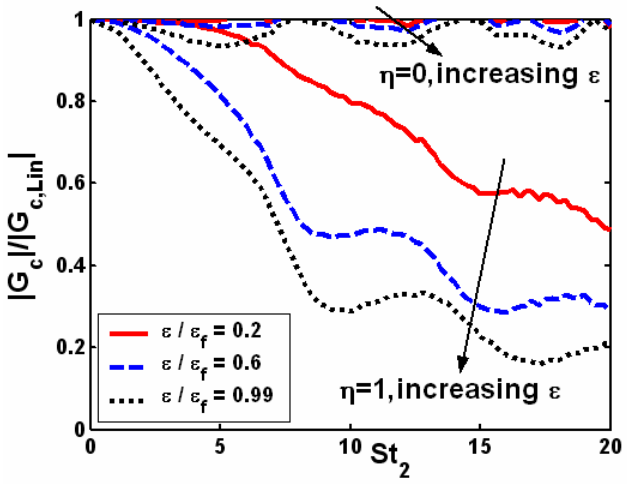

Figure 23 Strouhal number dependence of the ratio of the magnitude of the flame area-velocity transfer function to its linear value for the axisymmetric conical flame, β=2

Hence the presence of a single characteristic time scale, for the η=0 and η=1 cases, causes the nonlinear contribution to monotonically increase with increasing Strouhal number and/or decreasing flame aspect ratio. As discussed further below, *it is only for these two cases that the non-linearities always lead to a reduction in the magnitude of the total transfer function*. These conclusions are valid even at higher velocity amplitudes as shown by numerical simulations in Figure 23-Figure 25, which plot the St_2 dependence of the gain and phase of the nonlinear transfer function upon St_2. The gain transfer functions are normalized by their linear values, G/G_{Lin}. Results are shown for two convective wave

speeds, η=0 and η=1, allowing for a convenient comparison of the effects of nonlinearities from boundary conditions alone, and the combined effect of boundary conditions and flow disturbance non-uniformity. Consider the gain curves first, Figure 23 and Figure 25. As predicted earlier, the response tends to its linear value in all cases at low St_2. In the η=0 case, nonlinear effects are more apparent at high St_2. For the wedge flame in Figure 25 the response is considerably nonlinear even at moderate values of Strouhal number. The enhanced nonlinear response of wedge over cone flames is explained by the *Boundary Conditions* argument discussed earlier.

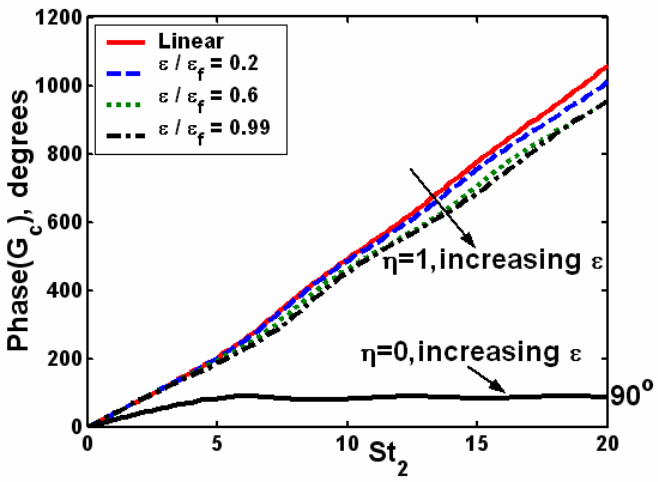

Figure 24 Strouhal number dependence of the phase of the flame area-velocity transfer function for the axisymmetric conical flame, β=2.

Turning to the η=1 case, note the substantial reduction in flame area relative to its linear value; i.e., there is a substantial degree of gain saturation. Although plotted in a different form, the resulting gain curves look quite similar to the qualitative plot of $H_n(\varepsilon)$ in Figure 3. In agreement with the *Strouhal Number* argument discussed earlier, the degree of nonlinearity increases with St_2. As shown in Figure 23 and Figure 25, the gain

for the conical and wedge flames decreases by about 80% and 85% respectively (at $\varepsilon=\varepsilon_f$ in the St_2= 20 and η= 1 case). In contrast, the gain never drops below 5% of its linear value for conical flames and 55% of its linear value for wedge flames in the η=0 case. Moreover, unlike the η=0 case, the phase of the area response for both the conical (see Figure 24) and wedge flames (not shown here) exhibits a strong amplitude dependence. These results indicate the extent to which flow non-uniformities can significantly modify the nonlinear flame response.

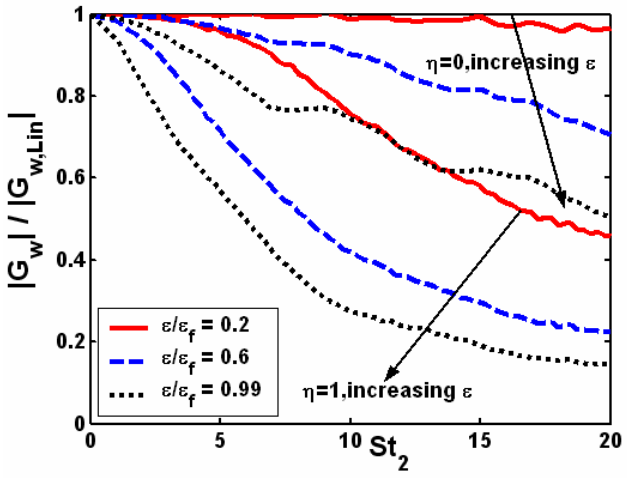

Figure 25 Strouhal number dependence of the ratio of the magnitude of the flame area-velocity transfer function to its linear value for the axisymmetric wedge flame, β=2

Next, consider the case where $\eta\neq0$ or 1 and the flame dynamics are controlled by the superposition of flame disturbances with the four different characteristic time scales discussed earlier. In contrast to the above results, interactions between the boundary condition and flow forcing non-uniformity solutions causes a non-monotonic variation in the transfer function gain with disturbance amplitude. To illustrate, Figure 26 shows the flame response for a wedge flame when η=2 (i.e. α=0.8 and disturbances are traveling at $0.4u_o$). Note that the gain results are not normalized by their linear value here. The gain

result indicates that in the $5<St_2<8$ range, the nonlinear transfer function actually *exceeds* its linear value. This result can be understood by noting that this behavior occurs in the vicinity of the regions where the linear transfer function achieves a minima. At these St_2 values, the contributions from the boundary conditions and the flow forcing terms destructively interfere, leading to low linear gains. As the velocity amplitude is increased, nonlinearities cause the gain due to both the boundary conditions and the flow forcing terms to decrease. However, since the relative "ages" of the two disturbances are unequal, the discussion in the context of Figure 7 shows that the magnitude of their gain reductions is different. Since the individual gain decreases by different amounts, the total gain does not go to zero at the St_2 value at which the linear gain is zero, but actually shifts to a higher St_2 value in the $\varepsilon=0.2\varepsilon_f$ case. At higher disturbance levels, the two terms never exactly cancel and the gain does not go to zero. Rather, there is a monotonic decrease in the gain of the transfer function with increase in velocity amplitude. Analogous behavior also occurs in conical flames, although less dramatically.

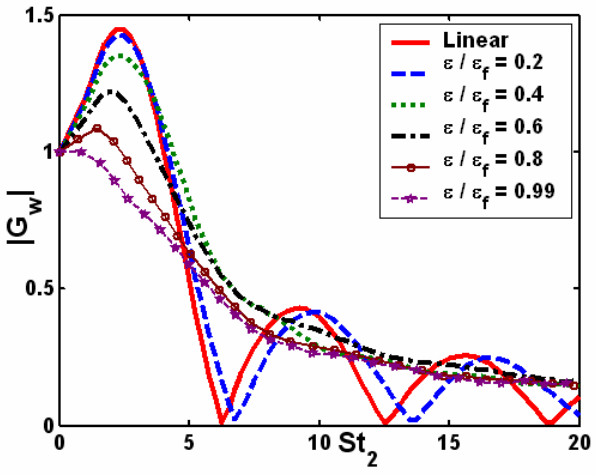

Figure 26 Strouhal number dependence of the magnitude of the flame area-velocity transfer function for the axisymmetric wedge flame, $\beta=2,\eta=2$

These predictions can be compared to related measurements of Durox *et al*. [23] on wedge flames, where the phase speed of the disturbances was half the mean flow speed. They obtained measurements at four forcing amplitudes ε~0.05-0.2 and β~5.6. Interestingly, they found both increases and decreases in the transfer function gain with changes in disturbance amplitude, depending upon Strouhal number. Their results are reproduced in Figure 27. The transfer functions plotted here equals the ratio of the fluctuating CH^* emission intensity to the velocity disturbance amplitude slightly above the burner exit. Note the strong similarities between their measurement and the predictions from Figure 26. In the $2<St_2<5$ regions where the transfer function exceeds unity, the nonlinear gain monotonically decreases with disturbance amplitude. In the $5<St_2<8$ range, the nonlinear transfer function first increases with disturbance amplitude, then decreases. This trend is quite consistent with the predictions of this study.

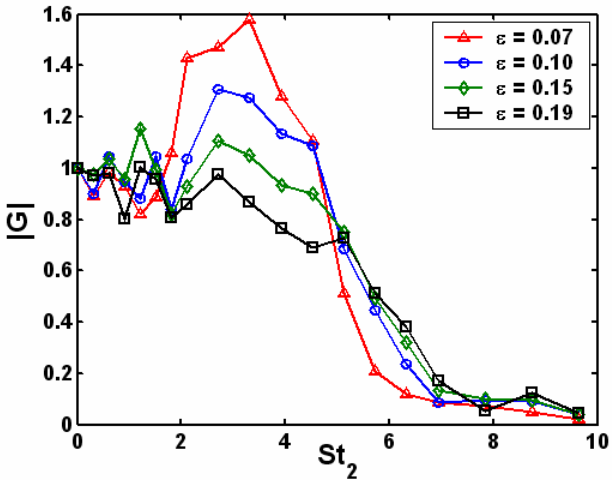

Figure 27 Experimentally measured gain for an inverted conical flame for a mean velocity u_o= 2.05 m/s, ϕ = 0.92. Data reproduced from Durox *et al.* [23]

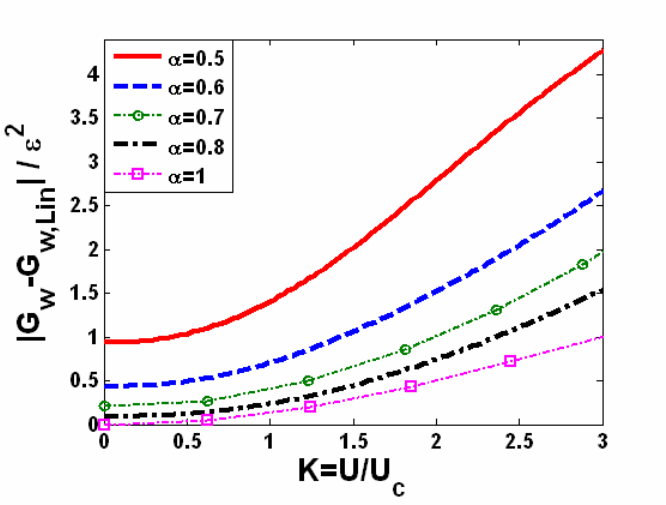

Figure 28 Dependence of non-linear part of the transfer function on the phase speed of the disturbances (K) for axisymmetric wedge flames, *St*=1

Using the perturbation analysis, the non-linear contribution to the wedge flame transfer function is shown for varying phase speeds at unity Strouhal number in Figure 28. *It shows that the non-linear contribution is higher when the phase speed of the disturbances is less than the mean flow speed (i.e. K>1)* in comparison to the case wherein 0<*K*<1. This is a direct manifestation of the *Flow Uniformity* argument discussed earlier. As noted earlier, non-linearity decreases with increase in the flame aspect ratio (i.e. increasing α), consistent with the *Flame Aspect Ratio* argument. Note that this result is valid for a low Strouhal number case wherein the linear gain does not go to zero for both the conical and wedge flames. Hence, the gain monotonically decreases with increasing disturbance amplitude. However, for higher Strouhal numbers, the linear gain goes to zero at certain η values. It is only in the vicinity of these η values that we find the corresponding increase in nonlinear flame transfer function. This result prominently highlights the sensitivity of the flame response to the phase speed of the disturbances.

Moreover, it demonstrates how the competition between boundary condition and flow nonuniformity terms can significantly impact the flame response behavior.

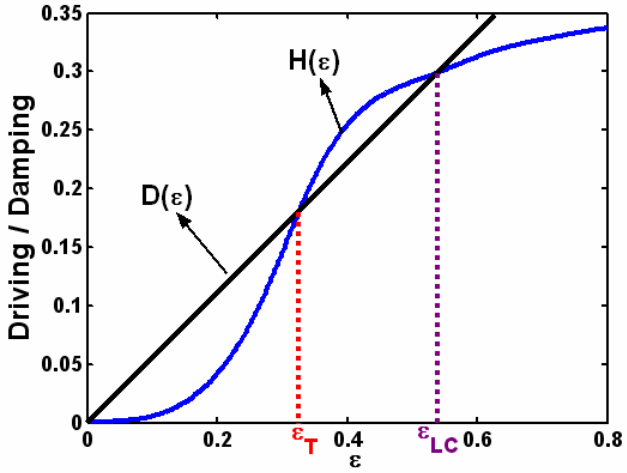

Figure 29 Dependence of acoustic driving, H(ε) (where H(ε) is equated for this example to $A_w'/\bar{A}_w$) and damping, D(ε), processes upon velocity amplitude ε, for wedge flames at St_2=6.25 with K=2, α =0.8

These results have important applications upon the type of bifurcations which may be observed in unstable combustors. In situations where the amplification and damping curves resemble that qualitatively shown in Figure 3, only supercritical bifurcations will occur and a single stable limit cycle amplitude, ε_{LC} is possible. In situations where the gain exceeds, then is less than, the linear gain (see Figure 26); i.e., it exhibits an inflection point, multiple stable solutions for the instability amplitude may exist, and sub-critical bifurcations are possible. This can be seen from Figure 29, which plots the dependence of $A_w'/\bar{A}_w$ vs ε for St_2=6.25, K=2.5, α=0.8. This curve represents $H(\varepsilon)$. A hypothetical damping curve, $D(\varepsilon)$ is also drawn in Figure 29. Note the 3 intersection points, two of which are stable, ε=0 and $\varepsilon=\varepsilon_{LC}$, and one of which is unstable, $\varepsilon=\varepsilon_T$. In this case two equally valid solutions are possible, ε=0 or $\varepsilon=\varepsilon_{LC}$, which one the system is actually at depends upon initial conditions. Such a system will manifest characteristics

such as hysteresis and triggering (i.e., the destabilization of a linearly stable system by a sufficiently large disturbance [57].

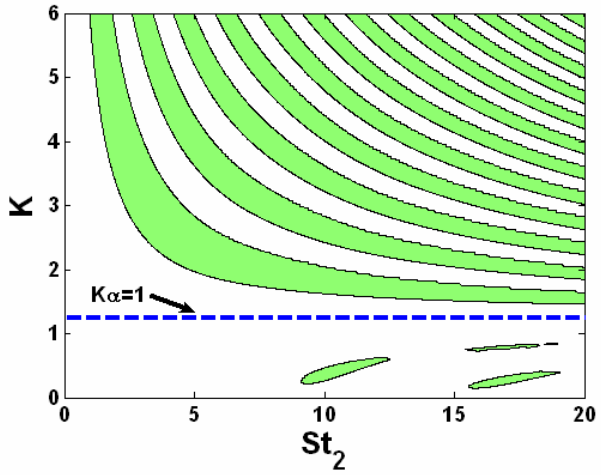

Figure 30 Qualitative representation of regions where nonlinear flame transfer exceeds (shaded) or is less than (white) linear transfer function, α=0.8,ε=0.1

The regions in parameter space (defined by K and St_2), where the nonlinear transfer function has an inflection point can be determined from the analytical solutions and is shown in Figure 30. The plot shown is for a wedge flame with an aspect ratio α=0.8, ε=0.1. *Note that an inflection point is most likely to exist when the phase speed of the disturbances is less than the mean flow speed (K>1).* This is in accordance with the earlier discussion which showed that non-linear effects were enhanced for K>1.

Finally, a brief comment on the response of the flame at the first harmonic of the forcing frequency. The previous discussion about the role played by the phase speed of the disturbances, Strouhal number and the flame aspect ratio upon nonlinearity in flame response is directly applicable here as well, since excitation of harmonics is another manifestation of nonlinearity. The analytical expressions for the flame response at ω= $2\omega_o$ are provided in Appendix E.

4.2.3 Flame Length

The changes in the average flame characteristics (such as its location and length) with increasing disturbance amplitude have been reported in many experimental studies [24,25,9]. These changes are indicative of non-linear effects and have potentially important effects upon the flame transfer function phase because they change the time delay between when a disturbance is created and when it encounters the flame. For example, Bellows *et al*. [9] observed a monotonic increase in the velocity-CH* chemiluminescence transfer function phase with disturbance amplitude and suggested it was due to the corresponding increase in flame length.

Using the perturbation analysis, the average flame length normalized by its steady state value, L_f can be expressed as:

$$L_{avg} = 1 + \varepsilon^2 \frac{\left(\alpha\left(K\alpha - 1\right)\left(-1 + \alpha + 2K\alpha + \left(\alpha - 3\right)K^2\alpha^2\right)St_2 + 2\alpha^3 K\left(K-1\right)Sin\left[\left(K\alpha - 1\right)St_2\right]\right)}{4\alpha^3\left(K\alpha - 1\right)^3 St_2} \quad (58)$$

As shown in Eq. (58), the contribution of the non-linearities to the flame length is a function of the velocity amplitude, flame aspect ratio, Strouhal number and the phase speed of disturbances, i.e. $L_{avg}=L_{avg}(\varepsilon,\alpha,St,K)$. In order to highlight the effect of each of these terms, we consider various limits. In the limit of η=1, Eq. (58) reduces to:

$$\lim_{\eta \to 1} L_{avg} = 1 - \varepsilon^2 \frac{(1-\alpha)(3+St_2^{\,2})}{12\alpha^2} \quad (59)$$

Eq. (59) predicts that L_f decreases with increasing Strouhal number (note that α<1) and velocity amplitude. Moreover this effect is amplified with decreasing flame aspect ratio,

α.

In the limit of low Strouhal numbers, the average flame length can be expressed as:

$$\lim_{St->0} L_{avg} = 1 - \varepsilon^2 \frac{(1-\alpha)}{4\alpha^2} \quad (60)$$

Equation (60) indicates that, at low Strouhal numbers, the average flame length is a function of only ε and flame aspect ratio and *is independent of the phase speed of the disturbances (K) and frequency (St)*. Moreover if the flame is long (i.e. $\alpha \rightarrow 1$), the effect of non-linearities disappear (see Eq. (60)) and the average flame length remains constant.

Another interesting feature is that for uniform disturbance velocity (K=0), or when the phase speed and mean flow speed are equal (K=1), *the average flame length is independent of the Strouhal number*, i.e.:

$$\lim_{K->0} L_{avg} = \lim_{K->1} L_{avg} = \lim_{St->0} L_{avg} \quad (61)$$

The discussion above is in conformity with experiments reported by Durox *et al*. [25], wherein a reduction in the average flame length was observed with increased velocity amplitudes. Their experiments were conducted at a frequency of 1000 Hz, α ~0.5 and a range of velocity amplitudes. The present analysis indicates that for α~0.5, the average flame length decreases, irrespective of the frequency and phase speed of the disturbances. Similar agreement is obtained with the results of Bourehla and Baillot [24] under conditions where their measured velocity profiles are similar to those considered here. These conditions correspond to K~1-2, St_2~8-12 and K=0, St_2>23.

4.3 Remarks

One of the key points made in this chapter is that the linear and nonlinear characteristics of the flame dynamics are controlled by the interaction between flame disturbances due to boundaries and flow non-uniformities. A constructive superposition of the two flame disturbance contributions can cause the flame to act as an "amplifier" at certain frequencies whereas a destructive superposition can cause the flame response to be identically zero.

In the nonlinear regime, the flame response is critically dependent on whether the solution lies in a region of constructive or destructive interference of the flame disturbances. In regions of constructive interference, the nonlinear flame transfer function gain is always less than its linear value whereas in regions of destructive interference the nonlinear transfer function may exceed its linear value. These characteristics can cause the same combustor to exhibit sub-or supercritical type of bifurcation depending on the operating condition. The analysis shows that nonlinearity is enhanced and that there is a greater tendency for the nonlinear transfer function to have an inflection point when the phase speed of the disturbances is less than the mean flow speed. Moreover, the average flame length decreases with increasing perturbation amplitude for most conditions, consistent with the available experimental data.

CHAPTER 5

FLAME RESPONSE: EFFECT OF STRETCH AFFECTED FLAME SPEED

An analysis of the linear response of 2D wedge and conical premixed flames is presented in this chapter, which takes into account the influence of flame stretch manifested as variations in the local flame speed along the wrinkled flame front. Results obtained from analyzing the G-equation shows that the flame response is mainly characterized by the Markstein length σ_c^* and a Strouhal number, St_2, defined as the disturbance angular frequency normalized by the time taken for a flame disturbance to propagate the flame length. Flame stretch is found to become important as the disturbance frequency satisfies $\sigma_c^* St_2^2 \sim O(1)$, i.e. $St_2 \sim O\left((\sigma_c^*)^{-1/2}\right)$. Specifically, for disturbance frequencies below this order, stretch effects are small such that the flame acts as an unstretched one. When the disturbance assumes $O(1)$ of this frequency, the transfer function, defined as the ratio of the normalized fluctuation of the heat release rate to that of velocity, is contributed mostly from fluctuations of the flame surface area, which is now affected by stretch. Finally, as the disturbance frequency increases to that of $St_2 \sim O\left((\sigma_c^*)^{-1}\right)$, i.e. $\sigma_c^* St_2 \sim O(1)$, the direct contribution from the stretch-affected flame speed fluctuation to the transfer function becomes comparable to that of the flame surface area. The present study qualitatively explains the experimentally observed filtering effect in which the flame wrinkles developed at the flame base decay along the flame surface for thermal-diffusively stable mixtures and for large frequencies

disturbances.

5.1 Results and Discussion

It is should be noted that the reason that the wedge flame has been adopted for analysis instead of the conical flame used in the experiment (see Figure 9 and Figure 10) is that the conical flame position is not analytically solvable because of the curvature at the flame tip. Thus, the evolution equation for the flame position becomes a second order nonlinear ordinary differential equation and hence can only be solved numerically. Since solutions for the wedge and conical flames differ only by a small correction term in the limit of weak stretch, discussion and conclusions for the analytically solvable wedge flame are fundamentally applicable to the conical flame except for cases where the burner diameter is of the order of the flame thickness.

5.1.1 Solutions of Flame Disturbance and Transfer Function

In this section, expressions for the location of the disturbed flame and the transfer function when the flame speed is affected by stretch are derived.

In response to the velocity disturbance, the flame position can be expanded as:

$$\begin{aligned} \zeta(r,t) &= \zeta_o(r) + \zeta'(r,t) \\ \zeta'(r,t) &= \varepsilon\zeta_1(r)e^{-iSt\cdot t} + O(\varepsilon^2) \end{aligned} \tag{62}$$

where

$$\zeta_o(r) = 1 - r \tag{63}$$

is the steady-state flame location. Substituting Eqs. (62) and (63) into Eq. (20), the flame speed relation can be expressed as:

$$\frac{S_L}{S_{L,o}} = 1 - \frac{\sigma_c \beta \zeta'_{rr}}{\left(1+\beta^2\right)^{3/2}} + \frac{\sigma_s \beta}{\left(1+\beta^2\right)^{1/2}} \left.\frac{\partial u}{\partial y}\right|_{y=\zeta} \tag{64}$$

where the subscript "*r*" denotes the spatial derivative with respect to *r*, and

$$\sigma_c = \left[1 - \frac{Ze}{2}\left(\frac{1}{Le} - 1\right)\right]\left(\frac{\delta}{R}\right) \tag{65}$$

$$\sigma_s = \frac{Ze}{2}\left(\frac{1}{Le} - 1\right)\left(\frac{\delta}{R}\right) \tag{66}$$

are the Markstein lengths related to the curvature and strain sensitivities of the flame speed, respectively. Recognizing that flame stretch is induced by aerodynamic strain, flame curvature, and flame motion, and that the curvature of the flame front can be expressed as $\zeta'_{rr} \Big/ \left(1+\beta^2\right)^{3/2}$, it is seen from Eq. (64) that in the linear limit, the individual contributions from the flame curvature and strain have been separated out, as represented by the second and third terms on the RHS of Eq. (64), respectively. Furthermore, it is seen from Eq. (65) that, as noted earlier, the flame speed is modified by the curvature through a pure curvature effect, which is independent of *Le*, and the curvature component of the nonequidiffusion-related stretch. Consequently, the nonequidiffusional effect tends to strengthen the pure curvature effect when *Le*>1, and weakens it when *Le*<1. It should also be pointed out that σ_c and σ_s become functions of frequency [58] when the time scales involving the flow oscillation and the transit time across the flame become comparable. It can be shown that, in the linear limit, the governing equation given by equation Eq. (67) is still valid except that σ_c and σ_s have to be now interpreted as frequency dependent Markstein transfer functions.

Substituting Eqs. (62)-(64) into Eq. (19) and collecting the $O(\varepsilon)$ terms, the evolution equation for the disturbed flame location ζ_1 can be derived as

$$\frac{\sigma_c\beta}{(1+\beta^2)^{3/2}}\frac{\partial^2\zeta_1}{\partial r^2}+\frac{\beta^2}{1+\beta^2}\frac{\partial\zeta_1}{\partial r}+iSt\zeta_1+\left(1-\frac{i\sigma_s KSt\beta}{\sqrt{1+\beta^2}}\right)e^{iStK(1-r)}=0 \qquad (67)$$

The solution of Eq. (67), subject to the boundary conditions in Eqs. (22) and (23), is

$$\zeta_1(r)=Ae^{L_1 r}+Be^{L_2 r}+Ce^{iSt_2\eta(1-r)} \qquad (68)$$

where

$$L_{1,2}=\frac{1}{2\sigma_c^*}\left(-1\pm\sqrt{1-4i\sigma_c^* St_2}\right), \qquad A=-\frac{C\left(L_2^2+St_2^2\eta^2 e^{L_2+iSt_2\eta}\right)}{L_2^2e^{L_1}-L_1^2e^{L_2}}$$

$$B=\frac{C\left(L_1^2+St_2^2\eta^2 e^{L_1+iSt_2\eta}\right)}{L_2^2e^{L_1}-L_1^2e^{L_2}},\ C=-\frac{1}{iSt}\left(\frac{1-i\sigma_s^* St_2\eta}{i\sigma_c^* St_2\eta^2-\eta+1}\right) \qquad (69)$$

$$St_2=St\frac{1+\beta^2}{\beta^2}, \qquad (70)$$

$$\eta=K\frac{\beta^2}{1+\beta^2} \qquad (71)$$

$$\sigma_c^*=\frac{\sigma_c}{\beta\left(1+\beta^2\right)^{1/2}} \qquad (72)$$

$$\sigma_s^*=\frac{\sigma_s\beta}{\left(1+\beta^2\right)^{1/2}} \qquad (73)$$

In the above St_2, referred to as the reduced Strouhal number, combines effects of the flame aspect ratio and the Strouhal number, and can be rewritten as $\omega_o(L_f/\cos\alpha)/(u_o\cos\alpha)$, where α is the angle between the nominal flame surface,

without disturbance, and the flow direction. Thus it represents the angular frequency of the disturbance normalized by the time taken for the flame disturbance to propagate the flame length.

Recognizing that in the limit of weak stretch, i.e. $\sigma_c^* \to 0$ and $\sigma_s^* \to 0$, we have $L_2 \to -\infty$, $e^{L_1} >> e^{L_2}$ and $e^{L_1 r} >> e^{L_2 r}$ except for the region very near the flame tip ($r \to 0$), Eq. (68) can be simplified to

$$\zeta_1 = C\left[-e^{L_1(r-1)} + e^{iSt_2\eta(1-r)}\right] \tag{74}$$

Thus, hereafter we shall present the analysis based on the much simpler solution, Eq. (74) . The solutions based on the exact expressions are listed in Appendix F.

Next, we consider the total heat release of the flame. Since, by considering flame stretch, the heat release responds to the disturbance through both the flame surface area and flame speed, fluctuations of the heat release can be expressed as $Q' = Q'_A + Q'_S$ in the linear limit, where

$$Q'_S = \int S'_L d\bar{A}\,, \qquad Q'_A = \int \bar{S}_L dA' \tag{75}$$

are consequences of the fluctuations of the flame speed and flame surface area, respectively, and

$$d\bar{A} = \left(1+\beta^2\right)^{1/2} dr \tag{76}$$

$$dA' = -\frac{\beta^2}{\left(1+\beta^2\right)^{1/2}} \frac{\partial \zeta'}{\partial r} dr \tag{77}$$

$$S'_L = -\frac{\sigma_c \beta \zeta'_{rr}}{\left(1+\beta^2\right)^{3/2}} + \frac{\sigma_s \beta}{\left(1+\beta^2\right)^{1/2}} \left.\frac{\partial u}{\partial y}\right|_{y=\zeta} \tag{78}$$

Substituting Eqs. (76)-(78) into Eq. (75), yields

$$G_S = -\left\{ \frac{\sigma_c^* \beta^2}{1+\beta^2} \left[\frac{\partial \zeta_1(r=1)}{\partial r} - \frac{\partial \zeta(r=0)}{\partial r} \right] + \sigma_s^* \left(1 - e^{iSt_2 \eta} \right) \right\} \tag{79}$$

$$G_A = \frac{\beta^2}{1+\beta^2} \zeta_1(r=0) \tag{80}$$

where $G_S = \left(Q_S'/\bar{Q}\right)/\left(u'/u_o\right)$ and $G_A = \left(Q_A'/\bar{Q}\right)/\left(u'/u_o\right)$ are the transfer functions contributed from the fluctuations of the flame speed and flame surface area, respectively. The overall transfer function is then given by $G=G_S+G_A$, which depends on four key parameters: St_2, η, σ_c^* and σ_s^*.

5.1.2 Baseline Flame Response

The baseline flame response characteristics for the unstretched flame are discussed extensively in Chapter 5. Note that for the unstretched case, only the fluctuations of the flame surface area contribute to the transfer function. With $\sigma_c^* = \sigma_s^* = 0$, Eq. (74) becomes

$$\zeta_1 = i \frac{e^{iSt_2(1-r)} - e^{i\eta St_2(1-r)}}{(\eta - 1) St} \tag{81}$$

$$\lim_{\eta \to 1} \zeta_1 = \frac{(1-r)}{\alpha} e^{iSt_2(1-r)} \tag{82}$$

Substituting Eq. (81) into (80) yields the transfer function

$$G = i \frac{e^{iSt_2} - e^{i\eta St_2}}{(\eta - 1) St_2} \tag{83}$$

with the gain given by

$$|G| = 2\left|\frac{sin\frac{1}{2}(\eta-1)St_2}{(\eta-1)St_2}\right| \tag{84}$$

Figure 31 shows the dependence of the gain of the transfer function, $|G|$, on St_2 for different η. It is seen that the gains are always less than unity (except for the $\eta=1$ case) and exhibit a series of peaks and nodes. In particular, the nodes in the gain occur at frequencies satisfying $|\eta St_2 - St_2| = 2n\pi$, ($n$=0,1,2…). The gains for the η=0 and η=2 cases are identical, which is anticipated from the η dependence of the gain in Eq. (84). In the limit of $\eta\to1$, Eq. (83) can be reduced to $G_{\eta\to1} = e^{iSt_2}$, leading to a constant, unity gain irrespective of the value of St_2. As discussed above and also shown in Eq. (83), the above characteristics for the gain of the transfer function is a consequence of the superposition of the convective wrinkling and that locally induced by flow non-uniformity. Specifically, it is seen from Eq. (84) that the dependence of $|G|$ on η is symmetric about η=1, namely with the increase of η from 0, $|G|$ first increases and then decreases monotonically as η exceeds 1. Figure 32 shows the dependence of the phase of the transfer function on St_2 for different η. It is seen that the phase increases with increasing St_2 and has a jump of $-\pi$ at St_2 satisfying $|\eta St_2 - St_2| = 2n\pi$, as a result of the nodes in the gains at these values of St_2.

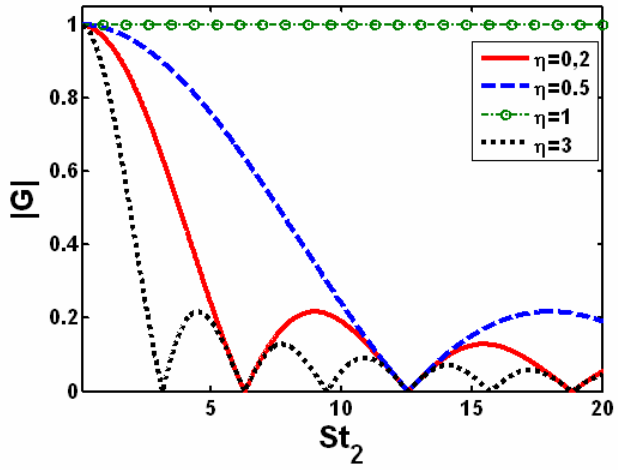

Figure 31 Strouhal number dependence of the magnitude of the wedge transfer function for different values of η, σ^*=0

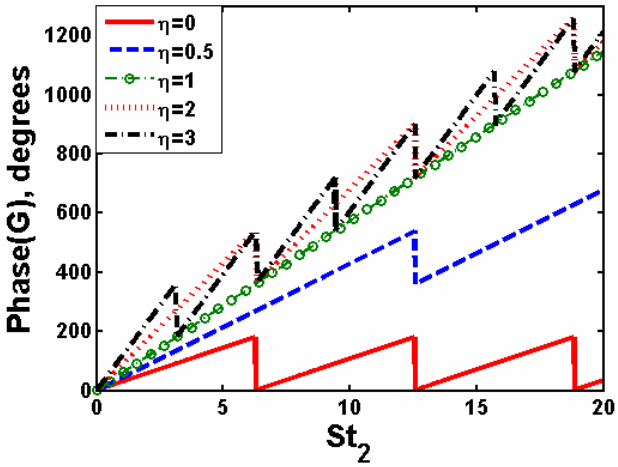

Figure 32 Strouhal number dependence of the phase of the transfer function for different values of η, σ^*=0

Note that in contrast to axisymmetric flames (see Chapter 4), two dimensional flames have nodes in the gain of the transfer function at $|\eta St_2 - St_2| = 2n\pi$. However, this does not mean that the flame does not respond to disturbances at these frequencies. To demonstrate this point, the radial distribution of the amplitude of the flame oscillation, $|\zeta_1|$, is shown in Figure 33 for St_2=47.5 and β=2 (σ_c^*=0 case only). It is seen that for this frequency there exist nodal points ($|\zeta_1|$=0) on the flame surface in additional to the one at

the flame base (r=1). Thus the flame segments within these nodal points are constrained by them and as such they oscillate in the manner of a vibrating string. Since there is no nodal point at the flame tip for this frequency, the flame segment between the flame tip and the nearest nodal point exhibits both bulk oscillatory movement and local wrinkling. Thus, the fluctuation of the flame surface area is a consequence of the superposition of these two forms of flame movement. Specifically, for frequencies corresponding to $\left|\eta St_2 - St_2\right| = 2n\pi$ ($St_2 = 2n\pi$ for η=0), a nodal point is located at the flame tip so that the entire flame surface is constrained by the nodal points and the fluctuation of the flame surface area is only due to flame wrinkling. In this case, it can be shown that the fluctuation amplitude of the flame surface area for the 2-D wedge flame is $O(\varepsilon^2)$, which is neglected by the linearization process. This is the reason that the transfer function shown in Figure 31 has nodes for $\left|\eta St_2 - St_2\right| = 2n\pi$ even though the velocity disturbance wrinkles the flame.

5.1.3 Stretch Effects under Uniform Velocity Disturbance

The influence of stretch on the gain and phase of the transfer function is considered in this section. To obtain insight into the results, it is useful to first consider the case of the uniform disturbance velocity field (η=0), which is simply an oscillating plug flow. For this case modification of the flame speed occurs only through the curvature of the flame front, as shown in Eq. (64). Then, the solution for the disturbed flame location, Eq. (74), becomes

$$\zeta_1 = -\frac{1}{iSt}\left[1 - e^{L_1(r-1)}\right] \tag{85}$$

Figure 33 shows the radial distribution of the amplitude of flame oscillation for different values of σ_c^*, with parameters (St_2=47.5 and β=2) chosen to be consistent with the experiments of Bourehla and Baillot [24]. It is seen that in the presence of stretch, the amplitude of the flame front wrinkling decays continuously from the flame base (r=1) to the tip (r=0), in contrast to the constant amplitude for the unstretched flame ($\sigma_c^* = 0$). Thus, the experimentally observed damping in the flame front oscillation away from the flame base is clearly reproduced, with this damping effect increasing with increasing σ_c^*.

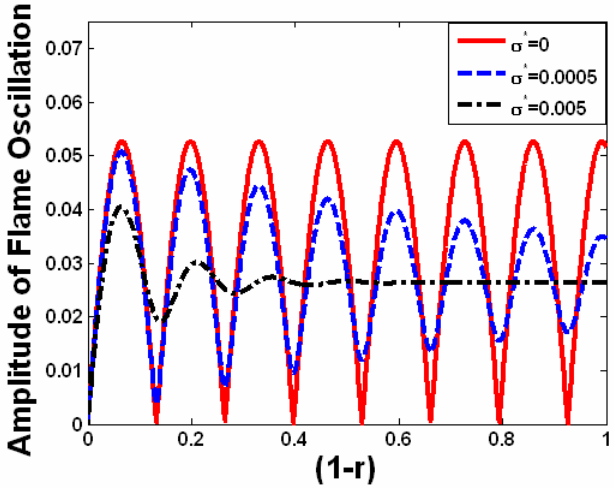

Figure 33 Radial distribution of the flame oscillation amplitude, $|\zeta_1(r)|$, for different values of σ_c^* with St_2 = 47.5, β=2 and η=0.

To further explore the damping mechanism of flame wrinkling by stretch, we expand Eq. (85) for small σ_c^*. In this limit,

$$L_1 \sim -iSt_2\left(1-2\sigma_c^{*2}St_2^2\right)+\sigma_c^* St_2^2$$

Then Eq. (85) becomes

$$\zeta_1 = -\frac{1}{iSt}\left[1 - e^{\sigma_c^* St_2^2 (r-1)} e^{-iSt_2\left(1-2\sigma_c^{*2} St_2^2\right)(r-1)}\right] \tag{86}$$

It is seen that for sufficiently small St_2, Eq. (86) degenerates to that for the unstretched flame

$$\zeta_{1,NS} = -\frac{1}{iSt}\left[1 - e^{-iSt_2(r-1)}\right] \tag{87}$$

implying that flame stretch effects are negligible such that the flame acts as an unstretched one under small disturbance frequencies. It is further seen from the comparison between Eqs. (86) and (87) that stretch damps the flame wrinkling through the term $e^{\sigma_c^* St_2^2 (r-1)}$, and this damping effect increases exponentially toward the flame tip, i.e. $r \to 0$. This demonstrates that the extent of damping in the flame wrinkling by stretch is controlled by the nondimensional parameter $\sigma_c^* St_2^2$, and becomes $O(1)$ as $\sigma_c^* St_2^2 \sim O(1)$, i.e. as the disturbance frequency satisfies $St_2 \sim O\left((\sigma_c^*)^{-1/2}\right)$. This property is consistent with the plots in Figure 33. For example, even for the very small stretch, $\sigma_c^* = 0.0005$, the damping is still quite evident especially near the flame tip (r=0) because $\sigma_c^* St_2^2 \approx 1.13 \sim O(1)$. For the case of $\sigma_c^* = 0.005$ for which $\sigma_c^* St_2^2 \approx 11.3$, the damping is so strong that the flame wrinkling is only evident near the flame base, consistent with the experiment of Bourehla and Baillot [24]. Furthermore, the nondimensional parameter $\sigma_c^* St_2^2$ indicates that the damping effect increases with the square of the disturbance frequency and hence is very sensitive to it. This is the reason that doubling the disturbance frequency is able to completely damp the flame wrinkling except for the flame base region, as shown in Figure 10. It is also seen from Eq. (86) and

Figure 33 that damping of the flame wrinkling results in more uniform flame oscillation amplitude, indicating an increase of the relative contribution of the bulk oscillatory movement of the flame to the fluctuation of the flame surface area. Moreover, Eq. (86) shows that flame stretch is also able to modulate the wavelength of the flame wrinkling through the term $1-\sigma_c^{*2}St_2^2$ in the exponential $e^{-iSt_2\left(1-2\sigma_c^{*2}St_2^2\right)(r-1)}$, and this modulation effect is $O(1)$ as $St_2 \sim \left(O(\sigma_c^*)^{-1}\right)$. However, at such a large St_2, flame wrinkling is totally suppressed such that its wavelength has no meaning. Thus, this effect can be neglected so that Eq. (37) can be further simplified to

$$\zeta_1 = -\frac{1}{iSt}\left[1-e^{\sigma_c^* St_2^2(r-1)}e^{-iSt_2(r-1)}\right]$$

and the expansion of L_1 only needs to keep the first two terms

$$L_1 \sim -iSt_2 + \sigma_c^* St_2^2 \tag{88}$$

It is noted that with the increase of St_2 to $O\left((\sigma_c^*)^{-1}\right)$, the expansion for L_1, Eq. (88), becomes less accurate. However, the trend revealed for the flame response at this order of frequency should still prevail.

We next study effects of flame stretch on the transfer function. Since the heat release rate mainly depends on the flame surface area, which in turn depends on the flame wrinkling, it is expected that flame stretch starts to have an $O(1)$ effect on the heat release and thereby on the transfer function for frequency St_2 from $O\left((\sigma_c^*)^{-1/2}\right)$. Substituting Eq. (85) into Eqs. (79) and (80), respectively, yields

$$G_S = -\frac{L_1 \sigma_c^*}{iSt_2}\left(1 - e^{-L_1}\right) \qquad (89)$$

$$G_A = -\frac{1}{iSt_2}\left(1 - e^{-L_1}\right) \qquad (90)$$

Figure 34 shows variations of the gains of G, G_A and G_S with the reduced Strouhal number, St_2, for $\sigma_c^* = 0.05$. The gain of the overall transfer function for the unstretched case ($\sigma_c^* = 0$),

$$G_{\sigma_c^*=0} = -\frac{1}{iSt_2}\left(1 - e^{iSt_2}\right) \qquad (91)$$

is also plotted for the purpose of comparison. It is seen that in the presence of flame stretch, the transfer function shows quite different behavior from the unstretched case. It is seen that the nodes at $St_2 = 2n\pi$ in the gain of the transfer function for the unstretched case ($\sigma_c^* = 0$) are eliminated in the presence of stretch, as already shown in Figure 33, leading to higher values of $|G|$ for the stretched flame around these frequencies. Relaxation of the flame surface from the nodal points then enhances fluctuation of the flame surface area, through the bulk oscillatory movement, to a larger extent than the damping effect through reduced wrinkling, which is O(ε^2) for $St_2 = 2n\pi$. Moreover, it is seen from the transfer functions for the stretched case that at small St_2 (<5) the overall transfer function G is very close to G_A, implying that contribution from the fluctuation of the flame surface area dominates that of the flame speed. However, with the increase of St_2 the relative contribution of G_S increases and finally becomes comparable to G_A at $St_2 \sim$ 30. It is noted that the gain of the overall transfer function, $|G|$, is not simply the sum of

$|G_A|$ and $|G_S|$ because G_A and G_S are not necessary in the same phase, as will be shown in Figure 35.

The dependence of the transfer functions, G_A, G_S and G, on the flame stretch σ_c^* and disturbance frequency St_2 can be further illustrated by substituting the expansion for L_1, Eq. (39), into Eqs. (40) and (41):

$$G_S \approx -\frac{1}{iSt_2}\left(-i\sigma_c^* St_2 + \sigma_c^{*2} St_2^2\right)\left(1 - e^{-\sigma_c^* St_2^2} e^{iSt_2}\right) \tag{92}$$

$$G_A \approx -\frac{1}{iSt_2}\left(1 - e^{-\sigma_c^* St_2^2} e^{iSt_2}\right) \tag{93}$$

Comparing Eq. (93) with the transfer function for the unstretched flame, Eq. (91), shows that flame stretch starts to have an $O(1)$ effect on the transfer function as the disturbance frequency St_2 satisfies $\sigma_c^* St_2^2 \sim O(1)$, as noted earlier. At this frequency, $G_S/G_A \sim O\left((\sigma_c^*)^{1/2}\right)$, and hence the contribution from the flame speed fluctuation can be neglected. Thus, the overall transfer function G is mostly derived from fluctuations of the flame surface area and the effect of flame stretch is only through its modulation of the flame shape. Therefore, we have

$$G \approx G_A \approx -\frac{1}{iSt_2}\left(1 - e^{-\sigma_c^* St_2^2} e^{iSt_2}\right) \sim O\left((\sigma_c^*)^{1/2}\right) \tag{94}$$

With St_2 increasing from $O\left((\sigma_c^*)^{-1/2}\right)$ to $O\left((\sigma_c^*)^{-1}\right)$, the contribution from the flame speed fluctuation, G_S, becomes comparable to G_A. Furthermore, since flame wrinkling is totally suppressed at this order of St_2, fluctuations of the flame surface area are mainly due to the bulk movement of the flame. Then the transfer functions become

$$G_S \approx -\frac{1}{iSt_2}\left(-i\sigma_c^* St_2 + \sigma_c^{*2} St_2^2\right), \quad G_A \approx -\frac{1}{iSt_2} \tag{95}$$

and the overall transfer function is given by

$$G \approx -\frac{1}{iSt_2}\left(1 + \sigma_c^{*2} St_2^2 - i\sigma_c^* St_2\right) \sim O\left(\sigma_c^*\right) \tag{96}$$

The above characteristics are consistent with Figure 34, which shows that G and G_A have almost identical values for $St_2 < 5$ ($\sigma_c^* St_2^2 \sim O(1)$), while G_A and G_S contribute comparably to the overall transfer function G for St_2>20 ($\sigma_c^* St_2 \sim O(1)$).

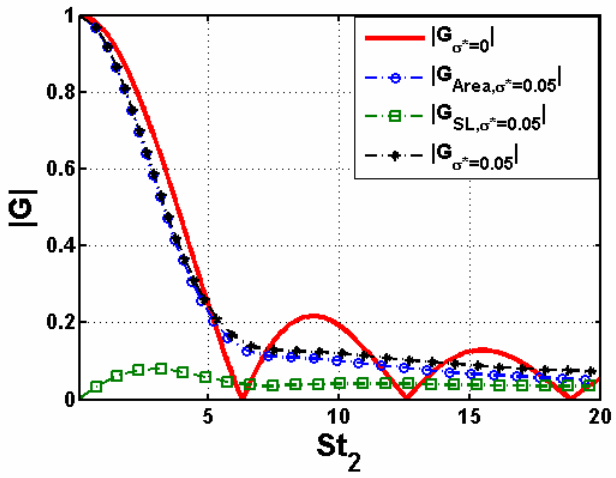

Figure 34 Variations of the gains of the overall transfer function G and the transfer functions resulted from the fluctuations of flame surface area and flame speed, G_A and G_S, with St_2 for $\sigma_c^* = 0.05$ and $\eta = 0$.The gain of the overall transfer function for $\sigma_c^* = 0$ and $\eta = 0$ is also plotted for comparison.

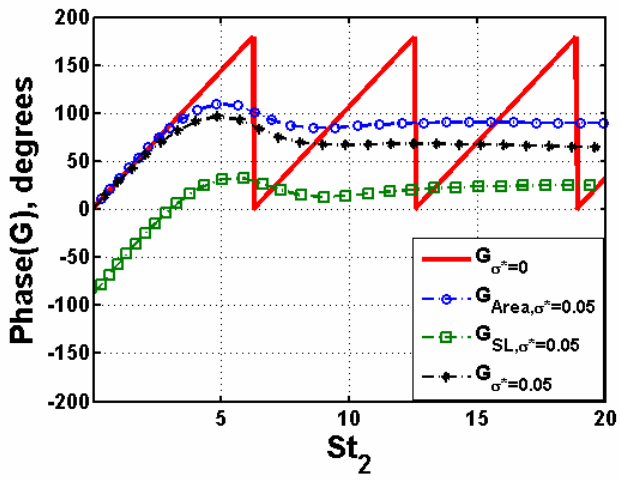

Figure 35. Variations of the phase of the overall transfer function *G* and the transfer functions resulted from the fluctuations of flame surface area and flame speed, G_A and G_S, with St_2 for $\sigma_c^* = 0.05$ and $\eta = 0$.

Figure 35 shows variations of the phases of G, G_A and G_S with the reduced Strouhal number, St_2, for $\sigma_c^* = 0.05$. It is seen that, compared to the unstretched case, the $-\pi$ jump in the phase resulted from the nodes in the gain of the transfer function is smoothed out, due to elimination of these nodes in the presence of stretch. Furthermore, it is seen that at small St_2, the phase of G follows closely that of G_A, whereas with increasing St_2 it approaches the phase of G_S due to the increased relative contribution of G_S, which is the same trend as we have discussed for the gain of the transfer function in Figure 34

5.1.4 Stretch Effects under Nonuniform Velocity Disturbance

In the more general case of a nonuniform disturbance velocity field ($\eta \neq 0$), the flame speed is modified by both the curvature and aerodynamic strain, as shown in

Eq.(78). In addition, the baseline flame response is also changed due to the wrinkling locally induced by the flow non-uniformity.

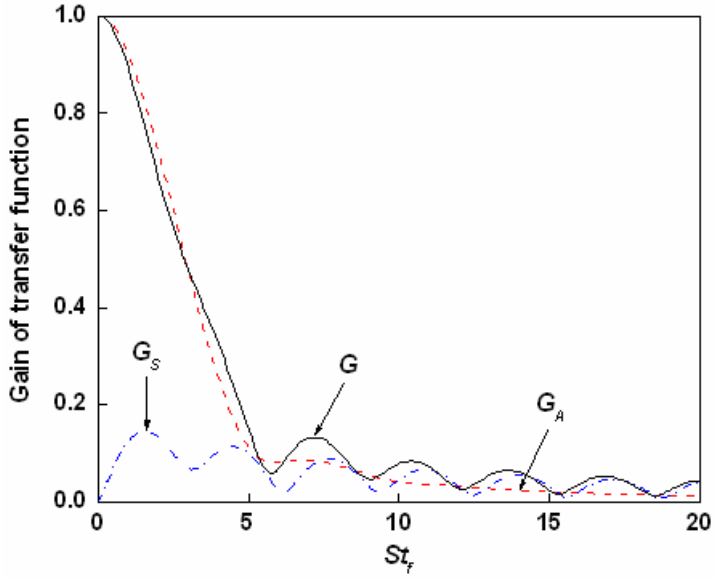

Figure 36 Variations of the gains of the overall transfer function *G* and the transfer functions resulted from the fluctuations of flame surface area and flame speed, G_A and G_S, with St_2 for $\sigma_c^* = 0.05$, $\sigma_s^* = 0$ and $\eta = 2$.

Substituting Eq. (74) into Eqs. (79) and (80) yields the transfer functions under nonuniform disturbance,

$$G_S = -\frac{\sigma_c^* C_1}{iSt_2}\left[L_1\left(1-e^{-L_1}\right)+iSt_2\eta\left(1-e^{iSt_2\eta}\right)\right]-\sigma_s^*\left(1-e^{iSt_2\eta}\right) \tag{97}$$

$$G_A = -\frac{C_1}{iSt_2}\left(-e^{-L_1}+e^{iSt_2\eta}\right) \tag{98}$$

where

$$C_1 = \frac{1-i\sigma_s^* St_2\eta}{i\sigma_c^* St_2\eta^2-\eta+1}$$

Figure 36 shows variations of the gains of G, G_A and G_S with the reduced Strouhal number, St_2, for $\sigma_c^* = 0.05$, $\sigma_s^* = 0$ and η=2. It is seen that at small frequencies ($St_2 < 5$) the overall transfer function G can be approximately represented by G_A, whereas at large St_2, G follows closely the trend of G_S, indicating that contributions from fluctuations of the flame surface area and flame speed dominate at small and large frequencies, respectively. To further analyze the trend shown in Figure 36, we substitute the expansion for L_1, and obtain

$$\zeta_1 \approx -\frac{C_1}{iSt}\left(-e^{-\sigma_c^* St_2^2(1-r)}e^{iSt_2(1-r)} + e^{iSt_2\eta(1-r)}\right) \tag{99}$$

$$G_S = -\frac{C_1}{iSt_2}\left[\left(-i\sigma_c^* St_2 + \sigma_c^{*2} St_2^2\right)\left(1 - e^{-\sigma_c^* St_2}e^{i\sigma_c^* St_2}\right) + i\sigma_c^* St_2\eta\left(1 - e^{iSt_2\eta}\right)\right] - \sigma_s^*\left(1 - e^{iSt_2\eta}\right) \tag{100}$$

$$G_A = -\frac{C_1}{iSt_2}\left(-e^{-\sigma_c^* St_2}e^{i\sigma_c^* St_2} + e^{iSt_2\eta}\right) \tag{101}$$

Comparing Eq. (101) with the transfer function for the unstretched flame, Eq. (83), shows that flame stretch begins to have $O(1)$ effects on the transfer function G_A as the disturbance frequency satisfies $\sigma_c^* St_2^2 \sim O(1)$, as in the case of the uniform velocity disturbance. At this frequency, $G_S / G_A \sim O\left((\sigma_c^*)^{1/2}\right)$, and hence the contribution from G_S can be neglected in the overall transfer function. Thus, the overall transfer function G is mostly derived from fluctuations of the flame surface area:

$$G \approx G_A \approx -\frac{C_1}{iSt_2}\left(-e^{-\sigma_c^* St_2}e^{i\sigma_c^* St_2} + e^{iSt_2\eta}\right) \tag{102}$$

Furthermore, as discussed in Section 5.1.2, under nonuniform velocity disturbance the solution is determined by the superposition of the convective wrinkling and that locally

induced by flow non-uniformity. It is apparent from the comparison between the results obtained with and without stretch effects, Eqs (33) and (50) and Eqs. (34) and (53), that flame stretch only damps the convective wrinkling with the locally induced wrinkling remains unchanged.

As St_2 increases from $O\left((\sigma_c^*)^{-1/2}\right)$ to $O\left((\sigma_c^*)^{-1}\right)$ such that $\sigma_c^* St_2 \sim O(1)$, the contribution from the flame speed fluctuation, G_S, becomes comparable to that from G_A. Furthermore, it is seen from Eq. (100) that aerodynamic strain only operates through the flame speed fluctuation. Further note that since both σ_c^* and σ_s^* are determined by the nondimensional flame thermal thickness (see Eqs. (65) and (73)) and we have assumed $Ze\left(Le^{-1}-1\right) \sim O(1)$, σ_c^* and σ_s^* can be assumed to have the same order of magnitude. Thus, at $St_2 \sim O\left((\sigma_c^*)^{-1}\right)$, aerodynamic strain contributes to G_S comparably with the rest of the terms of G_S. At this order of St_2, contributions to G_A and G_S due to the convective wrinkling have been totally damped such that the transfer functions become

$$G_S = -\frac{C_1}{iSt_2}\left[\left(-i\sigma_c^* St_2 + \sigma_c^{*2} St_2^2\right) + i\sigma_c^* St_2 \eta\left(1-e^{iSt_2\eta}\right)\right] - \sigma_s^*\left(1-e^{iSt_2\eta}\right) \qquad (103)$$

$$G_A = -\frac{C_1 e^{iSt_2\eta}}{iSt_2} \qquad (104)$$

With further increase of St_2, G_S becomes dominant over G_A and G follows closely the trend of G_S at large St_2, consistent with Figure 36

Figure 37 shows variations of the phases of G, G_A and G_S with St_2, for $\sigma_c^* = 0.05$, $\sigma_s^* = 0$ and η=2. It is seen that, as in the case of uniform velocity disturbance shown in

Figure 35, the phase jump of $-\pi$ is moderated by stretch and the phase of G follows the trends of G_A and G_S at small and large St_2, respectively. The difference is that for this value of η (=2), all the phases have close values.

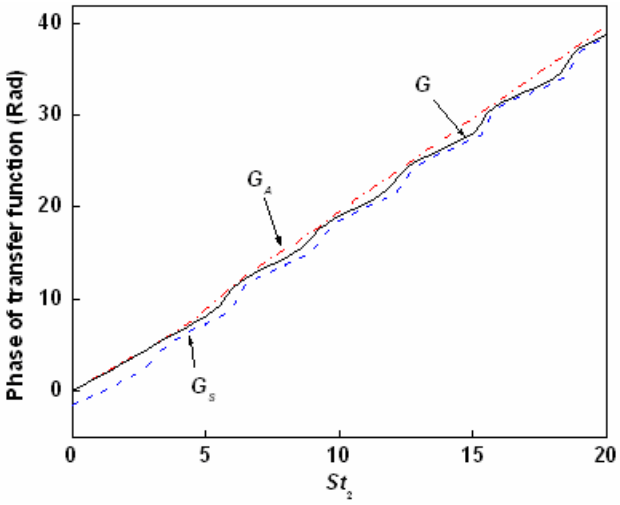

Figure 37 Variations of the phases of the overall transfer function G and the transfer functions resulted from the fluctuations of flame surface area and flame speed, G_A and G_S, with St_2 for $\sigma_c^* = 0.05$, $\sigma_S^* = 0$ and $\eta = 2$.

Figure 38 and Figure 39 respectively show variations of the gain and phase of the overall transfer function with St_2 for different values of η, with $\sigma_c^* = 0.02$ and $\sigma_S^* = 0.02$. Again the nodes in the gain and the $-\pi$ jump in the phase of the transfer function at $|\eta St_2 - St_2| = 2n\pi$ are eliminated by stretch. In addition, in contrast to the constant gain of unity for the unstretched η =1 case shown in Figure 31, stretch effects cause the gain to reduce monotonically with increasing St_2. Also, note that the gains for the η =0 and η =2 cases are identical in the unstretched case. However, in the presence of stretch, they possess different values. As we have discussed, the special characteristics for the gain of the transfer function for the unstretched case, such as unity gain for η=1 and the same

gains for η=0 and 2, is a consequence of the superposition of the convective and locally induced wrinkling. Therefore, for these values of η, damping of the convective wrinkling leads to substantially different behavior in the presence of stretch.

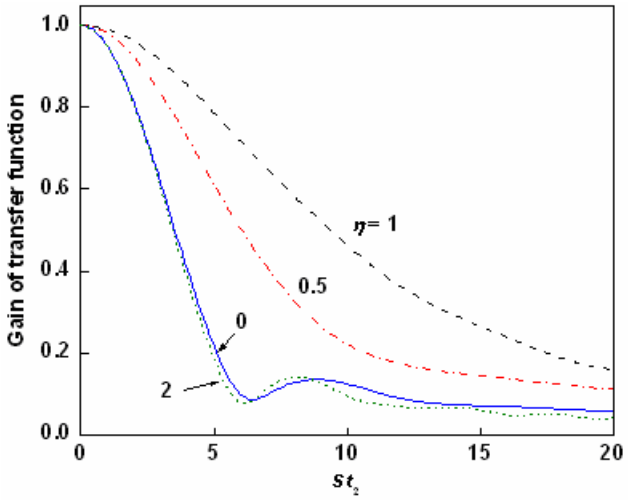

Figure 38 Variations of the gain of the overall transfer function *G* with St_2 for $\sigma_C^* = 0.02$, $\sigma_S^* = 0.02$ and different values of η.

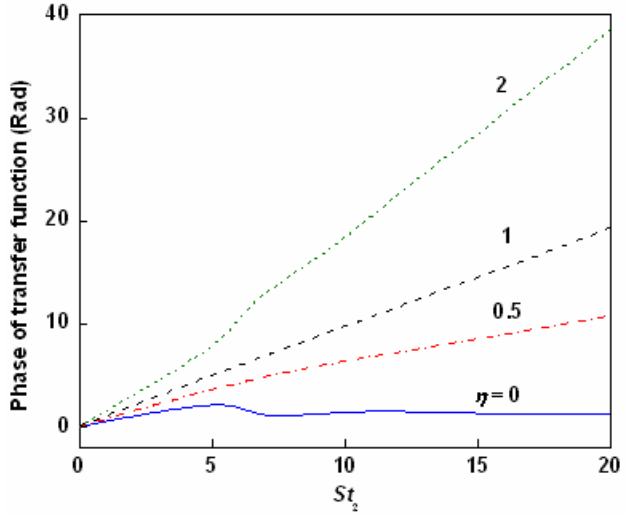

Figure 39 Variations of the phase of the overall transfer function *G* with St_2 for $\sigma_C^* = 0.02$, $\sigma_S^* = 0.02$ and different values of η.

5.1.5 Stretch Effects in Other Flame Geometries

In this chapter, a 2D wedge flame has been considered for analysis. For the 2D conical flame, since the leading-order flame location ζ_o is not analytically solvable due to the flame curvature effect at the flame tip, the evolution equations for both ζ_o and ζ_1 are second-order nonlinear ordinary differential equations and hence have to be solved numerically. However, in the limit of weak stretch, Eq. (63) is in fact a very good approximation for ζ_o except for the $O(\delta)$ region around the flame tip. Since the quantities of practical interest are the integrated ones over the entire flame surface, such as the heat release rate and the transfer function, the error induced by using Eq. (63) to approximate ζ_o for the 2D conical flame is expected to be small. The analysis for the wedge flame then becomes fundamentally applicable to the 2D conical flame, with the boundary condition in Eq. (23) replaced by that of symmetry.

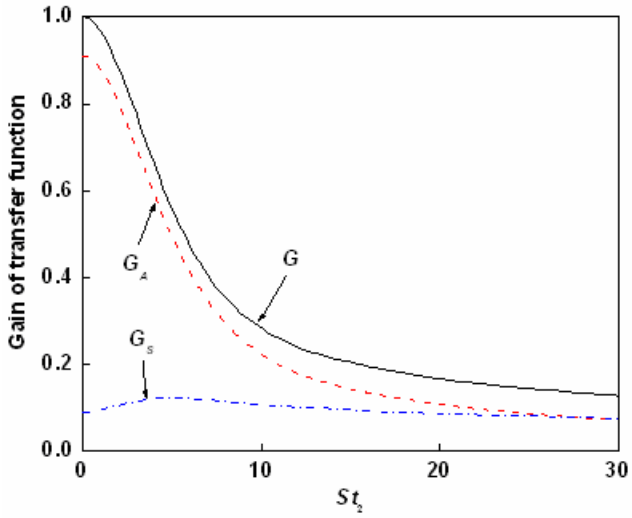

Figure 40 Variations of the gains of the overall transfer function G and the transfer functions resulted from the fluctuations of flame surface area and flame speed, G_A and G_S, with St_2 for the axisymmetric conical flame, with $\sigma_c^* = 0.05$, $\sigma_s^* = 0$ and $\eta = 0$.

For axisymmetric geometries (wedge and conical), the expression for the stretch-affected flame speed has an additional azimuthal term that introduces additional analytical complexity (see Appendix G for results). However, the qualitative trends for the effects of flame stretch on the linear flame response deduced from the 2D geometries still apply to the axisymmetric ones. Figure 40 shows variations of the gains of G, G_A and G_S with St_2 for the axisymmetric flame. It is seen that they exhibit the same trend as that of Figure 34, namely the contribution to the transfer function from the fluctuation of the flame surface area G_A dominates at small St_2, while with increasing St_2 the contribution from the flame speed fluctuation G_S increases and becomes comparable to G_A at $St_2 \sim \left(\sigma_c^*\right)^{-1}$. However, the effect of flame geometry causes the response of the overall heat release to exhibit significant quantitative differences. These differences are due to the fact that unsteady curvature effects grow in prominence with downstream distance. Thus, for an axisymmetric wedge flame where the majority of the flame area is at its tip, curvature effects cause substantial reductions in flame response, relative to those for the 2-D case (where flame area is distributed equally along the whole flame length). In contrast, for a conical flame, the majority of flame area lies at the flame base, where curvature effects are not as significant. Thus, curvature effects have a significant impact on the area fluctuations (G_{Area}) of these flames at much higher frequencies than axisymmetric wedge flames.

5.2 Remarks

In this chapter an analytical investigation of the linear response of a 2D wedge-shaped premixed flame to harmonic velocity disturbances is presented, which allows for the

dependence of the flame speed on stretch. Different from previous studies, the transfer function now consists of contributions from fluctuations of both the flame surface area and flame speed. Two nondimensional parameters, $\sigma_c^* St_2^2$ and $\sigma_c^* St_2$, were identified to characterize their relative contributions and thereby the impact of flame stretch on the flame response. Specifically, as the disturbance frequency satisfies $\sigma_c^* St_2^2 \sim O(1)$, i.e. $St_2 \sim O\left((\sigma_c^*)^{-1/2}\right)$, flame stretch starts to have $O(1)$ effect on the transfer function through damping of the disturbance-induced flame wrinkling. At this order of the frequency, the contribution from the flame speed fluctuation is negligibly small. Thus flame stretch affects the transfer function only through its modulation of the flame shape and thereby its surface area and this effect increases with the square of the disturbance frequency. At larger frequencies such that $\sigma_c^* St_2 \sim O(1)$, i.e. $St_2 \sim O\left((\sigma_c^*)^{-1}\right)$, contributions from fluctuations of the flame surface area and flame speed become comparable.

Flame stretch was commonly believed to be not important in the response of flames to disturbances, except for very large disturbance frequencies at which the wavelength of the disturbance-induced flame wrinkling is small so that the flame front curvature is sufficiently large. At such a large frequency the flame response diminishes significantly because flames tend not to respond to high frequency disturbances. However, the present study has convincingly demonstrated that, even for small σ_c^*, flame stretch is still important for "moderate" disturbance frequencies. This is because even if σ_c^* is small, $St_2 \sim \left(\sigma_c^*\right)^{-1/2}$ could assume values that are not very large but

nevertheless would induce $O(1)$ effects on the flame response, for example through damping of the disturbance-induced flame wrinkling. For example, this implies that stretch effects become important for $f > 100$ Hz for a methane-air flame with equivalence ratio of 1.0, $M_l \approx 1$ mm, flame length $L_f \approx 50$ mm and $u_o = 2$ m/s

CHAPTER 6

NUMERICAL FORMULATION

In this chapter, details of the coupled Euler-*G* equation solver are presented. Specifically, the numerical algorithms for each of the modules and their implementation details are discussed. The mathematical formulation and the basic principle behind the Ghost Fluid Method (GFM), used for applying the jump conditions across the flame, is elucidated. Finally, the chapter ends with a discussion about the test cases used for validating the code.

6.1 Governing Equation

The governing equations for three-dimensional, unsteady, inviscid compressible flows are given by:

$$\begin{pmatrix} \rho \\ \rho u \\ \rho v \\ \rho w \\ E \end{pmatrix}_t + \begin{pmatrix} \rho u \\ \rho u^2 + p \\ \rho uv \\ \rho uw \\ (E+p)u \end{pmatrix}_x + \begin{pmatrix} \rho v \\ \rho uv \\ \rho v^2 + p \\ \rho vw \\ (E+p)v \end{pmatrix}_y + \begin{pmatrix} \rho w \\ \rho uw \\ \rho vw \\ \rho w^2 + p \\ (E+p)w \end{pmatrix}_z = 0 \qquad (105)$$

where t is the time, ρ is the density, (u,v,w) are the velocities in the (x,y,z) dimensions, E is the total energy per unit volume and p is the pressure. The total energy, which is the sum of the kinetic energy and the internal energy, can be expressed as:

$$E = \rho e + \rho \frac{u^2 + v^2 + w^2}{2} \qquad (106)$$

where e is the internal energy per unit mass. Assuming ideal gas, the following relations hold:

$$p = \rho RT \qquad (107)$$

$$e = e_o + C_v T \quad (108)$$

where T is the temperature, R is the specific gas constant, C_v is the specific heat at constant volume and e_o is a constant corresponding to the formation energy at 0 K (chosen to be consistent with the heat release across the flame).

Consistent with the hydrodynamic theory, the flame is treated as a surface of discontinuity between the burned and unburned gases. Each of the fluids, i.e. reactants and products, satisfy the Euler equations (105)-(108) separately. The matching conditions (i.e. Rankine-Hugoniot relationship) at the flame are given by:

$$\begin{aligned}
&\left[\rho\vec{N}\bullet\left(\vec{V}-\vec{V}_f\right)\right]=0\\
&\left[p+\rho\left(\vec{N}\bullet\left(\vec{V}-\vec{V}_f\right)\right)^2\right]=0\\
&\left[\vec{V}\times\vec{N}\right]=0\\
&\left[e+\frac{p}{\rho}+\frac{\left(\vec{V}-\vec{V}_f\right)\bullet\left(\vec{V}-\vec{V}_f\right)}{2}\right]=0
\end{aligned} \qquad (109)$$

where $[\bullet]$ denotes the difference between the values on the product and reactant side, $\vec{V}_f$ is the local velocity of the flame front and $\vec{N}$ is the local unit normal to the flame.

The flame location, where the jump conditions (see Eq. (109)) have to be applied, is tracked using the level set method. The instantaneous flame position is given by an implicit expression, $G(x,t)=0$, where $G(\vec{x},t)$ is governed by the following equation:

$$\frac{\partial G}{\partial t}+\vec{V}_f\bullet\nabla G=0 \qquad (110)$$

Note that G is uniquely defined only at the flame surface while the surrounding G field is not. In the present implementation, G is initialized to be a signed distance function from

the flame (i.e. $\left(|\nabla G| = 1\right)$) which is advected using Eq. (110). Under the evolution of Eq. (110), $G(\vec{x},t)$ may not remain a distance function and hence reinitialization is required. This is done using [71]:

$$\frac{\partial G}{\partial \tau} + S(G_o)\left(|\nabla G| - 1\right) = 0 \qquad (111)$$

where $S(G_o)$ is the sign of G_o and τ is an artificial time. Here $G_o(\vec{x},t)$ refers to the level set function which is not a distance function while $G(\vec{x},t)$ is the new level set constructed which is a distance function *and has the same zero level set of* $G(\vec{x},t)$. Mathematically, Eq. (111) ensures that the G field will always be a distance function while the flame location remains unaffected by the reinitialization procedure (since $S(G_o)$ is zero at the flame).

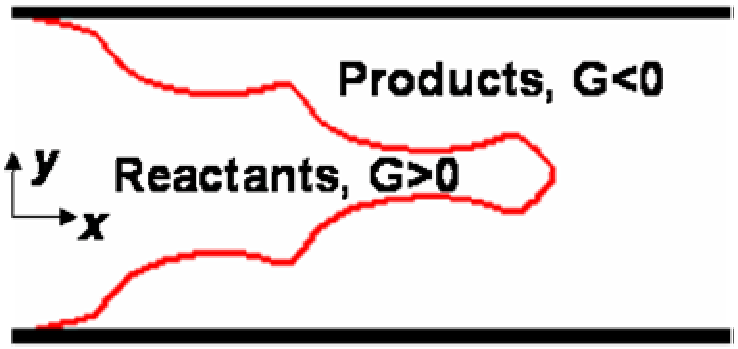

Figure 41. Illustration of two-dimensional flame geometry

In the current investigation, an inverted V flame in a two dimensional channel is considered (see Figure 41). The flame is assumed to be anchored on a ring attached to the inlet (x=0). Mathematically, this condition can be expressed as:

$$\left.\frac{\partial G}{\partial t}\right|_{x=0} = 0 \qquad (112)$$

At the inlet (x=0), the flow is assumed to be spatially uniform (in y direction) with an oscillating time component, i.e.,

$$\begin{aligned} u(x=0,y,t) &= \bar{u} + u' \, Cos(\omega t) \\ v(x=0,y,t) &= 0 \end{aligned} \qquad (113)$$

where ω is the frequency of forcing and u' is the amplitude of oscillation (uniform in y direction). Also, the inlet temperature, T_o, is imposed to be a constant (see Section 6.2.4). Wall boundary conditions are applied on the sides of the channel (see Figure 41) and non-reflecting boundary conditions at the exit. (105)-(113) form the complete set of governing equations which are solved numerically in order to capture the interaction between the flame and the flow.

6.2 Numerical Approach

The flame is treated as an interface separating two fluids i.e., products and reactants. The zero level marks the location of the flame, while G>0 and G<0 corresponds to reactants and products respectively. Note that both the fluids satisfy the Euler equations and their corresponding equation of state. Following the approach of Fedkiw *et al.*[59], the discretization of the level set can be done independent of the two sets of Euler equations. The details of the numerical scheme, for solving Eq.(110), are presented in Section 6.2.2.

Following Fedkiw *et al*. [60,61], the Ghost Fluid Method (GFM) is used to apply the matching conditions (Eq (109)) at the flame location. Essentially, any point in the computational domain can be determined to be either the reactant (G>0) or the product (G<0) based on the value of the level set function (G). Close to the flame (G=0), a band of ghost cells are defined. Each point in this band of cells, stores the mass, momentum

and energy of the real fluid that exists at that point (i.e. product or reactant depending on the value of G) and a *ghost mass, momentum and energy for the other fluid (which does not really exist at that point)*. Once the ghost fluid cells are defined (see Section 6.2.3 for details), numerical methods applicable to the single phase Euler solver (see Section 6.2.1) are used to discretize Eq (105) for each of the fluids separately. Then the level set function is advanced in time and the new value of G is used to decide which of the two discretizations should be used at a given grid point. The *ghost* cells are updated after very substep in the Runge-Kutta time integration routine while the G field is updated after the full Runge-Kutta time step.

In some other studies related to flame propagation [62,63], the level set is used to define a sharp interface (flame) location but smear out the flow variables (i.e. density, velocity etc). This approach is not acceptable as the flame propagation speed is dependent on the exact unburnt fluid conditions, which is lost when the flow variables are smeared out. Smiljanovski *et al*. [73] and more recently Schmidt & Klein [64], have developed a "in-cell reconstruction technique" which allows a sharp flame interface without any smearing of the flow variables. However, the Rankine-Hugoniot jump conditions have to be *explicitly* enforced at the flame which adds to algorithm complexity and computational cost (especially in multi-dimensions). In contrast, GFM *implicitly* captures the jump conditions at the flame by using *ghost* cells. Another advantage of GFM is that any single phase multidimensional solver can be used, without any modification, for solving multiphase problems. The entire complexity of applying the jump conditions is reduced to choosing the ghost /real fluid value at every point appropriately (which results in the

jump conditions across the flame being satisfied) and this aspect is handled by a separate GFM module.

In essence, there are three specific modules in the present formulation: An Euler solver, which is used to discretize the governing equations ((105)-(108)) for the two fluids (products and reactants), a GFM module which populates the ghost cells in a thin band around the flame and a *G*-equation module which tracks the flame dynamics. The numerical aspects of each of these modules and the boundary conditions are discussed in the following sub-sections.

6.2.1 Euler Solver

An unsteady, compressible, two dimensional finite difference Euler solver has been developed as part of the current investigation. A fifth order WENO (weighted essentially non-oscillatory) scheme developed by Jiang and Shu [65] has been implemented to evaluate the spatial discretizations in Eqs (105)-(108). These schemes (i.e. WENO) are based on ENO (essentially non-oscillatory) schemes which were first developed by Harten *et al* [66]. The essential idea behind ENO schemes is to use the "smoothest" stencil among several candidates to approximate the fluxes to a high order of accuracy and also avoid oscillations near discontinuities (say shocks). ENO schemes are uniformly higher order accurate right up to the discontinuity and have been found to be very robust. However, this free adaptation of the stencils is not necessary in the smooth regions of the flow. Also, ENO schemes involve a lot of decision making in the stencil choosing step which adds to the computational cost. WENO schemes overcome these drawbacks and still have the same robustness and high accuracy of ENO schemes. Essentially, a convex combination of all the stencils is used for calculating the fluxes in

contrast to using only a single stencil as in ENO. Each of the candidate stencils is assigned a weight which determines its contribution to the final approximation of the numerical flux. These weights are chosen so that they achieve higher order accuracy in smooth regions and are assigned a weight of zero if they contain a discontinuity (so they reduce to ENO at the discontinuities). Also, WENO schemes completely remove the logical decision making involved in choosing the stencils [65]. Hence these schemes are faster than ENO and have been found to be successful in a variety of applications, especially for problems containing both shocks and complicated smooth solution structures such as compressible turbulence [67,68].

For further discussion, the system of equations in (105) is rewritten in vector form (for the two dimensional case as):

$$\frac{\partial s}{\partial t}+\frac{\partial f(s)}{\partial x}+\frac{\partial g(s)}{\partial y}=0 \quad (114)$$

where $f(s)$ and $g(s)$ are the fluxes. $\frac{\partial f(s)}{\partial x}$ can be approximated (in conservative form) as:

$$\frac{\partial f(s)}{\partial x}=\frac{\left(\hat{f}_{i+1/2}-\hat{f}_{i-1/2}\right)}{\Delta x} \quad (115)$$

where $\hat{f}$ is the numerical flux to be evaluated. In the current algorithm, the following procedure is adopted [65] to evaluate the numerical flux:

a) Divided differences of the flux $f(s)$ and the solution s is stored at all grid points in the x direction, i.

b) At each fixed $x_{i+1/2,}$ the right eigenvectors (R_v), left eigenvectors (L_v) and the eigenvalues (λ_v) of the Jacobian $f'\left(s_{i+1/2}\right)$ (where $s_{i+1/2}$ is defined to be the average state at $x_{i+1/2}$) [69] are computed.

c) The differences computed in (a) are transformed into local characteristic fields using L_v , i.e.

$$S = L_v s$$
$$F = L_v f(s)$$

d) Global Lax-Friedrichs flux splitting operation is performed on each component of the characteristic variable and the WENO reconstruction procedure is applied to the positive and negative fluxes to get $\hat{F}^{\pm}_{i+1/2}$

e) Then, R_v is used transform back into physical space, i.e.,

$$\hat{f}^{\pm}_{i+1/2} = R_v \hat{F}^{\pm}_{i+1/2}$$

f) The numerical flux $\hat{f}_{i+1/2}$ is evaluated by adding the positive and negative fluxes

g) The derivative is computed using Eq (115).

h) Steps (a)-(g) are applied to compute the derivative in the y direction

For the time discretization, Runge-Kutta method is used to solve a system of initial value ODE's (resulting from the method of lines spatial approximation to the PDE). In the current implementation, a TVD (total variation diminishing) Runge-Kutta method [65] is used to achieve third order accuracy in time. The time step is decided by the CFL criterion:

$$\Delta t = CFL * min\left(\frac{\Delta x}{|u+c|}, \frac{\Delta y}{|v+c|}\right) \qquad (116)$$

where c is the local speed of sound and the *min* operation is performed over the entire computational domain.

6.2.2 G-equation Solver

The level set equation used for tracking the flame, Eq. (110), is a Hamilton–Jacobi equation. This equation is non-conservative and has the property that the solution develops sharp corners and cusps (discontinuities in derivative) even with a smooth initial condition. Hence robust numerical schemes that can capture these effects without excessive smearing are required. In the current solver (see Santosh *et al.* [70]), a fifth-order WENO [55] discretization of the spatial derivatives and a third-order TVD Runge–Kutta method [56] for the time integration has been implemented. To approximate the advection and propagation terms, the numerical Godunov Hamiltonian was adopted as it minimizes numerical dissipation errors. The solution domain is discretized using a uniform grid.

The initial value for the G-field was constructed from the assumed quiescent flame shape. This was done by defining the value of G at each grid location to be the signed distance of that location from the quiescent flame surface. The G-field was reset to a distance function after each time step using the reinitialization procedure described by Peng *et al*. [71].

In order to reduce the computational time, Eq. (110) is solved only in a band around the flame. This was achieved [70] by adopting the localization procedure introduced by Peng *et al*. [71]. Equation (110) is solved within a narrow band of grid points around the instantaneous flame front. This band evolves in time as the flame moves or as pockets form and burnout. This solver has been found to be very efficient and robust in implicitly capturing the formation of corners and pockets in a turbulent flame [70].

The instantaneous heat release of the (two dimensional) flame surface is given by:

$$Q(t) = \int_S \rho_u S_L \Delta h_R \, \delta(G) |\nabla G| \, d\Omega$$

where the integration is performed over a band of grid points around the flame and $\delta(G)$ is the Dirac-delta function. This integral is then evaluated at every sampling time step, using the numerical technique described in Smereka [72].

6.2.3 Ghost Fluid Method

In this section, the implementation of GFM is presented in detail. This discussion closely follows the work of Fedkiw *et al.* [61]. Consider the case wherein positive values of G denote reactants and negative values denote products. Then, the normal, defined as:

$$\vec{N} = \frac{\nabla G}{|\nabla G|} \qquad (117)$$

points from products into reactants. Let D denote the velocity of the flame front in the normal direction. The key idea behind GFM is that (in a reference frame moving with the flame) the mass (F_ρ), momentum ($F_{\rho VN}$) and energy flux (F_E) in a direction normal to the flame is conserved. This is equivalent to the Rankine-Hugoniot jump conditions at the flame moving with a speed D in the normal direction. So, in contrast to explicitly applying the Rankine-Hugoniot jump conditions at the interface [73], GFM uses the fact that F_ρ, $F_{\rho VN}$, and F_E are continuous to define a *ghost* fluid that captures the interface values of these variables.

Following [61], the expressions for the fluxes (in a reference frame moving with the flame) can be written as:

$$
\begin{aligned}
F_\rho &= \rho\left(V_N - D\right) \\
F_{\rho VN} &= p + \rho\left(V_N - D\right)^2 \\
F_E &= \left(\rho e + \frac{\rho\left(V_N - D\right)^2}{2} + \frac{\rho\left(V_{T1}^2 + V_{T2}^2\right)}{2} + p \right)\left(V_N - D\right)
\end{aligned}
\tag{118}
$$

where V_N refers to the normal component of the velocity while $V_{T1,2}$ refers to the tangential components of the velocity. At the interface:

$$
\begin{aligned}
F_\rho^{gt} &= F_\rho^{rl} \\
F_{\rho VN}^{gt} &= F_{\rho VN}^{rl} \\
F_E^{gt} &= F_E^{rl}
\end{aligned}
\tag{119}
$$

where the superscripts *gt* and *rl* stand for ghost fluid and real fluid respectively. Note that at any grid point, all quantities with the subscript *rl* are known. So the set of equations in (118) –(119) can be solved to yield:

$$
\begin{aligned}
V_N^{gt} - D &= \frac{\gamma^{gt} F_{\rho VN}^{rl}}{\left(\gamma^{gt}+1\right)F_\rho^{rl}} \pm \sqrt{\left(\frac{\gamma^{gt} F_{\rho VN}^{rl}}{\left(\gamma^{gt}+1\right)F_\rho^{rl}}\right)^2 - \frac{2\left(\gamma^{gt}-1\right)}{\left(\gamma^{gt}+1\right)}\left(\frac{\hat{F}_E^{rl}}{F_\rho^{rl}} - e_o^{gt}\right)} \\
\hat{F}_E &= \left(\rho e + \frac{\rho\left(V_N - D\right)^2}{2} + p \right)\left(V_N - D\right)
\end{aligned}
\tag{120}
$$

Eq (120) can be used to calculate the normal velocity of the ghost fluid. The ± sign in Eq (120) is chosen to give the minimum value of $\left|V_N^{gt} - D\right|$. Then the set of equations in (118) –(119) can be used to determine ρ^{gt}, p^{gt} and e^{gt}. Since the tangential velocities are continuous across the flame, the velocity in the ghost fluid is obtained by combining the normal velocity of the ghost fluid with the tangential velocity of the real fluid, i.e.,

$$
\vec{V}^{gt} = V_N^{gt}\vec{N} + \vec{V}^{rl} - V_N^{rl}\vec{N} \tag{121}
$$

Note that the tangential directions are never explicitly used to determine the ghost variables, hence the method is simple to implement in multi-dimensions.

The interface speed D is given by:

$$D\vec{N} = \vec{V}_u + S_L\vec{N} = \vec{V}_f \quad (122)$$

where the subscript *u* refers to the unburnt fluid. For the level set function (see Eq (110)), the interface speed *D* has to defined at every grid point in the domain. Since D only depends on the unburnt velocity (see Eq (122)) it can be readily calculated in the unburnt regions. In the burnt regions (i.e. products), the unburnt velocity is extended across the flame by solving the advection equation [60,61]:

$$\frac{\partial I}{\partial \tau} - \bar{N} \bullet \nabla I = 0 \qquad (123)$$

where *I* refers to the individual components of the unburnt velocity and τ is a fictitious time. Eq (123) needs to be solved for a few time steps (~30-50) in a narrow band around the flame.

6.2.4 Boundary Conditions

Characteristic boundary conditions developed by Poinsot & Lele [74] are implemented in the current formulation. At the inlet, velocity and temperature are imposed while the other flow variables are computed using the LODI (locally one dimensional inviscid) relations [74]. At the wall, the normal velocity is imposed to be zero. Non reflecting boundary conditions are imposed at the exit so that the acoustic waves leave the computational domain. The computational domain in the axial direction is chosen to be atleast twice the maximum height of the flame so that the LODI assumptions are valid and reflection of numerical waves is minimized at the exit.

The numerical implementation of the flame anchoring boundary condition requires some care. Note that, in reality, heat losses from the flame to the wall and the low velocity region in the boundary layer help in stabilizing the flame close to the wall. In the current (Eulerian) framework, these effects cannot be taken into account. In order to mimic the low velocity region in the boundary layer (required for the flame to be anchored), the inlet velocity at the wall (see Figure 41) is imposed to be equal to S_L, i.e.,

$$\begin{aligned} u\left(x=0, y\neq\pm R, t\right) &= \overline{u} + u' \, Cos\left(\omega t\right) \\ u\left(x=0, y=\pm R, t\right) &= S_L \\ v\left(x=0, y, t\right) &= 0 \end{aligned} \qquad (124)$$

This approach was found to be numerically robust and the flame was anchored even when the forcing amplitudes were high enough for the flame to be close to flashback.

6.3 Validation Studies

In this section three validation cases are presented for the current solver. The first study corresponds to the evolution of a two-dimensional periodic vortex for the compressible Euler equation [75]. The second study simulates the propagation of a one dimensional flame [61] while the final case computes the growth rate of the Darries-Landau instability [76]. In each of these cases, the computed results are compared with known analytical solutions.

6.3.1 Evolution of Two-Dimensional Periodic Vortex

The periodic vortex problem is set up in a computational domain of [0,10] × [0,10]. Periodic boundary conditions are applied in both the directions. The initial conditions are given by [75]:

$$
\begin{aligned}
u(x,y,0) &= 1-\frac{\varepsilon}{2\pi}\bar{y}e^{0.5\left(1-r^2\right)} \\
v(x,y,0) &= 1+\frac{\varepsilon}{2\pi}\bar{x}e^{0.5\left(1-r^2\right)} \\
T(x,y,0) &= 1-\frac{(\gamma-1)\varepsilon^2}{8\gamma\pi^2}e^{\left(1-r^2\right)} \\
S(x,y,0) &= 1
\end{aligned}
\qquad (125)
$$

where S is the entropy, ε is the vortex strength, γ is ratio of specific heats and

$$
\begin{aligned}
&T = p/\rho, \quad S = p/\rho^{\gamma} \\
&(\bar{x},\bar{y}) = (x-5, y-5), r^2 = \bar{x}^2+\bar{y}^2 \\
&\varepsilon = 5
\end{aligned}
\qquad (126)
$$

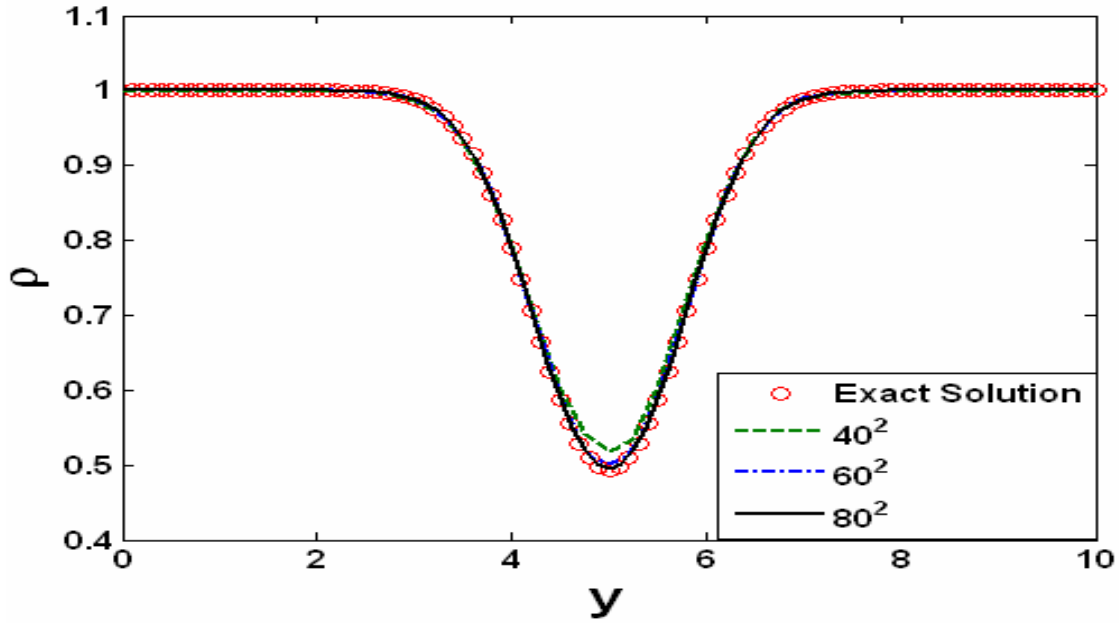

Figure 42 Density profile for the moving vortex problem at *x*=5, *t* =10 for varying grid resolution.

The Euler equations with the above initial conditions admit an exact solution which is convected with the speed (1,1) in the diagonal direction [75]. This flow simulation can be carried out for a very long time due to the periodic boundary condition. The simulation results are shown at t =10 (which corresponds to one time period) in Figure 42. Grid

independence is achieved for a 80^2 mesh and, at this resolution, the computed result is in excellent agreement with the analytical solution (see Figure 42). Next, simulations are carried out up to t=100 (namely 10 time periods). As can be observed in Figure 43, the quality of the solution does not deteriorate even when the simulations are carried out for a long time.

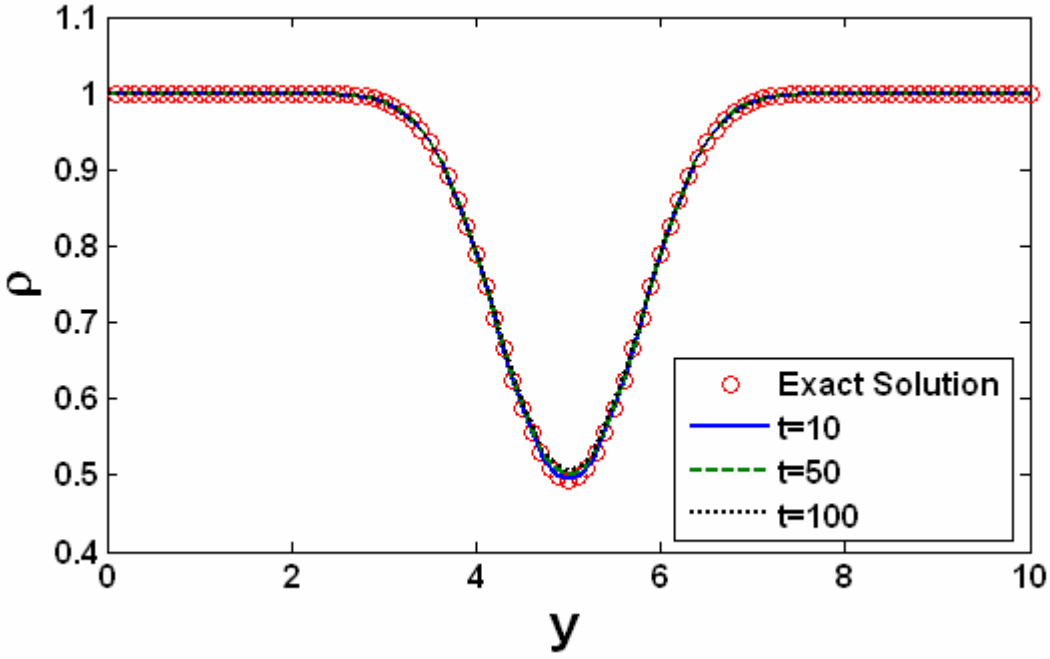

Figure 43 Density profile for the moving vortex problem at *x*=5, *t* =10, 50, 100

6.3.2 Propagation of a One Dimensional Flame

In this test case, a one dimensional flame propagates with a velocity given by [61]:

$$D = V_{N,1} + \left(3\times10^{-9}\right)\left(\frac{p_1}{\rho_1}\right)^2$$

where the subscript "1" denotes unburnt quantities. The computational domain is 1.6 m long with 100 grid points and the flame is located at x=0.8 m. The value of e_o in the unburnt gas is taken to be 2.0×10^6 and 0 in the burnt gas. In addition, ρ=1.14 kg/m^3,

p=98325 Pa, u=33 m/s for the reactants and, ρ=0.145 kg/m^3, p=94284, u=185.2 m/s for the products. Figure 44 shows the solution at t=0.01s after the flame has moved from x=0.8 m to about x=1.1 m at a speed of about 30 m/s. The jump in the primitive variables across the flame is captured without any smearing or numerical oscillations. The results are in agreement with the exact solution shown by the solid line in Figure 44.

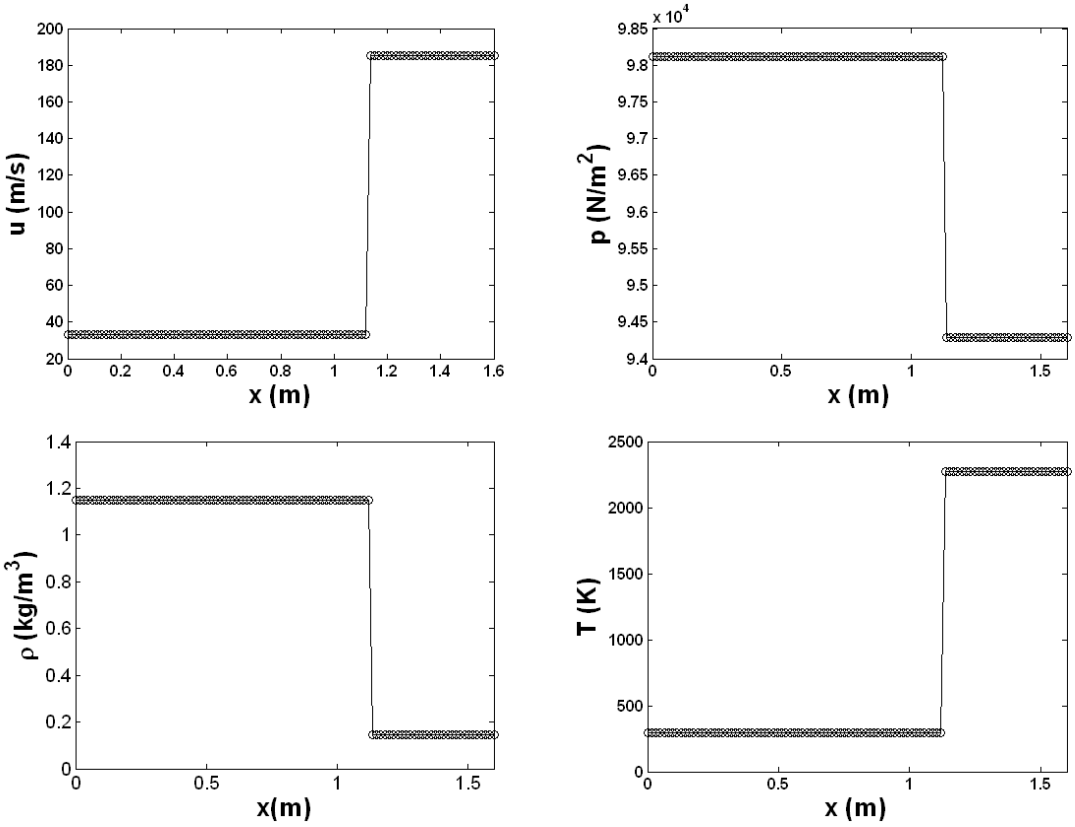

Figure 44 Solution of the one dimensional flame propagation problem at t=0.01 s. Solid line corresponds to the exact solution

6.3.3 Darries-Landau Instability

The Darrius-Landau instability growth rate is computed in a [0,2π/5] × [0, 2π/5] domain with 100 grid points in each direction. The initial profile is a small amplitude cosine wave defined by:

$$y = 0.005\cos(5x) + \pi/5$$

Periodic boundary conditions are applied in the y direction. In the x direction, the inlet velocity and temperature are imposed while non-reflecting boundary conditions are enforced at the outlet. Simulations were carried out by varying the density jump across the flame while keeping the flame speed (S_L) a constant.

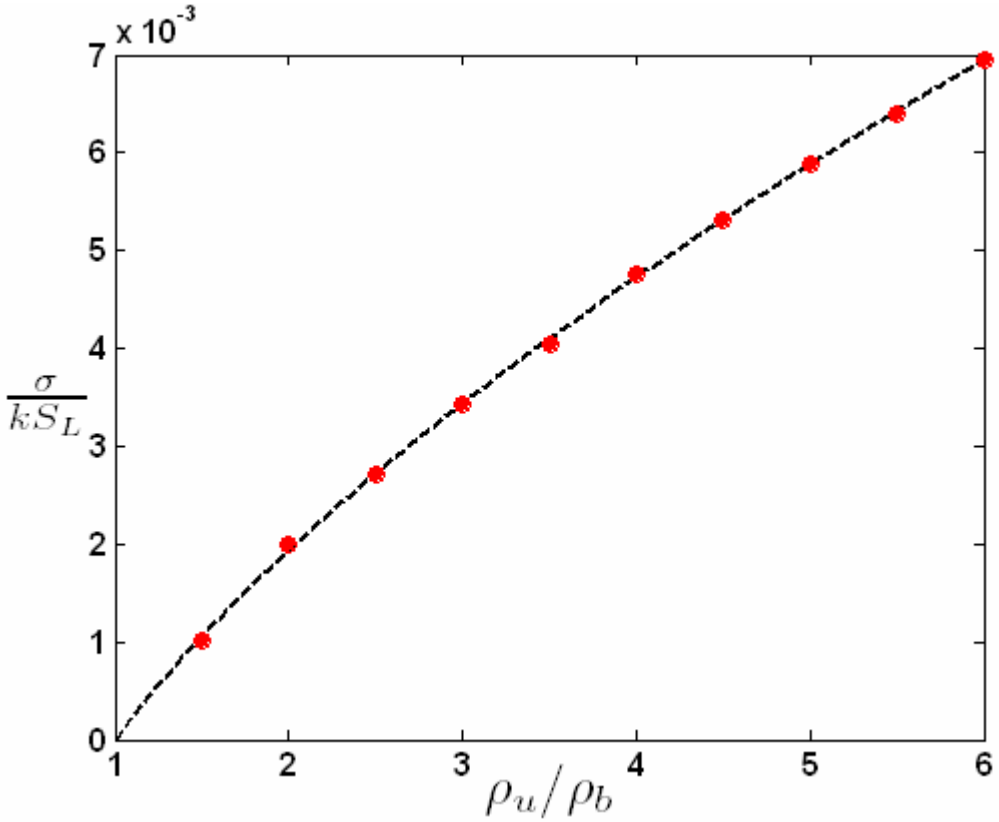

Figure 45 Computation of the Darrius-Landau instability growth rate for different thermal expansion ratios. Dashed line corresponds to the theoretical solution.

The Darrius-Landau instability results in exponential growth of the amplitude of the flame, with the growth rate (σ) give by [76]:

$$\frac{\sigma}{S_L k} = \Gamma_o + \Gamma_1 M_f^2$$

$$\Gamma_o = \frac{\Theta}{(\Theta+1)}\left(\sqrt{\Theta+1-\frac{1}{\Theta}}-1\right)$$

$$\Gamma_1 = \frac{\Theta}{2}\frac{\Gamma_o(\Gamma_o+1)}{\Gamma_o(\Theta+1)+\Theta}\left(\Theta-1+\frac{1}{2\Theta}\frac{\Theta^2-\Gamma_o^2}{1-(\Theta-1)M_f^2}+\frac{(\Gamma_o+1)^2}{2}\right)$$

where k is the wavenumber of the disturbance, M_f is the flame speed Mach number and Θ is the density ratio of the unburnt to the burnt gas. From the time evolution of this disturbance in the initial stages, the growth rate of the amplitude is computed for a range of Θ. The computed growth rate of the disturbance is in good agreement with the predictions from linear theory as shown in Figure 45.

6.3.4 Two Dimensional Anchored Flames

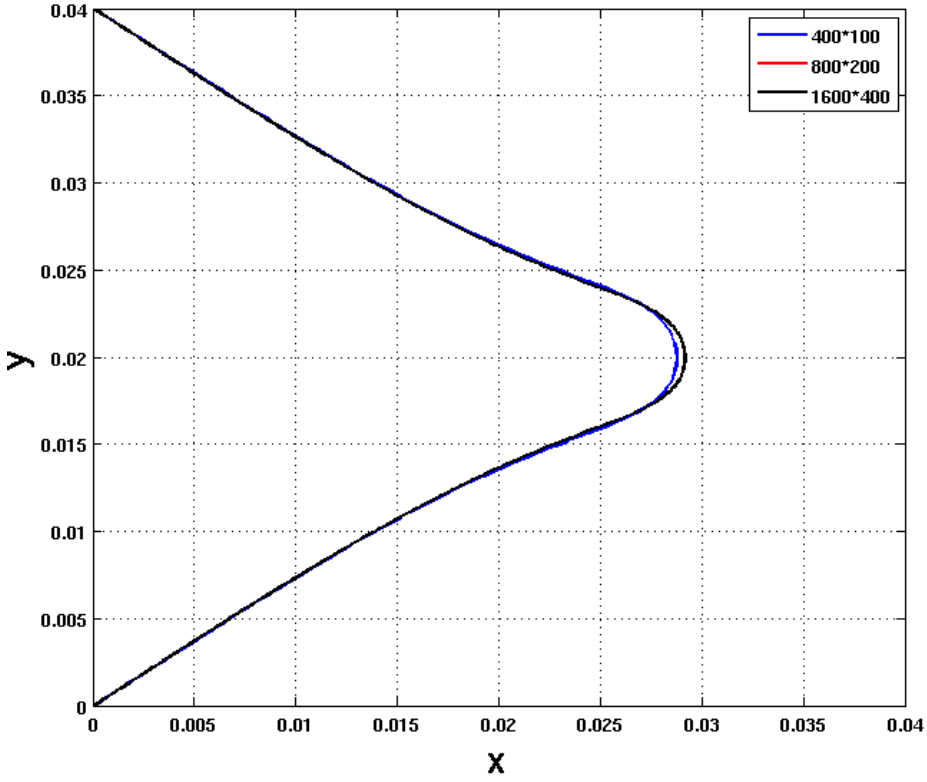

Figure 46 Steady state profile of an anchored two dimensional flame with varying grid resolution. Note that the computational domain extends upto X = 0.16 m (i.e. much larger than the region shown in the figure).

The steady state profile of an anchored two dimensional flame is shown in Figure 46. The simulations correspond to a [0, 0.16 *m*] × [0, 0.04 *m*] computational domain with S_{Lo}/u_o=0.5 and T_b/T_u=2. The grid (see Figure 46) is varied from 400×100 (i.e. *dx* = *dy* = 0.0004 *m*) to 1600×400 (i.e. *dx* = *dy* = 0.0001 *m*). The Markstein length was taken to be 0.001 *m*, CFL = 0.5 and the flame was anchored at (0,0) and (0,0.04 *m*). Wall boundary conditions are applied at *y* = 0, 0.04m and inlet/non-reflecting conditions at *x* = 0, 0.16 *m*. Grid independence is achieved beyond a spatial resolution of 800×200 (i.e. *dx* = *dy* =0.0002 *m*) points. At this spatial resolution, the loss in mass conservation associated with the (non-conservative) *G*-equation was found to less than 3.5% even when the simulations were carried out for 5 flow-through times.

In summary, the numerical scheme for the current solver has been tested on several benchmark problems and has been shown to be stable and accurate. Specifically, it has been shown to be successful in simulating the flame dynamics with realistic thermal expansion ratios.

CHAPTER 7

FLAME RESPONSE: EFFECT OF GAS EXPANSION

Prior chapters have considered the response of a premixed flame to an imposed disturbance. In reality, the flame alters the character of the disturbance, so that the problem is coupled. In this chapter, we allow for this coupling and therefore, solver for, rather than prescribe the disturbance field. Specifically, the impact of T_b/T_u on the heat release response of ducted premixed flames is analyzed. An unsteady compressible Euler solver coupled to the *G*-equation is developed to study the interaction between the unsteady flow field and flame. It is shown that flame confinement (due to the burner duct) has a strong impact on the mean and unsteady flow field characteristics. Essentially, the no-penetration condition at the wall causes the time-averaged (unburnt) tangential velocity along the flame front to accelerate. This causes the effective residence time of the flame wrinkles to vary with T_b/T_u although the flame has the same frequency of forcing, approach flow velocity and mean flame length. The perturbation velocity field magnitude has a significant spatial dependence and is shown to be much higher than the velocity excitation amplitude at the flame base. Furthermore, a theoretical analysis is developed to understand the effect of spatial non-uniformity of the mean and disturbance flow-field characteristics on the flame response. An explicit analytical expression is obtained for the effective Strouhal number controlling the flame response. It also yields insight to determine an effective reference velocity for defining heat release transfer functions which can then be consistently compared across T_b/T_u. Heat release transfer function gains show a strong dependence on T_b/T_u when the flame base excitation

amplitude is used as the reference velocity and the Strouhal number is based on the mean inlet velocity. Once the gains across T_b/T_u are corrected for the effective Strouhal number and reference velocity magnitude, good agreement is obtained with the gain predictions from constant density theory.

7.1 Flame Configuration and Simulation Parameters

In the current investigation, a ducted two dimensional flame anchored at the base is subjected to harmonic acoustic forcing. The flame base coincides with the inlet of a constant diameter duct (see Figure 41). Simulations are carried out for a range of excitation amplitudes (up to flashback) and Strouhal numbers (St~5-72) with T_b/T_u varying from 1 to 6. The Markstein length, which accounts for the variation of the flame speed with stretch (see Eq. (20)), normalized by the burner diameter is kept constant at 0.025.

7.2 Flame Flow-field Interaction

The steady state flame shape in the absence of acoustic excitation is shown in Figure 47. These simulations correspond to S_{Lo}/u_o=0.5 and T_b/T_u=6. The flame is anchored at the inlet of the burner wherein the flow enters the in the axial direction. At the burner centerline, the flame tip is rounded due to the effect of curvature on the flame speed. The velocity vectors (represented by arrows) are also shown to illustrate the velocity field. The deflection of the stream lines (towards the flame normal) on crossing the flame front and the corresponding jump in the burnt gas velocity can be clearly observed. Note that the computational domain is much larger than the region shown in Figure 47.

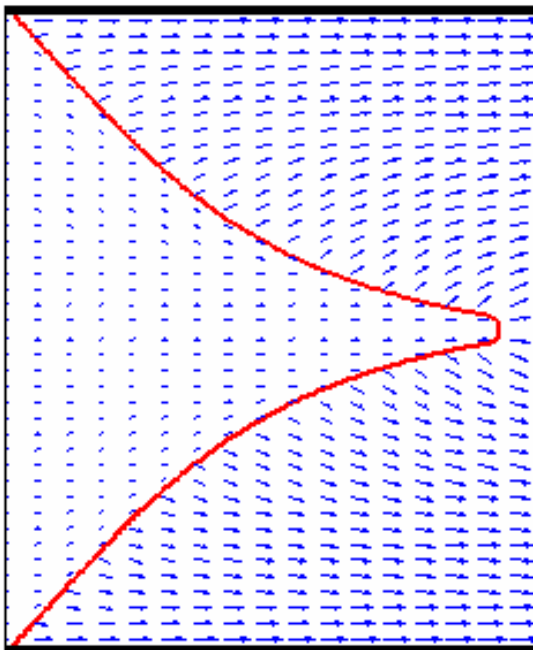

Figure 47 Steady state flame shape and velocity vectors in the absence of acoustic forcing, S_{Lo}/u_o=0.5, T_b/T_u=6. Note that the computational domain is much larger than the region shown in the figure.

Figure 48 shows the instantaneous flame position and the corresponding velocity vectors at ten different instances in an acoustic cycle. These simulations correspond to St=5, S_{Lo}/u_o=0.5, ε=0.5 and T_b/T_u=6. Note that for this frequency of forcing, the acoustic wavelength is longer than the mean flame height. During the first half of the acoustic cycle (see t=0-0.4τ cases in Figure 48), the flame tip progressively moves outward while the flame elements closer to the base propagate inward and vice-versa in the second half of the acoustic cycle (see t=0.5τ-0.9τ cases). The presence of the flame (deflection of streamlines with corresponding normal velocity jump) and the wall (i.e. zero wall normal velocity) causes the velocity field to have a "wake like" profile.

In order to gain insight into the local disturbance field perturbing the flame, the axial and transverse components are shown in Figure 49 and Figure 50 respectively. Moreover, the

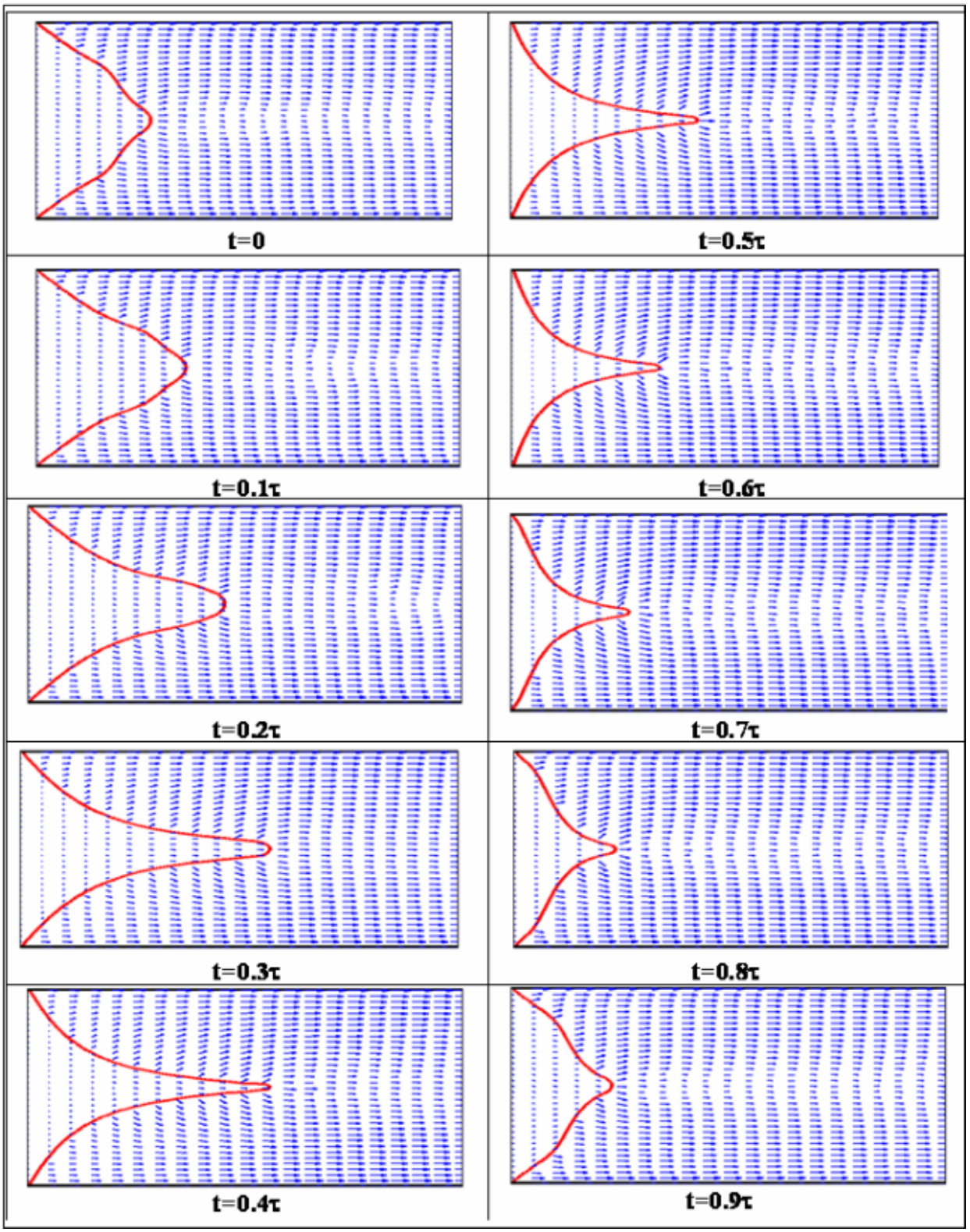

Figure 48 Flame front position and velocity vectors at different instants in an acoustic cycle. S_{Lo}/u_o=0.5, ε=0.5, St=5, T_b/T_u=6, τ is the acoustic time period

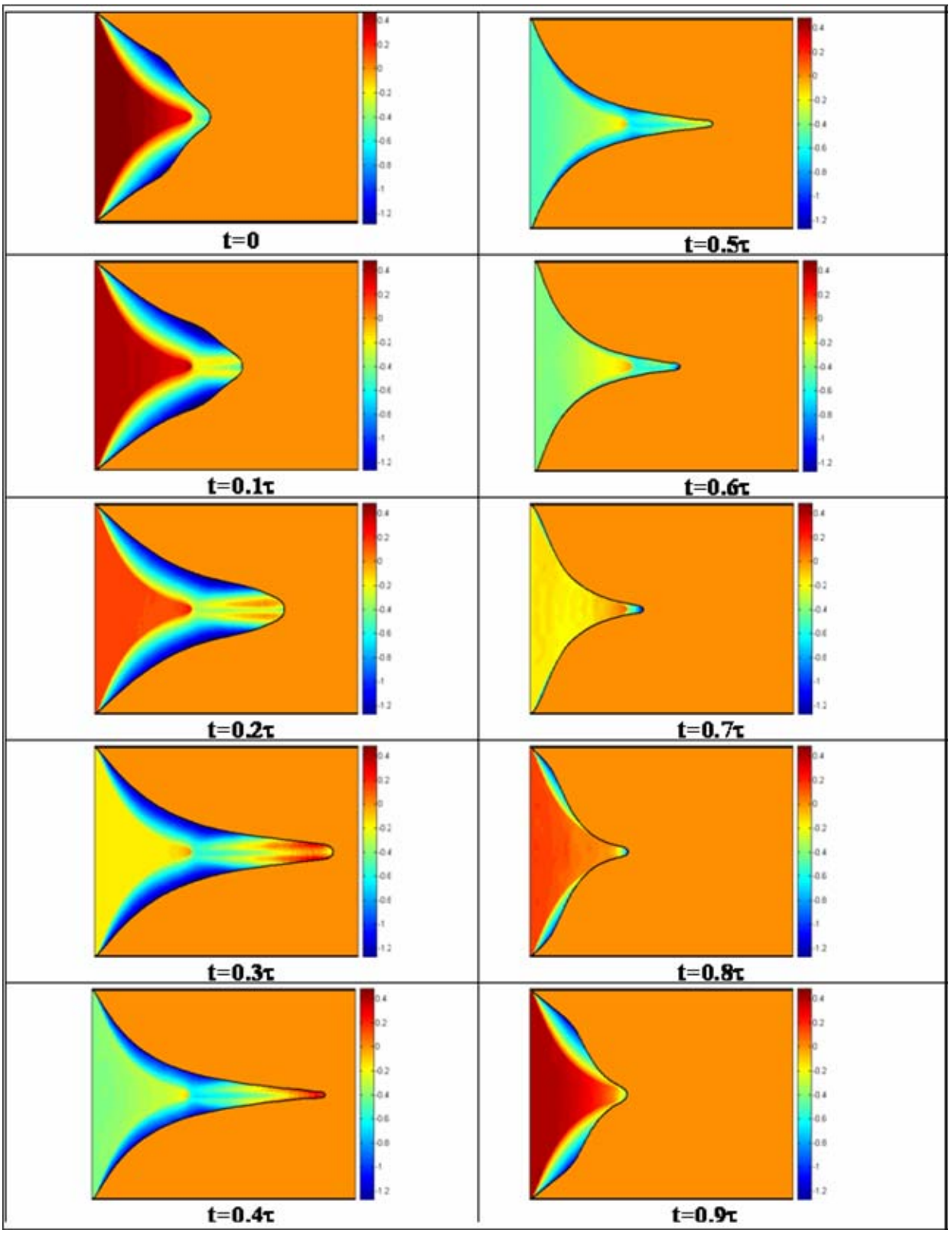

Figure 49 Instantaneous axial disturbance field (u') at different instants in an acoustic cycle. S_{Lo}/u_o=0.5, ε=0.5, St=5, T_b/T_u=6. Scale normalized by u_o, τ is the acoustic time period

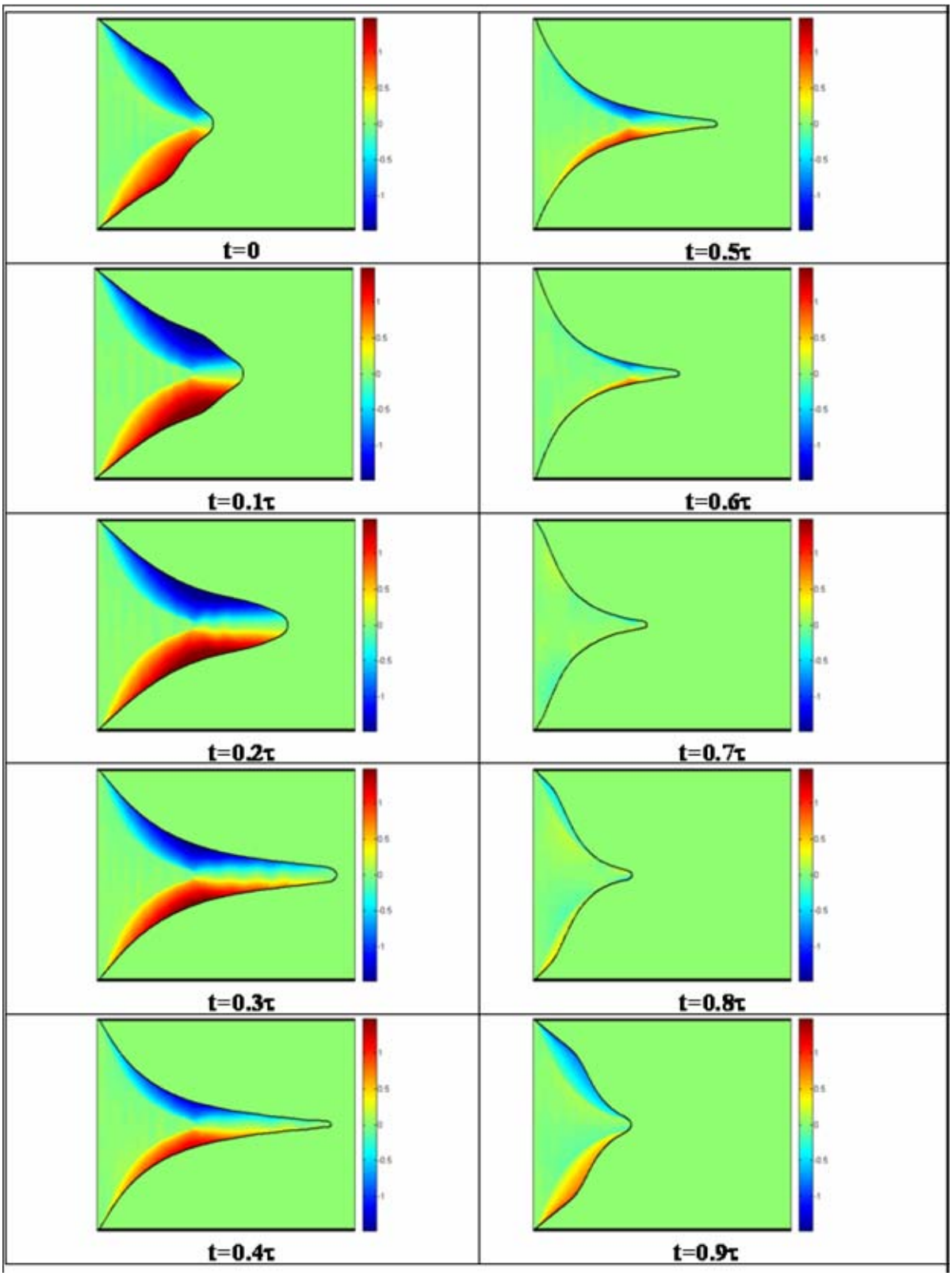

Figure 50 Instantaneous transverse disturbance field v' at different instants in an acoustic cycle. S_{Lo}/u_o=0.5, ε=0.5, St=5, T_b/T_u=6. Scale normalized by u_o, τ is the acoustic time period

disturbance velocity field has been set to zero in the burnt gases in order to highlight the flow-field features upstream of the flame. It can be clearly observed that the u' field is purely acoustic in nature away from the flame. However, close to the flame, the disturbance flow field is strongly modified. This can be inferred for the t=0 case (see Figure 49) wherein the value of u'/u_o changes from 0.5 to ~ -1.2. This strong deceleration is imposed by the wall as the flame element near the base has to move inward so that the flow (i.e. burnt gas which has a much higher velocity) can satisfy the no-penetration condition at the wall. Similarly, the wall enhances the amplitude of the transverse fluctuations, v'/u_o, from zero (away from the flame) to ~±1 closer to the flame (see Figure 50). The zone wherein the upstream disturbance field is strongly modified is much broader when the bulk of the flame is moving outward (i.e. closer to the wall as in t=0-0.4τ cases in Figure 49 and Figure 50) than when moving inward (see t=0.5-0.9τ cases). These features highlight the strong influence of the burner wall on the upstream disturbance field characteristics. In essence, *the disturbance field amplitude actually perturbing the flame surface is much higher in magnitude than the amplitude of excitation at the flame base*. This fact will be important when comparing heat release transfer functions across different T_b/T_u.

Figure 51 and Figure 52 show the instantaneous flame position along with the (u',v') field for St=24.32 while Figure 53 and Figure 54 correspond to a St=73 simulation. Both these cases have a higher flame aspect ratio (S_{Lo}/u_o=0.25) in comparison to the case considered till now. As pointed out earlier in the context of Figure 49, the u' disturbance field is purely acoustic in nature close to the flame base. However, in the region close to the flame tip (see Figure 53), the disturbance field has both convective and acoustic

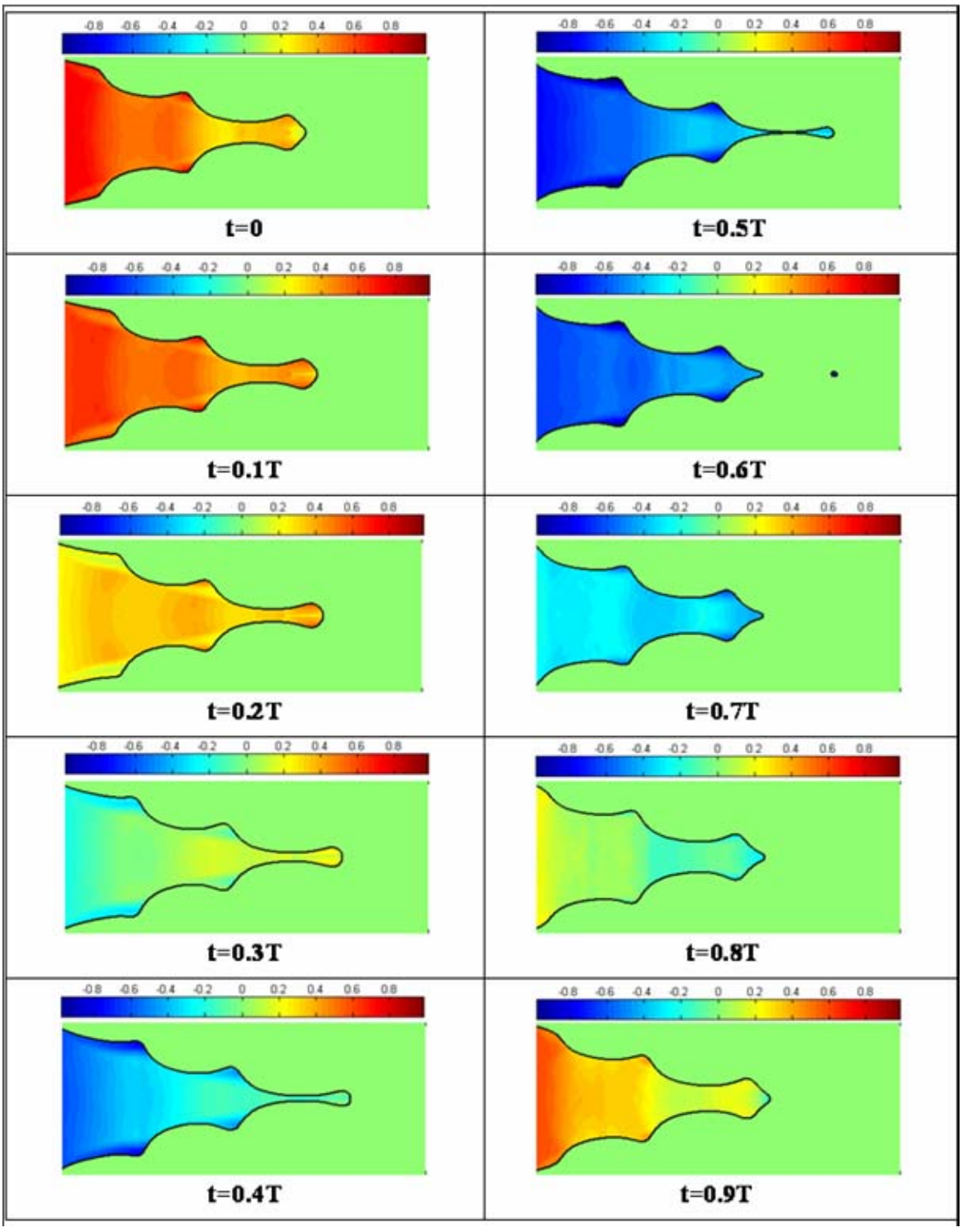

Figure 51 Fluctuating axial velocity disturbance field (u') at different instants in an acoustic cycle. S_{Lo}/u_o=0.25, ε=0.75, St=24.32, T_b/T_u=2. Scale normalized by u_o, τ is the acoustic time period

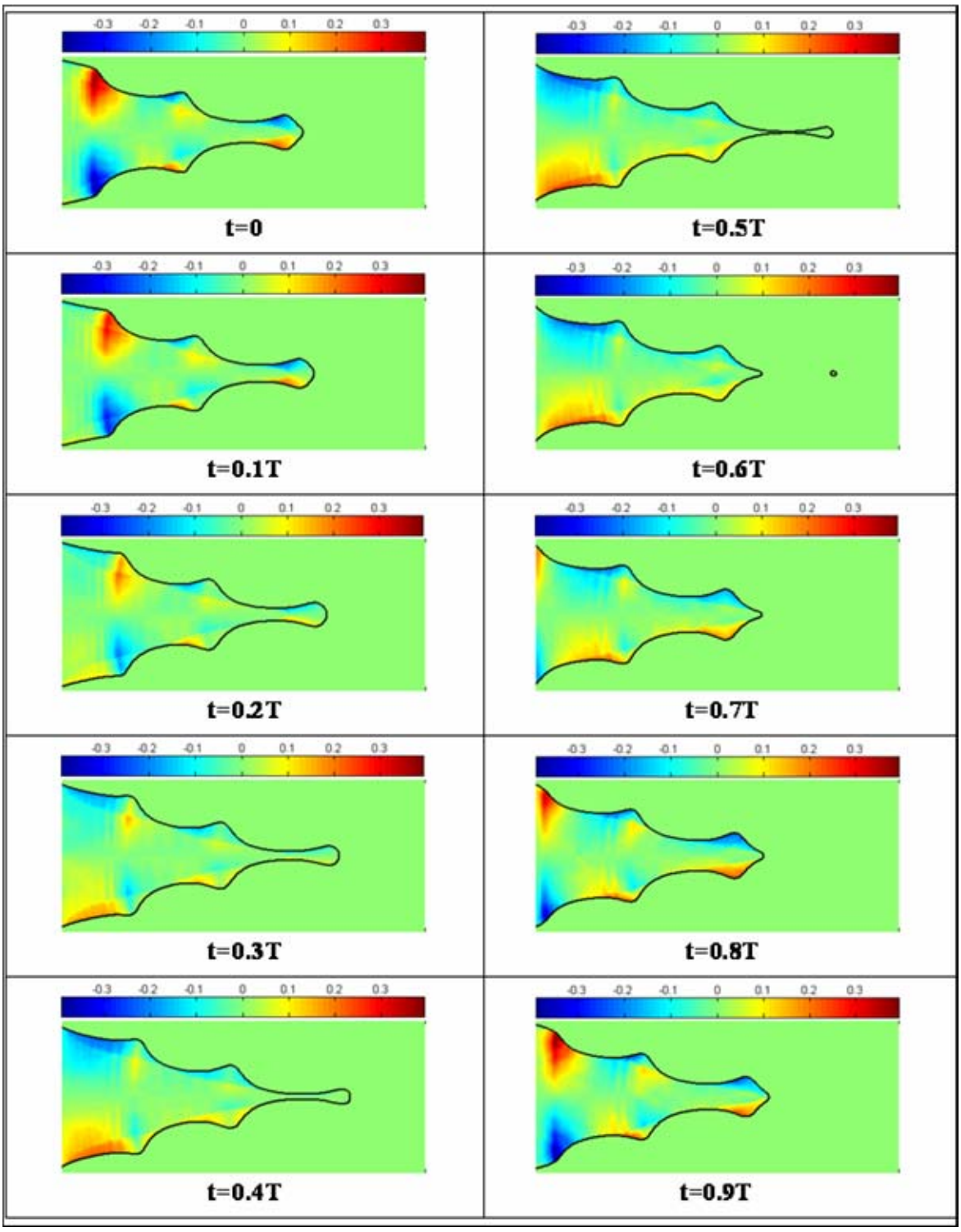

Figure 52 Fluctuating transverse velocity disturbance field (v') at different instants in an acoustic cycle. S_{Lo}/u_o=0.25, ε=0.75, St=24.32, T_b/T_u=2, Scale normalized by u_o, τ is the acoustic time period

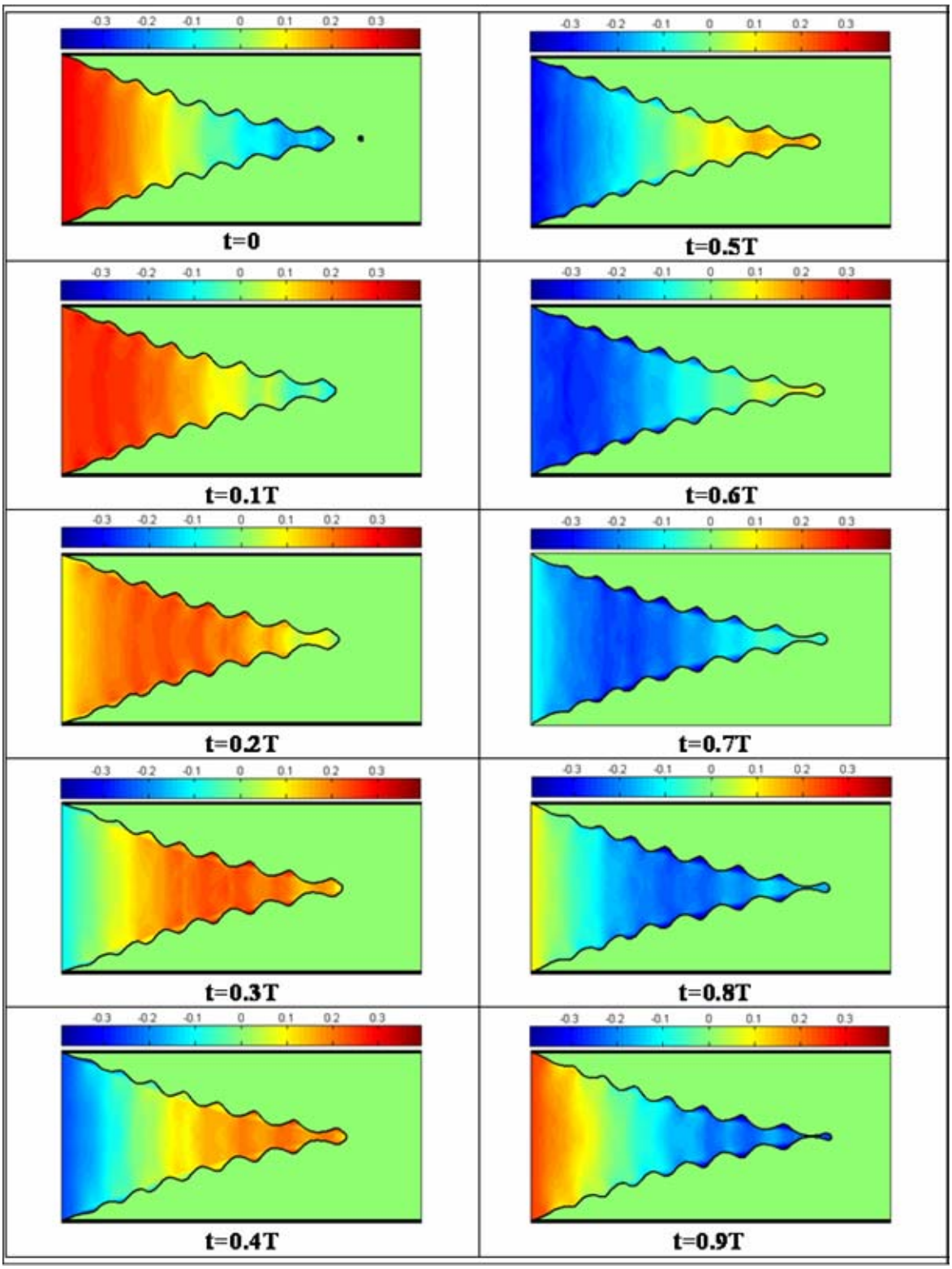

Figure 53 Instantaneous axial disturbance field (u') at different instants in an acoustic cycle. S_{Lo}/u_o=0.25, ε=0.3, St=73, T_b/T_u=2, Scale normalized by u_o, τ is the acoustic time period

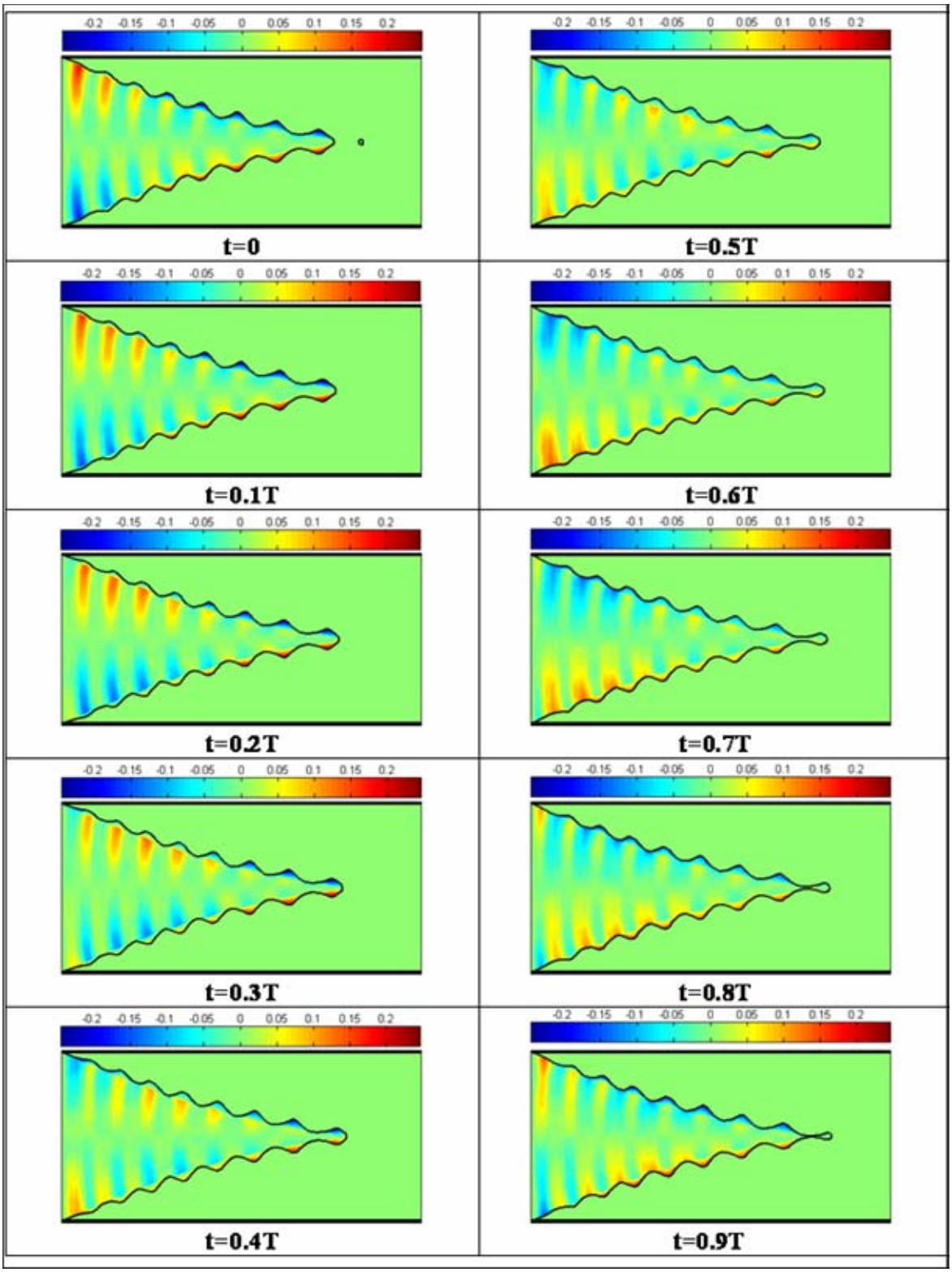

Figure 54 Instantaneous transverse disturbance field (v') at different instants in an acoustic cycle. S_{Lo}/u_o=0.25, ε=0.3, St=73, T_b/T_u=2, Scale normalized by u_o, τ is the acoustic time period

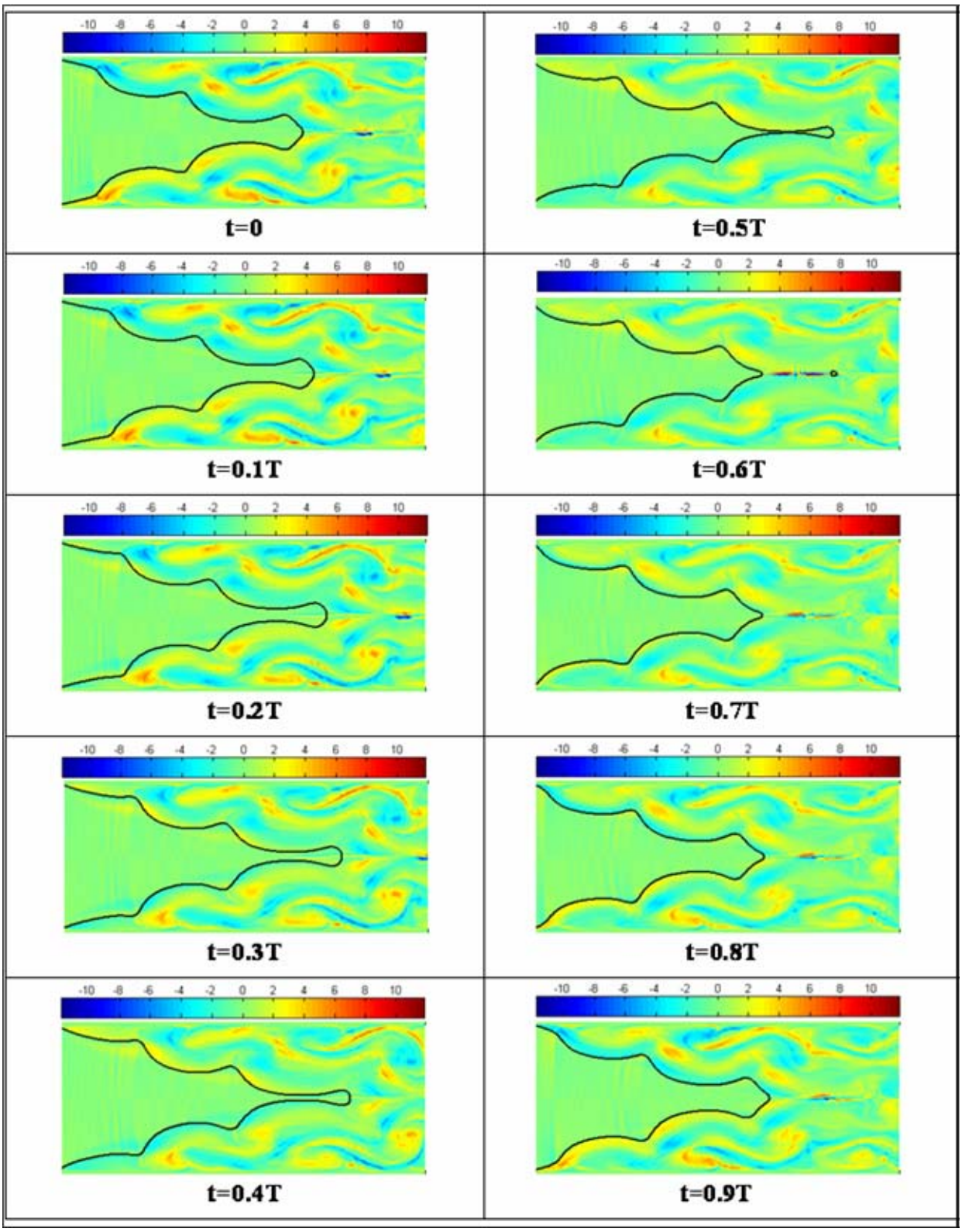

Figure 55 Instantaneous unsteady vorticity field snapshot at different instants in an acoustic cycle. S_{Lo}/u_o=0.25, ε=0.75, St=24.32, T_b/T_u=2, Scale normalized by u_o and R , τ is the acoustic time period

characters. This change in the disturbance field structure is enhanced as the wavelength of the wrinkle gets shorter (i.e. higher frequency of forcing). Note the presence of "bands" whose width corresponds to the wavelength of the wrinkle. At some time instants (e.g. see the regions close to the flame tip for t=0.1τ and t=0.6τ cases in Figure 53) these "bands" have opposite signs indicating the presence of a convective wave. However, in the majority of the cases (also see Figure 51), the amplitude of the convective wave is smaller in comparison to the acoustic wave leading to the formation of "bands" which are not necessarily of opposite signs. The v' field disturbance field amplitude is as strong as the u' field (see Figure 52 and Figure 54) close to the flame cusp regions. The strong influence of the wall is responsible for the v' field to be of the opposite sign close to the base in comparison to the region close to the flame tip (i.e. compare the sign of v' near the first three wrinkles close to the flame base with the wrinkles further downstream in Figure 54).Moreover, the strength of the v' field decays towards the axis which can be anticipated due to symmetry.

A typical evolution of the unsteady vorticity field structure in an acoustic cycle (for the St=24.32 case) is shown in Figure 55. The induced vorticity field upstream of the flame is very weak. However, a strong vorticity field is generated downstream of the flame with the strength being higher close to the flame cusps. Moreover, events like flame pocket burnout (see t=0.6τ -0.7τ cases in Figure 55) lead to extremely high levels of unsteady vorticity. These structures then convect out of the domain without decay due to the viscous effects being neglected.

Another key point to note is that the mean flow accelerates in the axial direction due to gas expansion effects. This is illustrated in Figure 56 and Figure 57, which show the

time-averaged normal and tangential velocity at the flame front (normalized by u_o), for different T_b/T_u. These simulations correspond to St=5, S_{Lo}/u_o=0.5 and ε=0.1. Consider the $T_b/T_u \rightarrow 1$ case first (red line in Figure 56 and Figure 57). Except for regions close to the tip, the time averaged normal velocity at the flame front is equal to the unstretched flame speed (i.e. equal to S_{Lo}/u_o). At the tip, the flame speed increases to a value equal to the mean axial velocity (i.e. $S_L/u_o \rightarrow 1$) in order to achieve kinematic balance (see Figure 56). The time averaged tangential velocity is also constant for a major part of the flame and then drops down to zero at the flame tip (see Figure 57). However, for higher T_b/T_u, the mean axial velocity is accelerated which implies that the flame speed at the tip has to correspondingly increase to achieve kinematic balance. The mean axial velocity at the flame tip monotonically increases with T_b/T_u (see Figure 56) and reaches a value greater than $2u_o$ for T_b/T_u=6. Moreover, the tangential velocity increases monotonically with T_b/T_u and can go as high as 2.5 u_o for T_b/T_u=6 (see Figure 57).

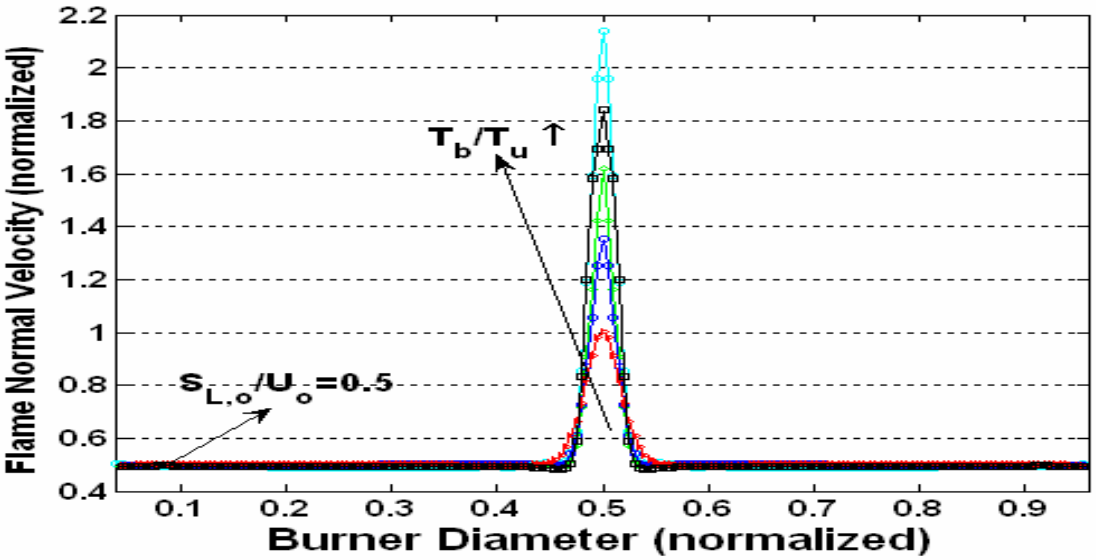

Figure 56 Time-averaged normal velocity at the flame (normalized by u_o) as a function of T_b/T_u. S_{Lo}/u_o=0.5, ε=0.1, St=5, T_b/T_u=1, 2, 3, 4, 6

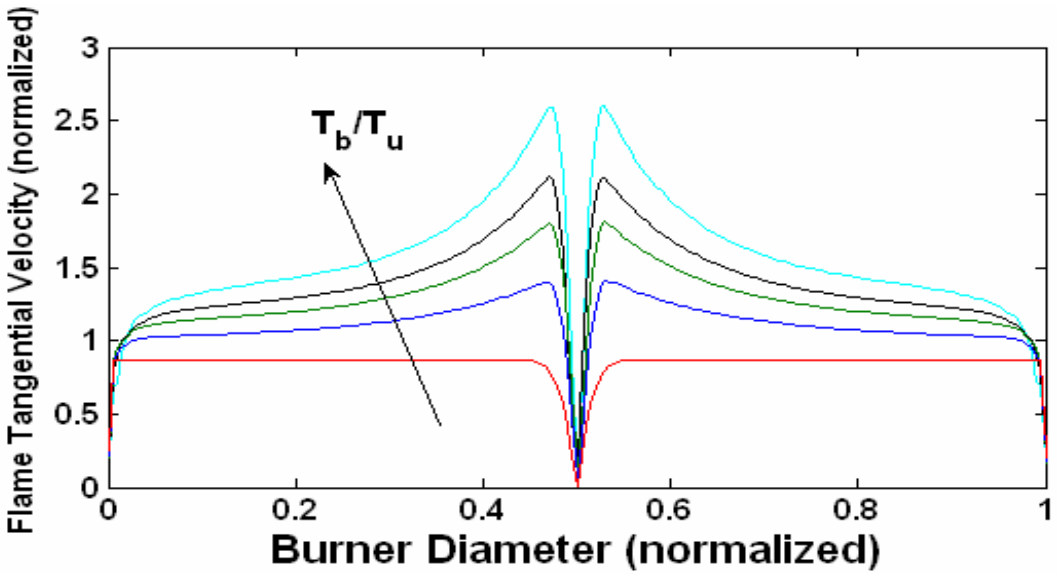

Figure 57 Time-averaged tangential velocity at the flame (normalized by u_o) as a function of T_b/T_u, S_{Lo}/u_o=0.5, ε=0.1, St=5, T_b/T_u=1, 2, 3, 4, 6

The enhanced tangential velocity along the flame front can be attributed to the effect of burner wall. Note that for the simulations reported in Figure 56 and Figure 57, the unstretched flame speed, S_{Lo}, has been kept constant. The normal velocity upstream of the flame is essentially controlled by S_{Lo} (see Figure 56) to achieve kinematic balance. Also, the parameter T_b/T_u controls the normal velocity downstream of the flame. So the only way that the wall can enforce the zero wall normal velocity condition is by controlling the flame tangential velocity on the burnt side. Since the tangential velocities are constant across the flame front, this implies that *the flame tangential velocity on the unburnt side is controlled by the wall*. This explains the strong variation of the time averaged flame tangential velocity with T_b/T_u in Figure 57. In summary, *the mean axial velocity at the flame tip and the time averaged tangential velocity along the flame front (except at the tip) are substantially higher in comparison to the* $T_b/T_u \rightarrow 1$ *case*. This is another key fact which will have to be considered when comparing flame responses across different T_b/T_u.

Another consequence of having a variable mean flame tangential velocity (e.g. see Figure 57) is that the wrinkle wavelength continually changes as it moves from the flame base to the tip. This broadening of the wavelength as the wrinkle propagates towards the flame tip can be clearly seen in the instantaneous flame shape contours presented in Figure 51 and Figure 53.

7.3 Flame Response Characteristics

Before considering specific results on the impact of T_b/T_u on the flame heat release transfer function, several general conclusions can be drawn from analysis of the governing equations. The general solution for the fluctuating flame area (two-dimensional case) in a non uniform mean velocity field ($\overline{u},\overline{v}$), can be expressed as (see Appendix B for derivation, Figure 12 for the schematic and also Section 2.4 for prior discussion):

$$\frac{\hat{A}}{A_o} = \frac{\beta^2}{\sqrt{1+\beta^2}} e^{-iStH(0)} \frac{\overline{\zeta}_r(0)}{P(0)} \chi(0) + \frac{\beta}{\sqrt{1+\beta^2}} \int_0^1 \left(e^{-iStH(r)} \kappa(r) \chi(r) \right) dr \qquad (127)$$

where

$$\begin{aligned}
\chi(r) &= \int_1^r \left(e^{iStH(\theta)} \frac{P(\theta)\hat{u}_n(\theta)}{F(\theta)} \right) d\theta \\
F(r) &= \frac{\beta \overline{u}_t}{\sqrt{1+\beta^2 \overline{\zeta}_r^2}} \\
P(r) &= \sqrt{1+\beta^2 \overline{\zeta}_r^2} \\
\kappa(r) &= \beta \left(\frac{\overline{\zeta}_r}{P(r)} \right)_r = \frac{\beta \overline{\zeta}_{rr}}{\left(1+\beta^2 \overline{\zeta}_r^2\right)^{3/2}} \\
H(r) &= \int_1^r \frac{1}{F(r)} dr
\end{aligned} \qquad (128)$$

and the subscripts *n*,*t* denote normal and tangential respectively. In Eq (127), (u,v) has been non-dimensionalized using the *inlet* mean flow velocity (u_o), flame position coordinate ζ by mean flame length L_f and *r* by the burner radius *R*. The flame aspect ratio, L_f/R, is denoted as β.

As discussed earlier in Section 2.4, Eq. (127) *explicitly* brings out the characteristic frequency controlling the flame response as:

$$-StH(0) = St\int_0^1 \frac{1}{F(r)}\,dr = St\int_0^1 \frac{\sqrt{1+\beta^2\bar{\zeta}_r^2}}{\beta\bar{u}_t}\,dr = \frac{St}{\beta}\int_0^1 \frac{dl_F}{\bar{u}_t} \quad (129)$$

Note that in Eq (129), $dl_F / \bar{u}_t$ corresponds to the time it takes for the wrinkle to propagate a distance, dl_F, along the mean flame front with the flame tangential velocity $\bar{u}_t$. So the characteristic frequency is essentially an integrated measure of the time it takes for the wrinkle to propagate from the flame base to the tip, normalized by the acoustic time period (τ). As discussed in the context of Figure 57, the local value of $\bar{u}_t$ increases monotonically with increase in T_b/T_u. So, although the flame might be excited at the same frequency and have approximately the same mean flame length (which is the case for the transfer function results to be reported later), the *effective* Strouhal number *decreases* with increasing T_b/T_u due to the corresponding increase in $\bar{u}_t$ (see Eq (129)).

For the special case of uniform axial mean flow, Eq (127) reduces to:

$$\frac{\hat{A}}{A_o} = \int_0^1 \sqrt{1+\beta^2}\, e^{irSt_2}\hat{u}_n(r)dr \qquad (130)$$

In this simplified situation, the flame response is driven by the correlation between the perturbation velocity normal to the flame ($\hat{u}_n$) and the harmonic term, e^{irSt_2}. Note that

in the limit of *low Strouhal numbers, the flame response is only driven by the integral of the normal perturbation velocity over the flame front*, i.e.,

$$\frac{\hat{A}}{A_o} \approx \int_0^1 \sqrt{1+\beta^2}\,\hat{u}_n(r)dr \qquad (131)$$

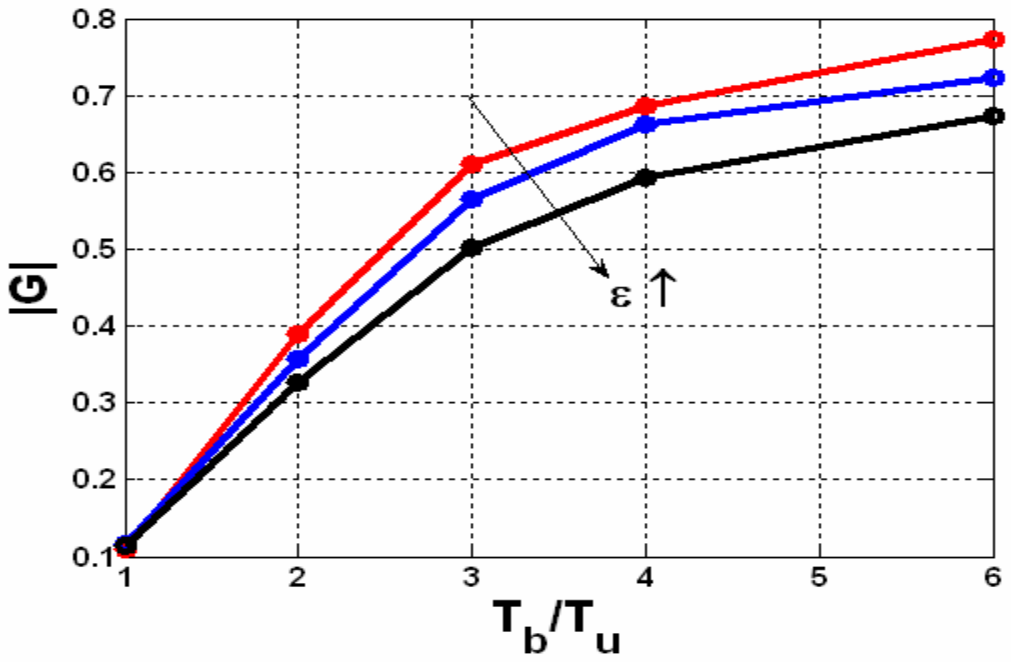

Figure 58 Flame heat release transfer function gain as a function of T_b/T_u for increasing values of excitation amplitude. S_{L_o}/u_o=0.5, ε = 0.1, 0.3, 0.5, St=5

It can be inferred from Eq. (127) and (130) that the flame response is strongly controlled by perturbation velocity normal to the flame ($\hat{u}_n$).Even if the velocity excitation amplitude at the flame base is the same, the flame will be locally perturbed by different values of $\hat{u}_n$ (see Figure 49 and Figure 50) as T_b/T_u increases. Moreover, the *spatial variation of the mean flame curvature* is a strong function of T_b/T_u and enhances fluctuations in the flame area (see the term $\kappa(r)$ in Eq.(127)). So it is critical to define a physically useful reference velocity, u'_{ref}, for the transfer function in order to meaningfully compare flame transfer functions as a function of T_b/T_u. *Thus comparing*

the flame response across different T_b/T_u cases requires some care as the mean tangential velocity ($\overline{u}_t$) and the perturbation velocity magnitude ($\hat{u}_n$) varies along the flame front.

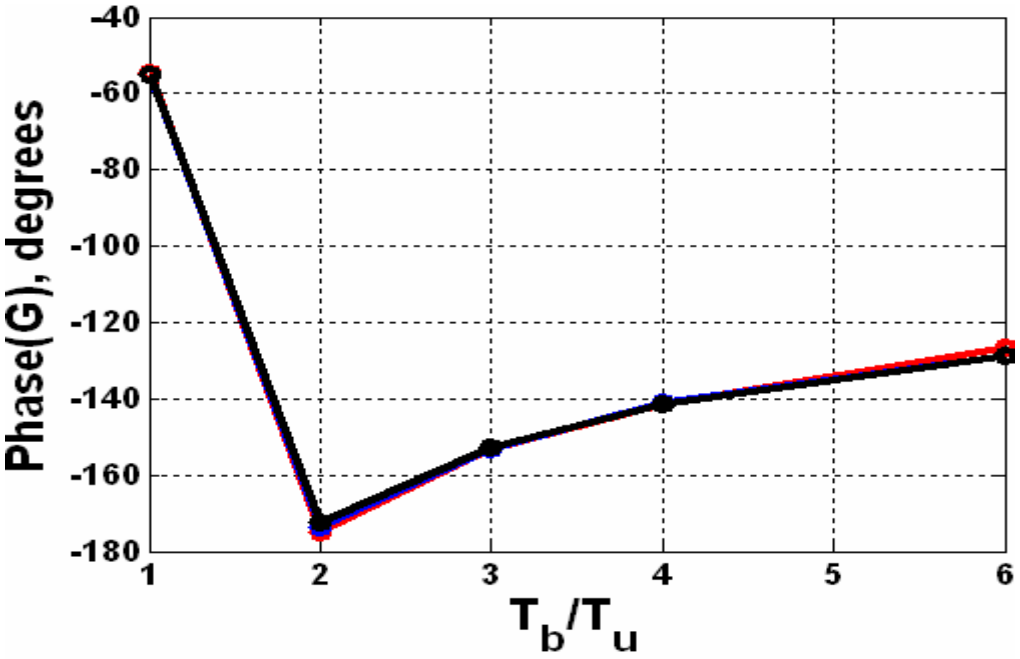

Figure 59 Flame heat release transfer function phase as a function of T_b/T_u for increasing values of excitation amplitude. S_{Lo}/uo=0.5, ε=0.1, 0.3, 0.5, St=5

The heat release transfer function gain and phase are shown in Figure 58 and Figure 59 respectively. These simulations correspond to the same parameters as considered before, i.e., St=5, S_{Lo}/u_o=0.5 with varying values of T_b/T_u and ε. The ε=0.5 corresponds to the highest possible amplitude before flashback. Also note that these transfer functions are defined with reference to the axial velocity perturbation at the flame base ($G_{u'_{base}}$). The gain increases monotonically with T_b/T_u with the sensitivity being higher at lower T_b/T_u (see Figure 58). The acceleration of the mean flow with increasing T_b/T_u is responsible for the strong variation of the transfer function phase (see Figure 59). However, it is insensitive to the amplitude of excitation. In contrast, the gain (see Figure 58) decreases monotonically with increasing velocity amplitude. In order to get further

insight, consider the T_b/T_u dependence of the gain for the ε=0.1 case first. This trend can be anticipated based on two specific points highlighted in prior discussion, i.e., normal velocity perturbation amplitude and effective Strouhal number. As was shown in Eq.(127), the heat release response is controlled by the normal velocity amplitude perturbing the flame ($\hat{u}_n$). This value is much higher than the value at the flame base (see Figure 49 and Figure 50). Since the reference velocity amplitude (i.e. value at flame base) is an underestimate of the actual magnitude at the flame front, the gain will clearly come out higher when T_b/T_u>1. Based on Eqs.(127) and (130), it can be inferred that an *effective* normal velocity perturbation amplitude, obtained by averaging ($\hat{u}_n$) over the entire flame, is a better measure of the reference amplitude actually perturbing the flame. Using the axial component of this *effective* normal perturbation velocity (see Eq. (132) and Eq. (131)) as the reference velocity for defining the transfer function ($G_{u'_{ref}}$), the gain differential across T_b/T_u reduces drastically in comparison to the original definition (see Figure 60 for comparison between $G_{u'_{ref}}$ and $G_{u'_{base}}$).

$$u'_{ref} = \sqrt{1+\beta^2}\,\frac{\int_0^1 \hat{u}_n(r)dr}{\int_0^1 dr} \qquad (132)$$

Secondly, the effective Strouhal number drops with increasing T_b/T_u due to the corresponding increase in $\bar{u}_t$ (see Figure 57 and the discussion related to Eq.(129)). From Figure 57, it can be estimated that $\bar{u}_t$, when averaged over the whole flame front, approximately increases by a factor of two for the T_b/T_u=6 case in comparison to the $T_b/T_u \to 1$ case. *This translates into a significant difference in the wrinkle residence time*

and consequently the effective Strouhal number (e.g. the effective $St_2 = St\,H(0)$, see Eq. (129),changes from 7.25 for $T_b/T_u \to 1$ to ~4.13 for $T_b/T_u=6$). This point is illustrated in Figure 61 which shows the Strouhal number dependence of the gain based on *linear theory* for the $T_b/T_u \to 1$ case (see Chapter 4 for details). As the effective Strouhal number (St_2) decreases from 7.25 to 4.13 (see the movement of the black circles in Figure 61), the gain increases by a factor of four. The gain values corresponding to this effective Strouhal number ($G_{Theory,St_{eff}}$) are plotted in Figure 60 for comparison. Clearly, the agreement between the gain based on the effective reference velocity ($G_{u'_{ref}}$) and the gain prediction for the $T_b/T_u \to 1$ case corresponding to the effective Strouhal number ($G_{Theory,St_{eff}}$) gets better.

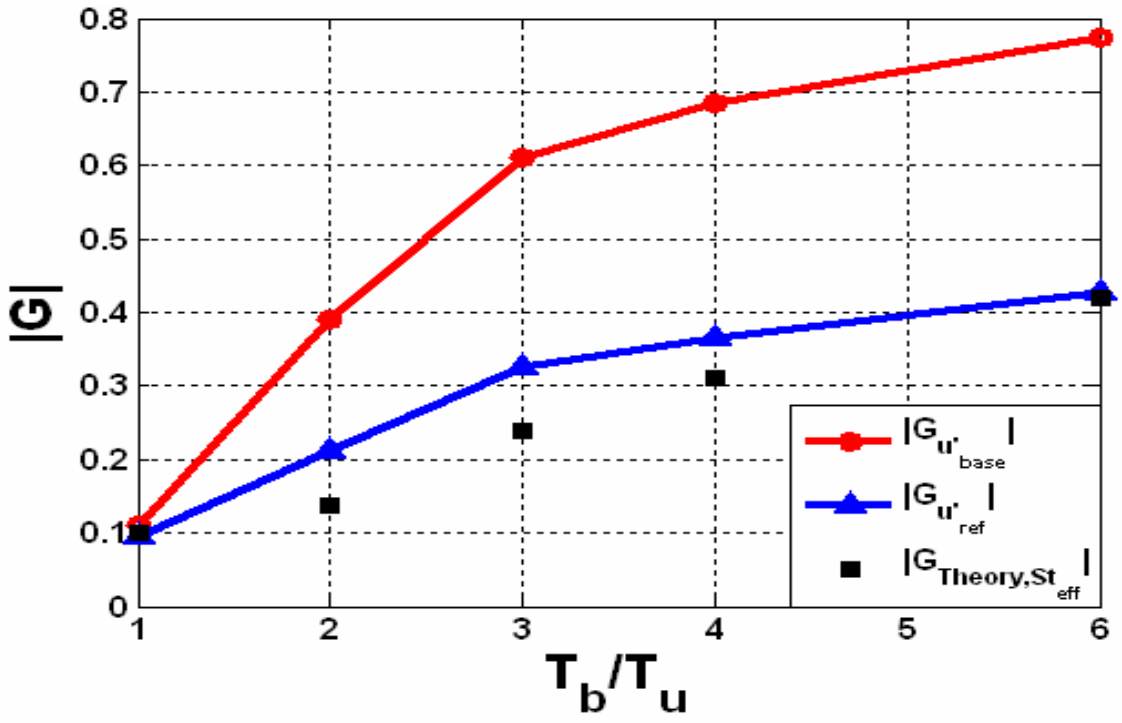

Figure 60 Flame heat release transfer function gain as a function of T_b/T_u. S_{Lo}/u_o=0.5, ε = 0.1, St=5

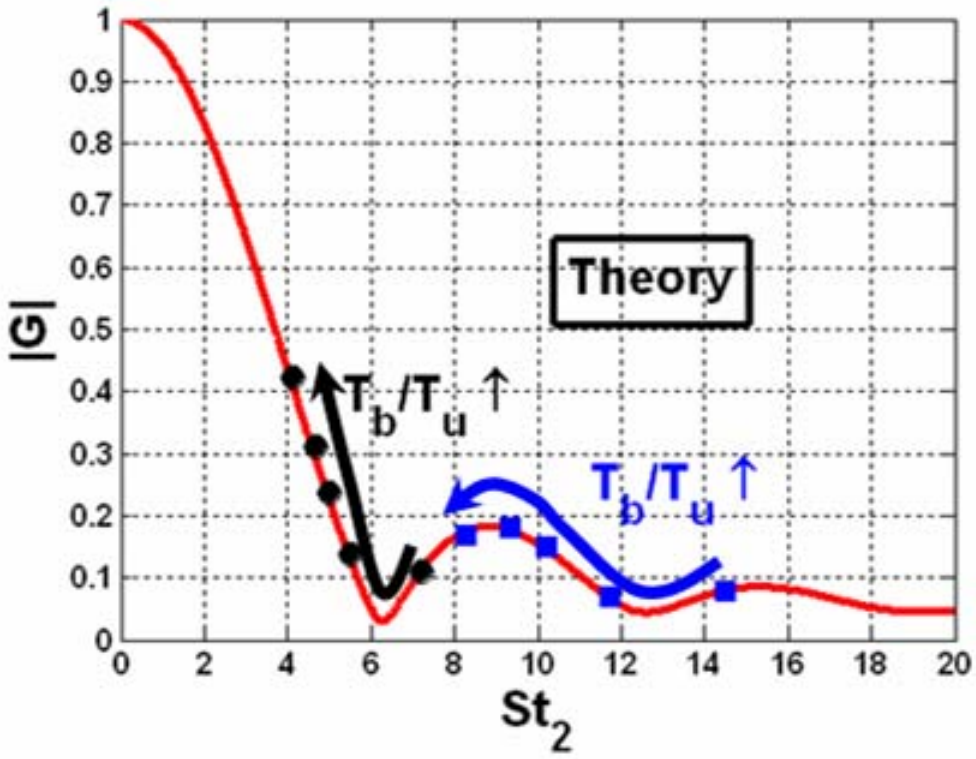

Figure 61 Flame heat release transfer function gain dependence on the reduced Strouhal number, St_2. Black circles correspond to the change in effective Strouhal number as T_b/T_u increases for S_{L_o}/u_o=0.5, ε = 0.1, St=5 while blue squares correspond to S_{L_o}/u_o=0.5, ε = 0.1, St=10.

Similar analysis has been performed for a case wherein the flame is excited at a much higher St=10. Trends similar to the St=5 case can be observed for the gain (see Figure 62) and phase (Figure 63). The gain, based on the effective reference velocity ($G_{u'_{ref}}$), is shown in Figure 64. As observed for the St=5 case (see Figure 60), the gain differential across T_b/T_u reduces substantially in comparison to the case wherein the reference velocity is based on the value at the flame base ($G_{u'_{base}}$). For this case, the effective St_2 changes from 14.5 for $T_b/T_u \rightarrow 1$ to ~8.29 for T_b/T_u=6 (see the movement of the blue squares in Figure 61). Once the gain values from theory are corrected for the effective Strouhal number ($G_{Theory,St_{eff}}$), there is good agreement with the gain ($G_{u'_{ref}}$) based on the effective reference velocity (see Figure 64).

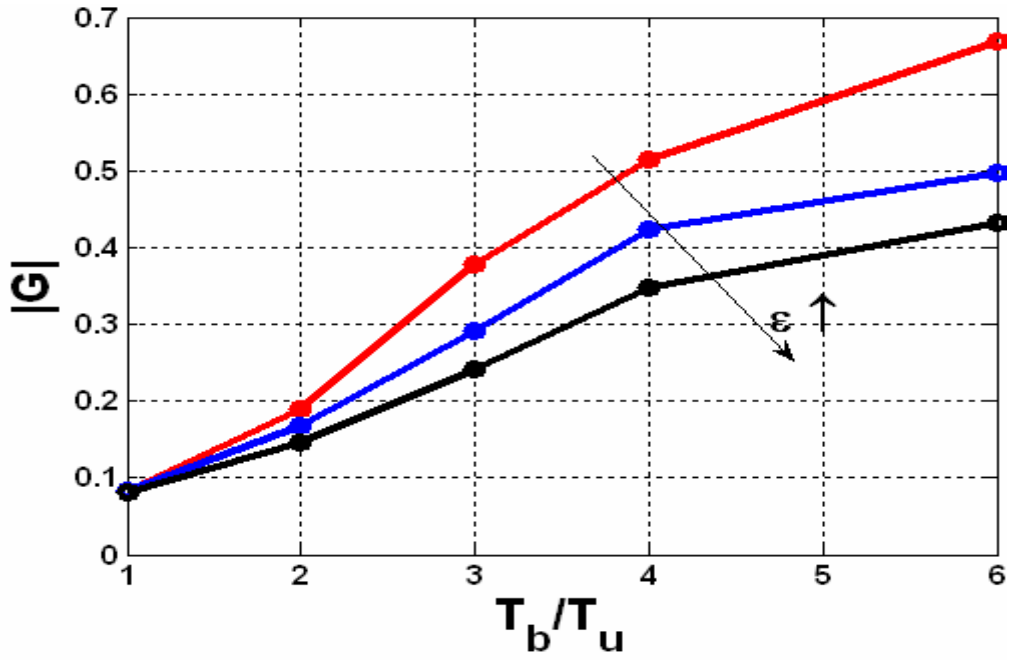

Figure 62 Flame heat release transfer function gain as a function of T_b/T_u for increasing values of excitation amplitude. S_{Lo}/u_o=0.5, ε = 0.1, 0.3, 0.5, St=10

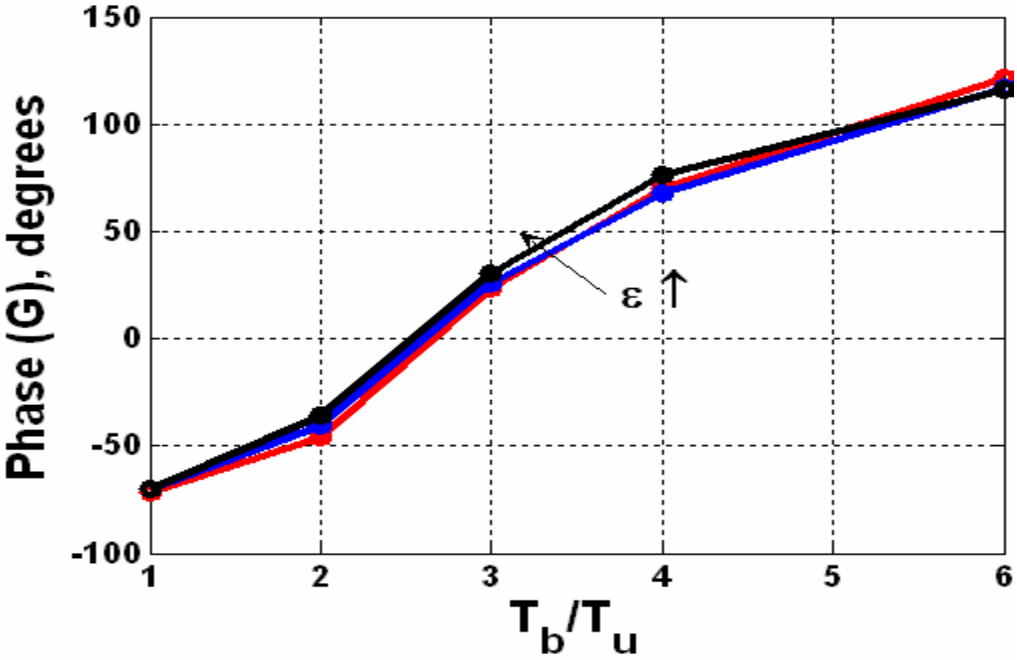

Figure 63 Flame heat release transfer function phase as a function of T_b/T_u for increasing values of excitation amplitude. S_{Lo}/u_o=0.5, ε = 0.1, 0.3, 0.5, St=10

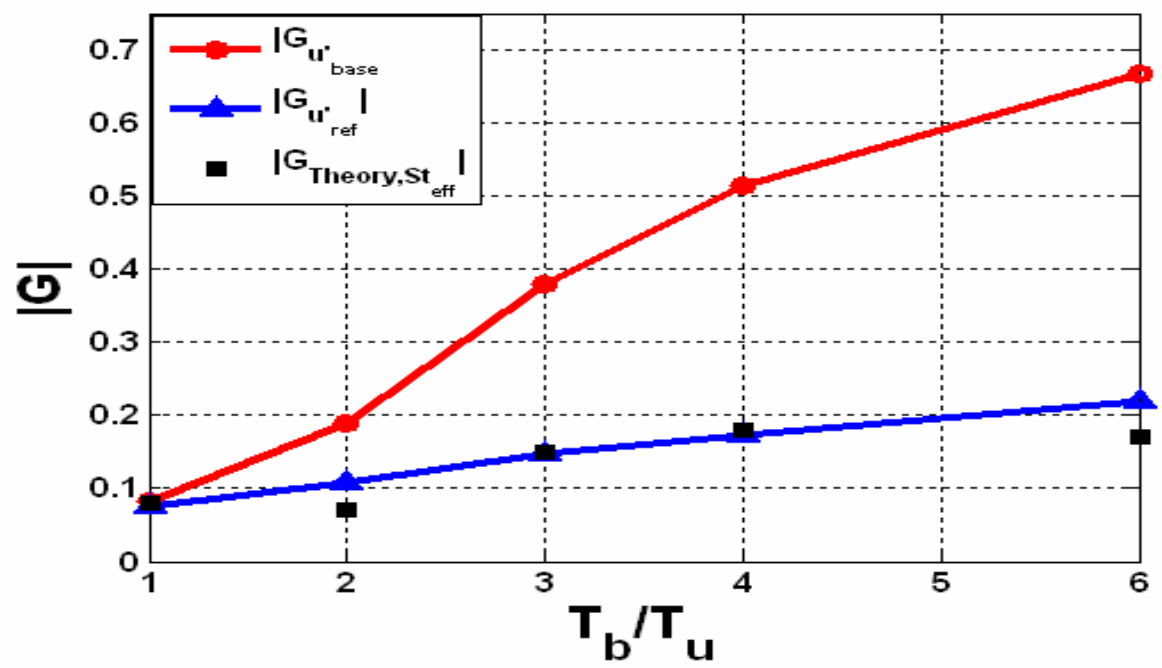

Figure 64 Flame heat release transfer function gain as a function of T_b/T_u. S_{L_o}/u_o=0.5, ε = 0.1, St=10

The current analysis helps in clarifying some of the observations reported by Birbaud *et al.*[29] who studied the effect of confinement by varying the diameter of the duct bounding an axisymmetric wedge flame. In the unconfined situation, the flame behaved as an *amplifier* for a certain range of Strouhal numbers and for higher Strouhal numbers it (i.e. the gain) exhibited a *low pass behavior*. *However, in the confined case, they reported that the gain was approximately constant (close to unity) regardless of the frequency and amplitude of excitation*. In that study, the gain was defined based on the axial velocity fluctuations at the flame base. Even if the flame base excitation velocity is the same for the confined and unconfined configuration, the perturbation velocity magnitude will have a widely different spatial structure. The discussion in the context of Figure 60, Figure 61 and Figure 64 shows that this choice of reference velocity is clearly inadequate for comparing flame responses across different confinement configurations. Birbaud *et al.* [29] *also reported that flame vortex interaction was the primary mechanism controlling*

the flame dynamics in the unconfined configuration. *Based on the differences in the Strouhal number (defined based on the forcing frequency, injector diameter and inlet mean flow velocity) dependence of the transfer function, they concluded that for the confined case flame-wall interaction effects were dominant in comparison to the mechanism of flame-vortex interaction*. The results presented in Figure 61 (also see Eq (129)) have shown that the *effective Strouhal number* (due to acceleration of the flame tangential velocity) in a confined configuration is significantly *lower* than the reference Strouhal number based on the inlet mean velocity. Essentially, the *effective Strouhal number* across the two flame configurations is widely different, making even a qualitative comparison of the flame response difficult. In summary, interpreting the physics from a transfer function based on the flame base velocity fluctuations and Strouhal number defined using the inlet mean velocity may yield physically misleading results.

Next, consider some of the non linear aspects of the heat release response. The flame front oscillation amplitude is substantially higher at the flame tip as can be seen in Figure 65 (which corresponds to a low velocity excitation amplitude of ε=0.1) and is a strong function of T_b/T_u. Since the surface area is equally distributed along the flame in the two-dimensional case (unlike axisymmetric flames), the higher oscillations close to the flame tip have a substantial effect on the heat release response. Moreover, at higher amplitudes, this "pinching" of the flame tip is followed by a fast kinematic burn out contributing to the nonlinearity in the flame response. These features can be observed in Figure 48 wherein the flame tip is substantially elongated for a part of the cycle (see t=0.3τ-0.4τ cases) and is then followed by kinematic destruction of flame area (t=0.5τ-0.6). This fact is also evident in Figure 66 which shows the time history of the instantaneous heat

release fluctuations for ε=0.5. The sharpening of the Q' peak coincides with the kinematic burnout of the flame tip (see t=0.4τ-0.5τ cases in Figure 48). This effect is enhanced at higher frequencies and is considered next.

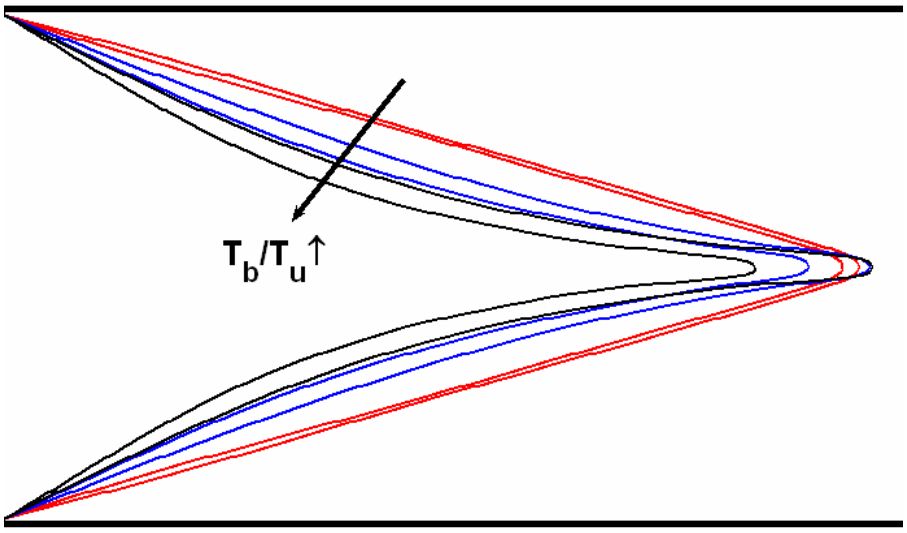

Figure 65 Flame envelope as a function of T_b/T_u. S_{Lo}/u_o=0.5, ε=0.1, St=5, T_b/T_u=1, 3, 6.

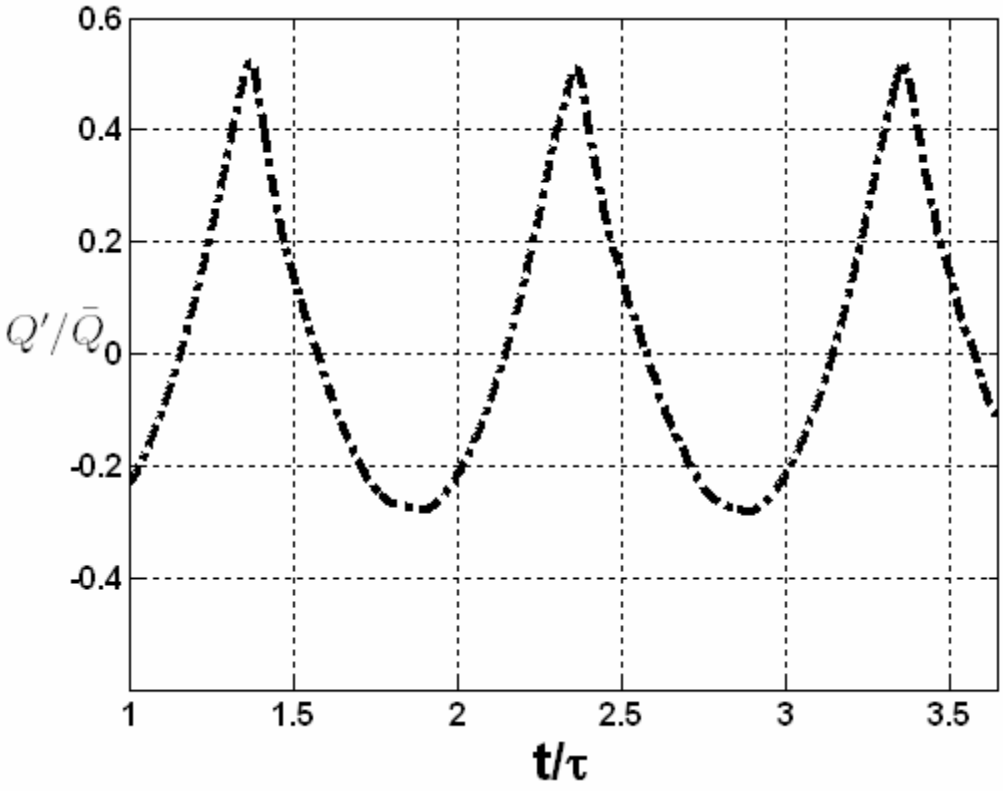

Figure 66 Heat release fluctuations (normalized by the mean) as a function of time (normalized by the acoustic time period, τ). S_{Lo}/u_o=0.5, ε=0.5, St=5, T_b/T_u=6

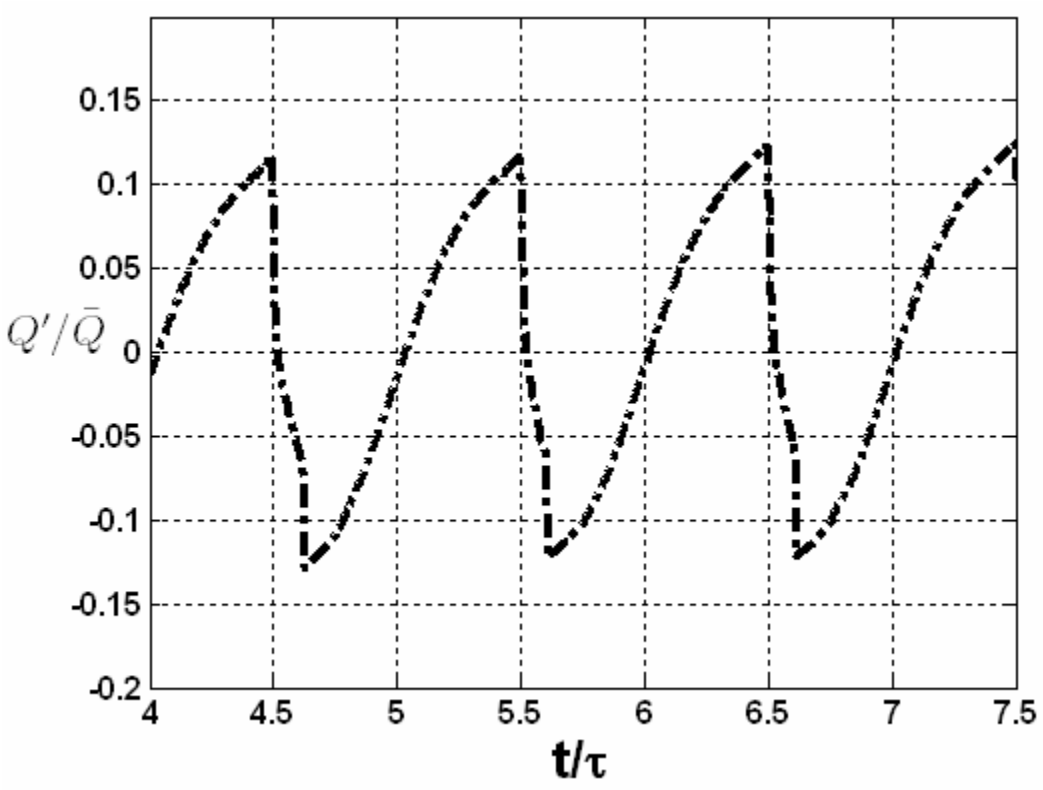

Figure 67 Heat release fluctuations (normalized by the mean) as a function of time (normalized by the acoustic time period, τ). S_{Lo}/u_o=0.25, ε=0.75, St=24.32, T_b/T_u=2

Figure 51 and Figure 52 show the instantaneous flame position along with the (u', v') disturbance field for St=24.32, S_{Lo}/u_o=0.25, T_b/T_u=2 and ε=0.75. Cusp formation, a nonlinear feature of the flame response, can be clearly observed at this amplitude. Moreover, the flame develops pockets (see Figure 51) which is a distinguishing feature of this case in contrast to the lower Strouhal number case considered earlier. These pockets enhance the rate of flame area destruction leading to saturation in the heat release response. This is also captured in the temporal variation of the heat release fluctuations as shown in Figure 67. Note that a sharp drop in the *Q'* level occurs at two discrete time instants in an acoustic cycle. The first event corresponds to the pocket pinch off (between

t=0.4τ-0.5τ in Figure 51) and the second one corresponds to the rapid burnout of the pocket (between t=0.5τ-0.6τ in Figure 51). As discussed earlier in Chapter 4, non-linear features start to appear at much lower amplitudes as the Strouhal number increases. This can also be inferred from Figure 53 and Figure 54 which show pocket formation (and also cusps) for a higher St=73 but a much lower amplitude of ε=0.3.

7.4 Remarks

In the current investigation, a numerical and theoretical analysis of the key factors impacting the heat release response of ducted flames is presented. Confinement effects are shown to have a strong impact on the mean and disturbance field characteristics with increase in T_b/T_u .This study highlights the need for careful consideration of reference velocity and the effective Strouhal number when comparing transfer functions for different T_b/T_u across the flame. On accounting for the strong spatial variation of the disturbance velocity field and the reduction in the wrinkle residence time, good agreement with the constant density theory is obtained. Furthermore, unsteady events like flame pinch off and pocket burnout are shown to be responsible for non linearity in the heat release response.

CHAPTER 8

CONCLUSIONS AND RECOMMENDATIONS

8.1 Conclusions of Present Work

The principal objective of this work was to predict the heat release response of premixed flames and to isolate the key non-dimensional parameters which characterize its linear and nonlinear dynamics. Results were derived from analytical and computational solutions of the nonlinear *G*-equation and compared with available experimental data. It was shown that the linear and nonlinear characteristics of the flame dynamics were controlled by the superposition of two sources of flame disturbances: those originating at the flame anchoring point due to boundary conditions and from flow non-uniformities along the flame. These disturbances do not generally propagate along the flame at the same speed. Consequently, they may either constructively or destructively superpose, so that the overall linear flame response depends upon two Strouhal numbers, St_2 and St_c, related to the amount of time taken for a flow (St_c) and flame front (St_2) disturbance to propagate the flame length, normalized by the acoustic period. Flame stretch effects are characterized b the non-dimensionalized Markstein length, σ_c^*. Flame stretch is found to become important as the disturbance frequency satisfies $\sigma_c^* St_2^2 \sim O(1)$, i.e. $St_2 \sim O\left((\sigma_c^*)^{-1/2}\right)$. Specifically, for disturbance frequencies below this order, stretch effects are small such that the flame acts as an unstretched one. When the disturbance assumes $O(1)$ of this frequency, the transfer function, defined as the ratio of the normalized fluctuation of the heat release rate to that

of velocity, is contributed mostly from fluctuations of the flame surface area, which is now affected by stretch. Finally, as the disturbance frequency increases to that of $St_2 \sim O\left((\sigma_c^*)^{-1}\right)$, i.e. $\sigma_c^* St_2 \sim O(1)$, the direct contribution from the stretch-affected flame speed fluctuation to the transfer function becomes comparable to that of the flame surface area. The present study qualitatively explains the experimentally observed filtering effect in which the flame wrinkles developed at the flame base decay along the flame surface for thermal-diffusively stable mixtures and for large frequencies disturbances.

The nonlinear flame response was shown to be controlled by flame propagation normal to itself, which smoothens out the wrinkles induced by the forcing at an amplitude dependent rate. Because the overall flame response is a *superposition* of the two flame disturbance contributions, the flame's nonlinear response exhibits two qualitatively different behaviors. For parameter values where these disturbances *constructively* interfere, the nonlinear flame response *saturates*. When the flame disturbances *destructively* interfere, the nonlinear transfer function may actually *exceed* its *linear* value before saturating. This result explains Durox *et al's*.[23] experimentally observed variation of the nonlinear flame response with frequency. These results have implications of the type of bifurcations which may be observed in unstable combustors. In situations where the nonlinear gain is always less than one, only supercritical bifurcations will occur and only a single stable limit cycle amplitude is possible. In situations where the gain exceeds, then is less than, the linear gain, multiple stable solutions for the instability amplitude may exist, and sub-critical bifurcations are possible. Such a system will

manifest characteristics such as *hysteresis* and *triggering* (i.e., the destabilization of a linearly stable system by a sufficiently large disturbance).

Most theoretical studies have considered the response of a premixed flame to an imposed disturbance. In reality, the flame alters the character of the disturbance field, so that the problem is coupled. In the final part of this thesis, this coupling was captured by developing a coupled Euler-*G* equation solver to study the dynamics of a ducted flame. It is shown that flame confinement (due to the burner duct) has a strong impact on the mean and unsteady flow field characteristics. Essentially, the no-penetration condition at the wall causes the time-averaged (unburnt) tangential velocity along the flame front to accelerate. This causes the effective residence time of the flame wrinkles to vary with T_b/T_u although the flame has the same frequency of forcing, approach flow velocity and mean flame length. The perturbation velocity field magnitude has a significant spatial dependence and is shown to be much higher than the velocity excitation amplitude at the flame base. Furthermore, a theoretical analysis was developed to understand the effect of spatial non-uniformity of the mean and disturbance flow-field characteristics on the flame response. An explicit analytical expression was also obtained for the effective Strouhal number controlling the flame response. The analysis also gave insight to determine an effective reference velocity for defining heat release transfer functions which can then be consistently compared across T_b/T_u. Heat release transfer function gains showed a strong dependence on T_b/T_u when the flame base excitation amplitude was used as the reference velocity and the Strouhal number was based on the mean inlet velocity. Once the gains across T_b/T_u were corrected for the effective Strouhal number and reference velocity

magnitude, good agreement was obtained with the gain predictions from constant density theory.

8.2 Recommendations for Future Work

This thesis provides a strong theoretical foundation for understanding the linear and nonlinear dynamics of laminar premixed flames subjected to harmonic velocity disturbances. In terms of future work, this analysis should be extended to turbulent flames in order to determine if there are any qualitative/quantitative similarities/differences in the flame response. The nonlinear flame response should be analyzed in cases where the flame is simultaneously being disturbed by deterministic, harmonic fluctuations as well as random fluctuations. The latter fluctuations simulate the impact of background turbulent fluctuations. As such, the analysis can be used to compare the nonlinear dynamics of laminar and turbulent flames.

In practical gas turbine combustors, apart from velocity disturbances, equivalence ratio oscillations are also known to be an important mechanism responsible for combustion instabilities. Currently, there is a lack of theory for understanding the nonlinear response of flames in the presence of equivalence ratio fluctuations. This understanding is essential to predict the limit cycle amplitude as (depending on the operating conditions) one or both of these mechanisms may be controlling its saturation characteristics.

In addition, a key issue which remains to be investigated is whether a conical or wedge flame can exhibit oscillations in the sinuous or varicose mode. Due to the acceleration of the products in a ducted conical/wedge flame, the velocity profile resembles that of a wake/jet respectively. An interesting question is whether this profile is

stable when subjected to infinitesimal/high amplitude disturbances. A combined theoretical and numerical analysis is required to capture the associated flame dynamics.

Finally, the impact of the hydrodynamic instability on the flame dynamics requires further investigation. In the current simulations, the residence time of the wrinkles was found to be much shorter than the characteristic time of the instability growth. Simulations for high aspect ratio (open) flames (having a longer wrinkle residence time) may bring out the impact of the instability on the propagating wrinkles and the associated flame response characteristics.

APPENDIX A

The governing equation for the flame dynamics, in a reference frame attached to the mean flame shape (see Figure 6), is given by:

$$\frac{\partial \xi}{\partial t} + U_o \frac{\partial \xi}{\partial X} = U'(X,t) \tag{133}$$

Differentiating w.r.t X we get

$$\frac{\partial \xi_X}{\partial t} + U_o \frac{\partial \xi_X}{\partial X} = \frac{\partial U'(X,t)}{\partial X} \tag{134}$$

Denote:

$$\begin{aligned} \eta &= \xi_X \\ f(X,t) &= \frac{\partial U'(X,t)}{\partial X} \end{aligned} \tag{135}$$

Then, Eq (134) can be rewritten as:

$$\frac{\partial \eta}{\partial t} + U_o \frac{\partial \eta}{\partial X} = f(X,t) \tag{136}$$

The general solution of the above equation is given by:

$$\eta = \frac{1}{U_o} \int_0^X f\left(x', t - \frac{X - x'}{U_o}\right) dx' + \Phi(X - Uo\, t) \tag{137}$$

The homogeneous solution can be evaluated using the boundary condition @X=0 (i.e. $\frac{\partial \xi}{\partial t} = U'_{base}(t)$) and Eq. (133), which yields:

$$\left.\frac{\partial \xi}{\partial X}\right|_{X=0} = \eta|_{X=0} = \frac{U'(X=0,t) - U'_{base}(t)}{U_o} \tag{138}$$

Using Eq. (138) in Eq. (137) we get,

$$\Phi\left(-Uo\,t\right)=\frac{U'\left(X=0,t\right)-U'_{base}\left(t\right)}{U_o}$$
$$\Rightarrow \Phi\left(X-Uo\,t\right)=\frac{U'\left(X=0,t-X/Uo\right)-U'_{base}\left(t-X/Uo\right)}{U_o} \tag{139}$$

Using Eq. (139), the solution can be rewritten as:

$$\eta=\frac{1}{U_o}\int_0^X f\left(x',t-\frac{X-x'}{U_o}\right)dx'+\frac{U'\left(X=0,t-X/Uo\right)-U'_{base}\left(t-X/Uo\right)}{U_o} \tag{140}$$

Using Eq. (140) and Eq. (135) the final solution can be expressed as:

$$\frac{\partial\xi(X,t)}{\partial X}=\underbrace{\frac{1}{U_o}\int_0^X\left(\frac{\partial U'(X,t)}{\partial X}\right)_{X\to x',t\to\left(t-\frac{X-x'}{U_o}\right)}dx'}_{Flow\ non-uniformity\left(particular\ solution\right)}+\underbrace{\frac{1}{U_o}\left(U'(X=0,t-\frac{X}{U_o})-U'_{base}\left(t-X/Uo\right)\right)}_{Boundary\ condition\left(homogeneous\ solution\right)}$$

APPENDIX B

The governing equation for the flame dynamics (see Eq (19) and Figure 12) is given by:

$$\frac{\partial \zeta}{\partial t} + S_L \sqrt{1+\beta^2 \zeta_r^2} = u(\zeta,t) - \beta\, v(\zeta,t)\zeta_r \quad (141)$$

Decomposing the variables in Eq (141) into mean and fluctuating parts and retaining the linear terms yields:

$$\overline{u} - \beta \overline{v} \overline{\zeta}_r - S_L(r)\sqrt{1+\beta^2 \overline{\zeta}_r^2} = 0 \quad (142)$$

$$\zeta_t' = u' - \beta \overline{v} \zeta_r' - \beta v' \overline{\zeta}_r - \frac{\beta^2 S_L(r) \overline{\zeta}_r \zeta_r'}{\sqrt{1+\beta^2 \overline{\zeta}_r^2}} \quad (143)$$

In Eqs (142) and (143), (u,v) has been non-dimensionalized using the *inlet* mean flow velocity (U_o) , ζ by mean flame length L_f and r by the burner radius R. The flame aspect ratio, L_f/R, is denoted as β. At the mean flame front, the fluctuating normal velocity and the mean tangential velocity are given by:

$$u_n' = \frac{u' - \beta v' \overline{\xi}_r}{\sqrt{1+\beta^2 \overline{\xi}_r^{\,2}}} \quad (144)$$

$$\overline{u}_t = \frac{-\overline{u}\beta \overline{\xi}_r - \overline{v}}{\sqrt{1+\beta^2 \overline{\xi}_r^{\,2}}} \quad (145)$$

where the subscripts n,t denote normal and tangential respectively. Equation (143) can be rewritten in terms of the fluctuating normal velocity and mean tangential velocity (using Eqs (142), (144) and (145)) as:

$$\zeta_t' = u_n' \sqrt{1+\beta^2 \overline{\zeta}_r^2} + \frac{\beta \overline{u}_t}{\sqrt{1+\beta^2 \overline{\zeta}_r^2}} \zeta_r' \quad (146)$$

Assuming harmonic oscillations, (i.e. $\zeta'(r,t)=\hat{\zeta}(r)e^{-iSt\,t}$, $u_n'(r,t)=\hat{u}_n(r)e^{-iSt\,t}$)

yields:

$$iSt\;\hat{\zeta}+\hat{u}_n\sqrt{1+\beta^2\overline{\zeta}_r^2}+\frac{\beta\overline{u}_t}{\sqrt{1+\beta^2\overline{\zeta}_r^2}}\hat{\zeta}_r=0 \qquad (147)$$

where *St* is the non-dimensional frequency.

Solving Eq (147) and applying the flame anchoring boundary condition at $r=1$ yields:

$$\hat{\zeta}(r)=e^{\int_1^r -\frac{iSt}{F(\varphi)}\,d\varphi}\int_r^1\left(-e^{\int_1^\theta \frac{iSt}{F(\varphi)}\,d\varphi}\,\frac{P(\theta)\hat{u}_n(\theta)}{F(\theta)}\right)d\theta \qquad (148)$$

where
$$F(r)=\frac{\beta\overline{u}_t}{\sqrt{1+\beta^2\overline{\zeta}_r^2}}$$
$$P(r)=\sqrt{1+\beta^2\overline{\zeta}_r^2} \qquad (149)$$

Using Eq (148), the fluctuating flame area (for a two-dimensional flame) can be expressed as:

$$\frac{\hat{A}}{A_o}=\int_0^1\left(\frac{iSt\;\beta^2\overline{\zeta}_r}{\sqrt{1+\beta^2}F(r)P(r)}e^{\int_1^r -\frac{iSt}{F(\varphi)}\,d\varphi}\int_1^r\left(e^{\int_1^\theta \frac{iSt}{F(\varphi)}\,d\varphi}\,\frac{P(\theta)\hat{u}_n(\theta)}{F(\theta)}\right)d\theta-\frac{\beta^2\hat{u}_n(r)\overline{\zeta}_r}{\sqrt{1+\beta^2}F(r)}\right)dr \qquad (150)$$

Define:

$$I_1=\int_0^1\left(\frac{iSt\;\beta^2\overline{\zeta}_r}{\sqrt{1+\beta^2}F(r)P(r)}e^{-iStH(r)}\int_1^r\left(e^{iStH(\theta)}\,\frac{P(\theta)\hat{u}_n(\theta)}{F(\theta)}\right)d\theta\right)dr \qquad (151)$$

$$I_2=\int_0^1\left(-\frac{\beta^2\hat{u}_n(r)\overline{\zeta}_r}{\sqrt{1+\beta^2}F(r)}\right)dr \qquad (152)$$

$$H(\theta)=\int_1^{\theta}\frac{1}{F(\varphi)}\,d\varphi \qquad (153)$$

Equation (151) can then be rewritten as:

$$I_1=\int_0^1\left(\frac{-\beta^2}{\sqrt{1+\beta^2}}M(r)\,N(r)\right)dr \qquad (154)$$

where

$$M(r)=\frac{-iSte^{-iStH(r)}}{F(r)}$$

$$N(r)=\frac{\bar{\zeta}_r}{P(r)}\int_1^r\left(e^{iStH(\theta)}\frac{P(\theta)\hat{u}_n(\theta)}{F(\theta)}\right)d\theta \qquad (155)$$

Note that:

$$\int M(r)\,dr=e^{-iStH(r)} \qquad (156)$$

Integrating Eq.(154) by parts, yields:

$$\begin{aligned}
I_1&=\int_0^1\left(\frac{-\beta^2}{\sqrt{1+\beta^2}}M(r)\,N(r)\right)dr\\
&=\left(\frac{-\beta^2}{\sqrt{1+\beta^2}}\int M(r)dr\;N(r)\right)\Bigg|_0^1-\int_0^1\left(\frac{-\beta^2}{\sqrt{1+\beta^2}}\int M(r)dr\;N'(r)\right)dr\\
&=\frac{-\beta^2}{\sqrt{1+\beta^2}}e^{-iStH(0)}\frac{\bar{\zeta}_r(0)}{G(0)}\int_0^1\left(e^{iStH(r)}\frac{P(r)\hat{u}_n(r)}{F(r)}\right)dr\\
&\quad-\int_0^1\left(\frac{-\beta^2}{\sqrt{1+\beta^2}}e^{-iStH(r)}\;N'(r)\right)dr
\end{aligned} \qquad (157)$$

Also,

$$N'(r)=\frac{\bar{\zeta}_r}{P(r)}\left(e^{iStH(r)}\frac{P(r)\hat{u}_n(r)}{F(r)}\right)+\left(\frac{\bar{\zeta}_r}{P(r)}\right)_r\int_1^r\left(e^{iStH(\theta)}\frac{P(\theta)\hat{u}_n(\theta)}{F(\theta)}\right)d\theta \qquad (158)$$

Using (158), Eq. (157) can be simplified to:

$$I_1 = \frac{-\beta^2}{\sqrt{1+\beta^2}} e^{-iStH(0)} \frac{\bar{\zeta}_r(0)}{P(0)} \int_0^1 \left(e^{iStH(r)} \frac{P(r)\hat{u}_n(r)}{F(r)} \right) dr$$
$$+ \frac{\beta^2}{\sqrt{1+\beta^2}} \int_0^1 \bar{\zeta}_r \left(\frac{\hat{u}_n(r)}{F(r)} \right) dr \qquad (159)$$
$$+ \frac{\beta^2}{\sqrt{1+\beta^2}} \int_0^1 \left(e^{-iStH(r)} \left(\frac{\bar{\zeta}_r}{P(r)} \right)_r \int_1^r \left(e^{iStH(\theta)} \frac{P(\theta)\hat{u}_n(\theta)}{F(\theta)} \right) d\theta \right) dr$$

Using Eq (159), (152) in Eq. (150)yields:

$$\frac{\hat{A}}{A_o} = \frac{\beta^2}{\sqrt{1+\beta^2}} \left(e^{-iStH(0)} \frac{\bar{\zeta}_r(0)}{P(0)} \chi(0) + \int_0^1 \left(e^{-iStH(r)} \left(\frac{\bar{\zeta}_r}{P(r)} \right)_r \chi(r) \right) dr \right) \qquad (160)$$
$$\chi(r) = \int_1^r \left(e^{iStH(\theta)} \frac{P(\theta)\hat{u}_n(\theta)}{F(\theta)} \right) d\theta$$

Finally, the expression for the area fluctuations can be written in the following form:

$$\boxed{\frac{\hat{A}}{A_o} = \frac{\beta^2}{\sqrt{1+\beta^2}} e^{-iStH(0)} \frac{\bar{\zeta}_r(0)}{P(0)} \chi(0) + \frac{\beta}{\sqrt{1+\beta^2}} \int_0^1 \left(e^{-iStH(r)} \kappa(r) \chi(r) \right) dr} \qquad (161)$$

where

$$\boxed{\begin{aligned} \chi(r) &= \int_1^r \left(e^{iStH(\theta)} \frac{P(\theta)\hat{u}_n(\theta)}{F(\theta)} \right) d\theta \\ F(r) &= \frac{\beta \bar{u}_t}{\sqrt{1+\beta^2 \bar{\zeta}_r^2}} \\ P(r) &= \sqrt{1+\beta^2 \bar{\zeta}_r^2} \\ \kappa(r) &= \beta \left(\frac{\bar{\zeta}_r}{P(r)} \right)_r = \frac{\beta \bar{\zeta}_{rr}}{\left(1+\beta^2 \bar{\zeta}_r^2\right)^{3/2}} \\ H(r) &= \int_1^r \frac{1}{F(r)} dr \end{aligned}} \qquad (162)$$

The characteristic frequency is equal to

$$-StH(0) = St\int_0^1 \frac{1}{F(r)}\,dr = St\int_0^1 \frac{\sqrt{1+\beta^2\bar{\zeta}_r^2}}{\beta\bar{u}_t}\,dr \quad (163)$$

For a flame in a uniform axial mean flow, (i.e. $v = 0, \bar{\zeta}_r = -1$), Eq. (163) reduces to

$$St\int_0^1 \frac{\sqrt{1+\beta^2}}{\beta}\frac{\sqrt{1+\beta^2}}{\beta}\,dr = St_2$$

Also for this case, Eq. (160) reduces to:

$$\frac{\hat{A}}{A_o} = \int_0^1 \left(\sqrt{1+\beta^2}\,e^{iSt_2 r}\,\hat{u}_n(r)\right)dr \quad (164)$$

If the disturbance field is purely axial (i.e. $v' = 0$) with magnitude ε, Eq. (164) reduces to:

$$\frac{\hat{A}}{A_o} = \varepsilon\int_0^1 e^{iSt_2 r}\,dr = \varepsilon\frac{e^{iSt_2}-1}{iSt_2}$$

Hence, the transfer function for this particular case can be expressed as:

$$G_{2d,linear} = \frac{e^{iSt_2}-1}{iSt_2}$$

APPENDIX C

The solutions for the flame position are:

$$\zeta_o(r,t) = 1 - r$$

$$\zeta_1(r,t) = \left(\frac{2Sin\left[\left(\frac{St(K\alpha - 1)(1-r)}{2\alpha} \right) \right]}{(K\alpha - 1)\ St} \right) Cos\left[St \left\{ \frac{(K\alpha + 1)(r-1)}{2\alpha} + t \right\} \right]$$

$$\begin{aligned}
\zeta_2(r,t) = & \left(\frac{r + \alpha - r\alpha - 1}{4(K\alpha - 1)^2 \alpha^2} \right) Cos\left[2\ St \left\{ \frac{r - 1 + \alpha t}{\alpha} \right\} \right] \\
& + \left(\frac{6K - 4K\alpha - 3K^2\alpha + K^2\alpha^2}{8\ St(K\alpha - 1)^3} \right) Sin\left[2\ St \left\{ \frac{r - 1 + \alpha t}{\alpha} \right\} \right] \\
& + \left(\frac{K\alpha(K-1)}{2(K\alpha - 1)^3\ St} \right) Sin\left[St\ \frac{(1-r)(K\alpha - 1)}{\alpha} \right] \\
& + \left(\frac{2K - K^2\alpha - K^2\alpha^2}{8\ St(K\alpha - 1)^3} \right) Sin\left(2\ St(K(r-1) + t) \right) \\
& + \left(\frac{-2K + K\alpha + K^2\alpha}{2(K\alpha - 1)^3\ St} \right) Sin\left[St \left\{ \frac{(K\alpha + 1)(r-1) + 2\alpha t}{\alpha} \right\} \right] \\
& + \left(\frac{(r-1)(-1 + \alpha + 2K\alpha - 3K^2\alpha^2 + K^2\alpha^3)}{4\alpha^2(K\alpha - 1)^2} \right)
\end{aligned}$$

$$\begin{aligned}
\zeta_3(r,t) = & \left(\frac{(r-1)(1-\alpha)(-3 + 13K\alpha - 4K\alpha^2 - 13K^2\alpha^2 - 3K^2\alpha^3 + 10K^3\alpha^3)}{8(K\alpha - 1)^4\alpha^3} \right) \\
& \times Cos\left[St \left\{ \frac{r - 1 + \alpha t}{\alpha} \right\} \right]
\end{aligned}$$

$$-\left(\frac{\begin{array}{l}2(r-1)^2(1-\alpha)^2(K\alpha-1)^2St^2+K\alpha^4(4-4\alpha-8K-5K\alpha\\+9K\alpha^2+27K^2\alpha-15K^2\alpha^2-4K^2\alpha^3-18K^3\alpha^2+14K^3\alpha^3)\end{array}}{16(K\alpha-1)^5\alpha^4\,St}\right)\times Sin\left[St\left\{\frac{r-1+\alpha t}{\alpha}\right\}\right]$$

$$-\left(\frac{K(r-1)(-1+\alpha+2\alpha K-3K^2\alpha^2+K^2\alpha^3)}{4\alpha^2(K\alpha-1)^3}\right)Cos\left[St(K(r-1)+t)\right]$$

$$-\left(\frac{K(\alpha-1)(-8+16K-21\alpha K^2-2K^2\alpha^2+15K^3\alpha^2)}{16(K\alpha-1)^5St}\right)Sin\left[St(K(r-1)+t)\right]$$

$$+\left(\frac{K(r-1)(1-\alpha)(1-2\alpha+K\alpha)}{8\alpha^2(K\alpha-1)^4}\right)Cos\left[St\,\frac{(1-r)(K\alpha-2)+\alpha t}{\alpha}\right]$$

$$+\left(\frac{K(\alpha-1)(4-8K+8K\alpha-3\alpha K^2-2K^2\alpha^2+K^3\alpha^2)}{16(K\alpha-1)^5St}\right)Sin\left[St\,\frac{(1-r)(K\alpha-2)+\alpha t}{\alpha}\right]$$

$$+\left(\frac{K^2\alpha(5-\alpha-3K-5K\alpha+2K^2\alpha+2K^2\alpha^2)}{16(K\alpha-1)^5St}\right)Sin\left[St\,\frac{(1-r)(2K\alpha-1)+\alpha t}{\alpha}\right]$$

$$+\left(\frac{(1-\alpha)(r-1)(-1+7K\alpha-4K\alpha^2-3K^2\alpha^2+K^2\alpha^3)}{8\,\alpha^3(K\alpha-1)^4}\right)Cos\left[3St\left\{\frac{r-1+\alpha t}{\alpha}\right\}\right]$$

$$+\left(\frac{\begin{array}{l}K\alpha^4(-12+12\alpha+52K-57K\alpha+9K\alpha^2-45K^2\alpha+41K^2\alpha^2-4K^2\alpha^3\\+10K^3\alpha^2-6K^3\alpha^3)-6(r-1)^2(1-\alpha)^2(K\alpha-1)^2St^2\end{array}}{48(K\alpha-1)^5\alpha^4\,St}\right)$$

$$\times Sin\left[3St\left\{\frac{r-1+\alpha t}{\alpha}\right\}\right]+\left(\frac{K(r-1)(1-\alpha)(-3+2\alpha+K\alpha)}{8\alpha^2(K\alpha-1)^4}\right)Cos\left[St\,\frac{(1-r)(K\alpha+2)-3\alpha t}{\alpha}\right]$$

$$+\left(\frac{K(\alpha-1)(-4+4\alpha+28K-32\alpha K+8K\alpha^2-23K^2\alpha+17K^2\alpha^2-2K^2\alpha^3+5K^3\alpha^2-K^3\alpha^3)}{16(K\alpha-1)^5St}\right)$$

$$\times Sin\left[St\,\frac{(1-r)(K\alpha+2)-3\alpha t}{\alpha}\right]-\left(\frac{K^2(4-3\alpha K-7\alpha^2K+2K\alpha^3+K^2\alpha^2+3K^2\alpha^3)}{48(K\alpha-1)^5St}\right)$$

$$\times Sin\left[3St(K(r-1)+t)\right]+\left(\frac{K^2(12-13\alpha+5\alpha^2-9K\alpha+\alpha^2K+2\alpha^2K^2+2\alpha^3K^2)}{16(K\alpha-1)^5St}\right)$$

$$\times Sin\left[St\,\frac{(r-1)(2K\alpha+1)+3\alpha t}{\alpha}\right]$$

The Mathematica code for the third order perturbation analysis is given below:

```
ClearAll;

Si = 1 - r + e * Si1[t, r] + e^2 * Si2[t, r] + e^3 * Si3[t, r]

Sit = D[Si, t]

V = 1 + e * Cos[St * K * Si - St * t]

Series[Sit + Sqrt[1 - a + a * D[Si, r]^2] - V, {e, 0, 3}]

FullSimplify[DSolve[D[Z1[t, r], t] - a * D[Z1[t, r], r] - Cos[K St - K r St - St t] == 0, Z1[t, r], {t, r}]]

v1 = Z1[t, r];

v2 = v1 /. {r → 1}

Solve[v2 == 0, C[1][1 + a t]]

v4 = v3 /. {t -> (t - 1) / a}

V4 = v4 /. {t → r + a * t}

Si1Soln = FullSimplify[v1]

FullSimplify[DSolve[D[Z2[t, r], t] - a * D[Z2[t, r], r]
    + K St * Si1Soln * Sin[K St - K r St - St t]
    + 1/2 a * (1 - a) * D[Si1Soln, r]^2 == 0, Z2[t, r], {t, r}]]

Si2Soln = FullSimplify[Z2[t, r]]

DSolve[D[Z3[t, r], t] - a * D[Z3[t, r], r] + v8 == 0, Z3[t, r], {t, r}]

v10 = v9 /. {r → 1};

Solve[v10 == 0, C[1][1 + a t]]

v12 = v11 /. {t -> (t - 1) / a};

v13 = v12 /. {t -> r + a * t};

Si3Soln = v9 /. {C[1][r + a t] → v13};

Si3Soln = Simplify[Si3Soln];

SiTot = Simplify[1 - r + Si1Soln * e + Si2Soln * e^2 + Si3Soln * e^3];

Series[2 * r * Sqrt[1 - a + a * D[SiTot, r]^2], {e, 0, 3}]

ConeArea = Integrate[v14, {r, 0, 1}]
```

```
CTF = (Integrate[2 * ConeArea * Exp[I * St * t], {t, to, to + 2 * Pi / St}]) / (e * 2 * Pi / St)

v10 = Simplify[CTF]

v11 = Simplify[TrigToExp[v10]]

v12 = Collect[v11, e^-1, Simplify]

v14 = Collect[v13, e^-1, Simplify]

v15 = v14 /. {St → w * a}

lim1 = Simplify[Limit[v15, e → 0]]

lim2 = Collect[Simplify[Limit[v15, K → 0]], e, FullSimplify]

lim5 = Simplify[Limit[v15, w → 0]]

lim5 = FullSimplify[v15]

Collect[lim5, e, Simplify]
```

APPENDIX D

The transfer function coefficients referred to in Eq. (54) are:

$$\tilde{A}_{c,\omega_o} = -8\ (\alpha-1)^2 + 4K\alpha\{2 - i(\alpha-1)St_2\} - 2K^2\alpha^2\left\{10 + \alpha + \alpha^2 + i8St_2 - i4\alpha St_2\right\}$$
$$+K^3\alpha^3\{\ 27 - \alpha(3 + i8St_2) + i32St_2\} + K^4\alpha^4\{-17 + 9\alpha - i32St_2 + i8St_2\alpha\} - i4K^5\alpha^5 St_2\{\alpha - 3\ \}$$

$$\tilde{B}_{c,\omega_o} = 2(\alpha-1)\left\{6\alpha + iSt_2 - i4\alpha St - (\alpha-1)St^2\right\} + 4K\alpha(\alpha-1)\left\{-10 + i4St_2 - St_2{}^2 + \alpha(i + St_2)^2\right\}$$
$$+K^2\alpha^2\left\{-76 + 81\alpha - \alpha^2 - i44(\alpha-1)St_2 - i6(\alpha-1)St_2\alpha - 2St_2{}^2(\alpha-1)^2\right\}$$
$$+K^3\alpha^3\left\{-8\alpha^2 + i(\alpha-1)(i49 + 46St_2 + 6\alpha St_2)\right\} + 2K^4\alpha^4\{-7 + 9\alpha - i10St_2(\alpha-1)\}$$

$$\tilde{C}_{c,\omega_o} = \{8(iSt_2 - 2)\} + 4K\{5 - \alpha - i3St_2(1+\alpha)\} + 2K^2\alpha\{2 + 6\alpha + i11St_2 + i2St_2\alpha\}$$
$$-2K^3\alpha^2\{11 + \alpha + i6St_2\} + K^4\alpha^3\{9 + i2St_2\} - K^5\alpha^4$$

$$\tilde{D}_{c,\omega_o} = 4 - \alpha + \alpha^2 - K\alpha(13 + 3\alpha) + 2K^2\alpha^2(9 + \alpha) - 8K^3\alpha^3$$

$$\tilde{E}_{c,\omega_o} = 16(\alpha-1)^2 + 4K\alpha\left\{-6 + 10\alpha - 8\alpha^2 + iSt_2(3 - 5\alpha + 2\alpha^2)\right\}$$
$$+2K^2\alpha^2\left\{2(-15 + 31\alpha - 2\alpha^2) - iSt_2(19 - 28\alpha + 9\alpha^2)\right\}$$
$$+3K^3\alpha^3\left\{29 - 44\alpha - 5\alpha^2 + i2St_2(12 - 13\alpha + \alpha^2)\right\}$$
$$+K^4\alpha^4\left\{-59 + 77\alpha + 8\alpha^2 + i2St_2\{-9 + 8\alpha + \alpha^2)\right\} + 2K^5\alpha^5\{7 - 9\alpha - i2St_2(\alpha-1)\}$$

The transfer function coefficients referred to in Eq. (55) are

$$\tilde{A}_{w,\omega_o} = 8(\alpha-1)^2 - i8K\alpha\left\{-i+(\alpha-1)^2 St_2\right\} + 2K^2\alpha^2\left\{10+\alpha+\alpha^2+i4St_2+2(\alpha-1)St_2{}^2\right\}$$
$$+K^3\alpha^3\left\{-27-i20St_2-i2St_2\alpha^2+16\ St_2{}^2+\ \alpha(3-i2St_2-8St_2{}^2)\right\}$$
$$+K^4\alpha^4\left\{17+i27St_2-32St_2{}^2+\alpha(-9-i3St_2+8St_2{}^2)\right\} - K^5\alpha^5 St_2\left\{i17-32St_2+\alpha(8St_2-i9)\right\}$$
$$+4\ K^6\alpha^6(\alpha-3)St_2{}^2$$

$$\tilde{B}_{w,\omega_o} = 2(\alpha-1)\left\{3\alpha St^2 - 6\alpha(1-iSt_2) - i(\alpha-1)St^3 \quad\right\}$$
$$+i4K\alpha(\alpha-1)\left\{(\alpha+10)(1-iSt_2) - (5+\alpha)St_2{}^2 + i(\alpha-1)St_2{}^3)\right\}$$
$$+K^2\alpha^2\left\{(1-iSt_2)(76-81\alpha+\alpha^2) + 2St_2{}^2(\alpha-1)(23+2\alpha+iSt_2-i\alpha St_2)\right\}$$
$$+K^3\alpha^3\left\{8\alpha^2(1-iSt_2) - (\alpha-1)(-49+i49St_2+46St_2{}^2+6\alpha St_2{}^2)\right\}$$

$$\tilde{C}_{w,\omega_o} = \left\{-16(i+St_2)^2\right\} + 4K\left\{-5+\alpha+i10St_2+\ i2\alpha St_2\ +\ 6St_2{}^2+8\alpha St_2{}^2\right\}$$
$$-4K^2\alpha\left\{1+i3St_2+14St_2{}^2+\alpha(3-i7St_2+5St_2{}^2)\right\}$$
$$+2K^3\alpha^2\left\{11+\alpha-i24St_2-i8\alpha St_2+23St_2{}^2+2\alpha St_2{}^2\right\}$$
$$+K^4\alpha^3\left\{-9+i2(20+\alpha)St_2-16St_2{}^2\right\}$$
$$+K^5\alpha^4\left\{1-i11St_2+2St_2{}^2\right\} + iK^6\alpha^5 St_2$$

The transfer function expressions in the limit of $K\alpha\to 1$ are given by:

$$\lim_{K\alpha\to 1} G_{c,\omega_o} = \frac{2\left(-1+e^{i\,St_2}(1-iSt_2)\right)}{St_2{}^2} + \varepsilon^2\left(\frac{26-59\alpha+31\alpha^2+iSt_2(\alpha-1)(5\alpha-4)}{2St_2^2\alpha^2} + \right.$$
$$\left. e^{i\,St_2}\frac{\left(\begin{array}{l}-30(26-59\alpha+31\alpha^2)+60iSt_2(11-25\alpha+13\alpha^2)\\ +15St_2^2(3\alpha-2)(7\alpha-9)+5iSt_2^3\left(13-31\alpha+16\alpha^2\right)-(15St_2^4-2iSt_2^5)(\alpha-1)^2\end{array}\right)}{60St_2^2\alpha^2}\right)$$

$$\lim_{K\alpha\to 1} G_{w,\omega_o} = \frac{2\left(1+e^{i\,St_2}\left(-1+iSt_2+St_2^2\right)\right)}{{St_2}^2} + \varepsilon^2\left(\frac{-26+59\alpha-31\alpha^2}{2St_2^2\alpha^2} + e^{i\,St_2}\,\frac{\left(\begin{array}{l} 30(1-iSt_2-\frac{St_2^2}{2})(26-59\alpha+31\alpha^2)+5iSt_2^3\left(28-61\alpha+31\alpha^2\right) \\ +5St_2^4\left(4-13\alpha+7\alpha^2\right)-(7iSt_2^5+2St_2^6)(\alpha-1)^2 \end{array}\right)}{60St_2^2\alpha^2}\right)$$

APPENDIX E

The transfer function at the first harmonic, defined as $G_{2\omega_o} = \dfrac{A'(2\omega_o)/\overline{A}}{u(\omega_o)'/u_o}$, is:

$$G_{2\omega_o} = \varepsilon \left(\frac{\tilde{A}_{2\omega_o} e^{i\,2K\alpha\,St_2}}{8\alpha(K\alpha-1)^3 St_2^2} + \frac{\tilde{B}_{2\omega_o} e^{i2\,St_2}}{8\alpha(K\alpha-1)^3 St_2^2} + \frac{\tilde{C}_{2\omega_o}\ K\ e^{i\,(K\alpha+1)\,St_2}}{(K\alpha+1)^2(K\alpha-1)^3 St_2^2} + \frac{\tilde{D}_{2\omega_o}}{8\alpha(K\alpha+1)^2 St_2^2} \right) \tag{165}$$

where the coefficients $\tilde{A}_{2\omega o}$ to $\tilde{D}_{2\omega_o}$ for conical flames are given as

$$\begin{aligned}
\tilde{A}_{c,2\omega_o} &= (3-\alpha-2K\alpha) \\
\tilde{B}_{c,2\omega_o} &= (\alpha-3)\alpha^2K^2 + (4-2\alpha(1+iSt_2)+2iSt_2)\alpha K + i2(\alpha-1)(i+St_2) \\
\tilde{C}_{c,2\omega_o} &= (-3+2\alpha+\alpha^2K^2) \\
\tilde{D}_{c,2\omega_o} &= 5-\alpha(3+i2St_2)+i2St_2+K\alpha(3-\alpha(1+i2St_2)+i2St_2)
\end{aligned}$$

The coefficients for wedge flames reduce to:

$$\begin{aligned}
\tilde{A}_{w,\omega_o} &= (-3+\alpha+2K\alpha)(1-i2\alpha KSt_2) \\
\tilde{B}_{w,\omega_o} &= i(\alpha-3)(i+2St_2)\alpha^2K^2 - 2(\alpha-1)(-1+i2St_2+2St_2^2) \\
&\quad + 2\alpha K(-2+\alpha+i4St_2-i2\alpha St_2+2(\alpha-1)St_2^2) \\
\tilde{C}_{w,\omega_o} &= i(-3+2\alpha+\alpha^2K^2)(i+St_2(1+\alpha K)) \\
\tilde{D}_{w,\omega_o} &= -5-3\alpha(K-1)+\alpha^2K
\end{aligned}$$

Note that the response at the first harmonic has three characteristic time scales represented by the terms $2St_2$, $2St_c$ and $(K\alpha+1)St_2 = St_2+St_c$. As discussed in the previous section, boundary conditions are solely responsible for St_2 while flow non-uniformities account for St_c. Similar to the response at the fundamental frequency, there is a single characteristic time scale in the limit of (η=1) represented by the term $2St_2$. In the limit of

(η=1), Eq. (165) reduces to:

$$\lim_{\eta\to 1} G_{c,2\omega_o} = \varepsilon \left(\frac{\begin{array}{l} 3(\alpha-2)(e^{i2St_2}-1)-3i(\alpha-1+(\alpha-3)e^{i2St_2})St_2 \\ +6e^{i2St_2}St_2^2+i2(\alpha-1)e^{i2St_2}St_2^3 \end{array}}{24\alpha St_2^2} \right)$$

$$\lim_{\eta\to 1} G_{w,2\omega_o} = \varepsilon \left(\frac{\begin{array}{l} -3(\alpha-2)(e^{i2St_2}-1)+6(\alpha-2)(i+St_2)e^{i2St_2}St_2 \\ +4St_2^3e^{i2St_2}(i(\alpha+2)-(\alpha-1)St_2^4) \end{array}}{24\alpha St_2^2} \right)$$

For the uniform velocity case (η=0), the transfer functions for conical and wedge flames can be simplified to:

$$\lim_{\eta\to 0} G_{c,2\omega_o} = \varepsilon(\alpha-1)\left(\frac{e^{2i\,St_2}(1-iSt_2)-1-iSt_2}{4St_2^2\alpha} \right) \quad (166)$$

$$\lim_{\eta\to 0} G_{w,2\omega_o} = \varepsilon(\alpha-1)\left(\frac{1+e^{2i\,St_2}(-1+2St_2(i+St_2))}{4St_2^2\alpha} \right) \quad (167)$$

As the flame becomes long (i.e. increase in α), the gain drops considerably.

APPENDIX F

Using the expression for flame shape given by Eq (68), the exact expression for the transfer function can be expressed as:

$$G\left(St_2,\eta,\sigma_c^*,\sigma_s^*\right)=\overbrace{\widetilde{G_S}}^{S_L\ Fluctuation}+\overbrace{\widetilde{G_A}}^{Area\ Fluctuation}$$

$$G_A=\left(i+\eta St_2\ \sigma_s^*\right)\frac{\left(\begin{array}{l}e^{i\,\eta St_2}\left(1+\Lambda-2i\sigma_c^*St_2+2\sigma_c^{*2}\eta^2St_2^2\right)-2\Lambda e^{\frac{1-\Lambda}{2\sigma_c^*}}+\\ e^{i\,\eta St_2-\frac{\Lambda}{\sigma_c^*}}\left(-1+\Lambda+2i\sigma_c^*St_2-2\sigma_c^{*2}\eta^2St_2^2\right)\end{array}\right)}{St_2\ \left(-i+i\eta+\sigma_c^*\eta^2St_2\right)\left(\begin{array}{l}i\left(-1+\Lambda+2i\sigma_c^*St_2\right)e^{\frac{-\Lambda}{\sigma_c^*}}+\\ \left(i+i\Lambda+2\sigma_c^*St_2\right)\end{array}\right)}$$

(168)

$$G_S=\left(e^{i\,\eta St_2}-1\right)\sigma_s^*+\left(i+\sigma_s^*\right)\times$$

$$\frac{\left(\begin{array}{l}\left(1+\Lambda-2i\sigma_c^*St_2\right)\left(-1+\Lambda+2i\eta\sigma_c^*St_2\right)+4\Lambda\eta^2\sigma_c^{*2}St_2^2e^{i\,\eta St_2-\frac{1+\Lambda}{2\sigma_c^*}}-2\eta\sigma_c^*St_2\left(i+(\Lambda+2)\sigma_c^*St_2+\Lambda\left(i+\eta\sigma_c^*St_2\right)\right)e^{i\,\eta St_2}\\ +4i\Lambda\sigma_c^*St_2e^{\frac{1-\Lambda}{2\sigma_c^*}}-2e^{i\,\eta St_2-\frac{\Lambda}{\sigma_c^*}}\eta\sigma_c^*St_2\left(-i-(\Lambda+2)\sigma_c^*St_2+\Lambda\left(i+\eta\sigma_c^*St_2\right)\right)+\left(1+\Lambda-2i\eta\sigma_c^*St_2\right)\left(-1+\Lambda+2i\sigma_c^*St_2\right)e^{-\frac{\Lambda}{\sigma_c^*}}\end{array}\right)}{2St_2\left(-i+i\eta+\sigma_c^*\eta^2St_2\right)\left(\begin{array}{l}i\left(-1+\Lambda+2i\sigma_c^*St_2\right)e^{\frac{-\Lambda}{\sigma_c^*}}+\\ \left(i+i\Lambda+2\sigma_c^*St_2\right)\end{array}\right)}$$

(169)

where

$$\Lambda=\sqrt{1-4i\sigma_cSt_2}$$

APPENDIX G

For the case of axisymmetric flames, the evolution equation for $\hat{\zeta}_1$ (see Eq (35)) with the azimuthal component of stretch included can be expressed as:

$$\frac{\hat{\sigma}_c \beta}{\left(1+\beta^2\right)^{3/2}} \frac{\partial^2 \hat{\zeta}_1}{\partial r^2} + \frac{\beta^2}{1+\beta^2} \frac{\partial \hat{\zeta}_1}{\partial r} + \frac{\beta\, \hat{\sigma}_{c,azim}}{\sqrt{1+\beta^2}} \frac{1}{r} \frac{\partial \zeta_1}{\partial r} + iSt\, \hat{\zeta}_1 + \left(1 - \frac{i\hat{\sigma}_s KSt\beta}{\sqrt{1+\beta^2}}\right) e^{iSt\,\{K(1-r)\}} = 0 \tag{170}$$

An exact solution to the above expression can be obtained in terms of the confluent hypergeometric function and the generalized Laguerre polynomial. However, the expressions are quite complex and not amenable to analytical insight. Considerable simplification can be achieved by neglecting the azimuthal component represented by the $\frac{1}{r}\frac{\partial \zeta_1}{\partial r}$ term in Eq. (170). In the physically interesting case of $\sigma << 1$, the stretch term is only significant at high frequencies wherein the length scale of wrinkling is small – conditions where the second derivative of flame curvature has a much larger value than the first derivative. As such, this azimuthal curvature term is only non-negligible near $r = 0$. However, the portion of flame area near $r=0$ is negligible relative to that contributed by the rest of the flame – as such, although this term will have a significant impact on *flame position* at such points, its affect on *flame area – and thus heat release* – is minimal. Indeed simulations shown in Figure 68 support the above arguments.

So neglecting the azimuthal component, the solution for $\zeta_1(r,t)$ can be expressed as[**]:

[**] For the case of a 2-d wedge flame, the mean flame shape given by Eq. (34) satisfies the governing equation and the boundary conditions exactly. Here we assume the same flame shape for the axisymmetric case as in Eq. (34), which closely describes the actual flame shape with mean curvature effects included except near r=0.

$$\zeta_1(r,t) = Re\left(\frac{e^{-iSt\,t}\left(e^{i\eta St_2(1-r)} - e^{\frac{(1-r)(1-\Lambda)}{2\sigma^*}} \right)}{St\left(i(\eta-1) + \sigma^* \eta^2 St_2 \right)} \right) \tag{171}$$

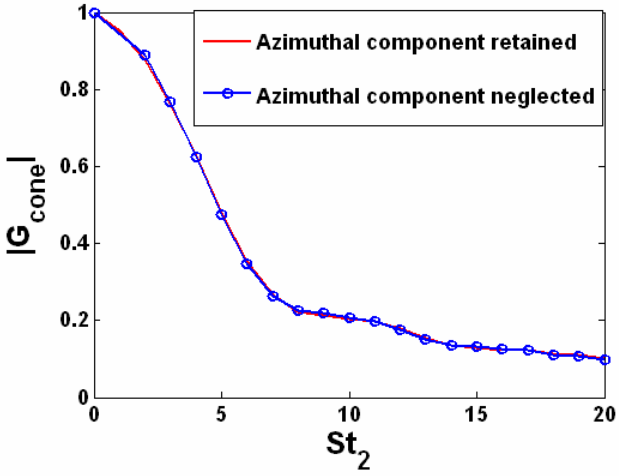

Figure 68 Axisymmetric conical linear transfer function amplitude dependence upon the reduced Strouhal number (St_2) for η=0, σ^*=0.005,β=2

The resulting conical and wedge flame transfer functions can be expressed as:

$$G_c(St_2,\eta,\sigma_c^*,\sigma_s^*) = \underbrace{2\left(i+\eta St_2\ \sigma_s^*\right)\frac{\left(\begin{array}{l} -i(1+\Lambda)(\eta-1)+2\sigma_c^*\eta St_2+2i\Lambda\eta e^{\frac{1-\Lambda}{2\sigma_c^*}} \\ -ie^{i\,\eta St_2}\left(1+\Lambda-i\sigma_c^*(1-\Lambda)\eta^2 St_2\right) \end{array}\right)}{\eta St_2^2\ \ (1+\Lambda)\left(1-\eta+i\sigma_c^*\eta^2 St_2\right)}}_{Area\ Fluctuation}$$

$$+\underbrace{\left(e^{i\,\eta St_2}-1\right)\sigma_s^* + \frac{\left(1-i\eta St_2\ \sigma_s^*\right)\left(-1+\Lambda+2i\sigma_c^*\eta St_2\right)}{2St_2\left(-i+i\eta+\sigma_c^*\eta^2 St_2\right)}}_{S_L\,Fluctuation}$$

$$G_w(St_2,\eta,\sigma^*) = \underbrace{2\left(i+\eta St_2\ \sigma_s^*\right)\frac{\left(\begin{array}{l} e^{i\,\eta St_2}\left((1+\Lambda)(1-i\eta St_2)-2i\sigma_c^* St_2+\sigma_c^*\eta St_2^2(-2+\sigma_c^*(1-\Lambda)\eta^2\right) \\ -2i\sigma_c^{*2}\eta^3 St_2^3\Big)+2i\Lambda\eta e^{\frac{1-\Lambda}{2\sigma_c^*}}\left(\sigma_c^* St_2+(i+St_2)\right)+\big((1+\Lambda)(\eta-1) \\ -i\sigma_c^* St_2(\Lambda\eta-2+3\eta)\big) \end{array}\right)}{\eta St_2^2\ \left((\eta-1)-i\eta^2 St_2\sigma^*\right)\left(1+\Lambda-2iSt_2\sigma^*\right)}}_{Area\ Fluctuation}$$

$$+\underbrace{\left(e^{i\,\eta St_2}-1\right)\sigma_s^* + \frac{\left(i+\eta St_2\ \sigma_s^*\right)\sigma_c^*\left(\begin{array}{l}(1+\Lambda)(\eta-1)-2i\sigma_c^*\eta St_2+2\Lambda e^{\frac{1-\Lambda}{2\sigma_c^*}} \\ +i\eta e^{i\,\eta St_2}\left(i+(\eta+2)\sigma_c^* St_2+\Lambda\left(i+\sigma_c^*\eta St_2\right)\right)\end{array}\right)}{\left(-i+i\eta+\sigma_c^*\eta^2 St_2\right)\left(1+\Lambda-2i\sigma_c^* St_2\right)}}_{S_L\ Fluctuation}$$

REFERENCES

[1] Broda, J. C., Seo, S., Santoro, R. J., Shirhattikar, G. & Yang, V., "An Experimental Study of Combustion Dynamics of a Premixed Swirl Injector", *Proc. Comb. Inst.* **27**: (1998) 1849-1856.

[2] Candel, S., "Combustion Dynamics and Control: Progress and Challenges", *Proc. Comb. Inst* **29** (2002) 1-28.

[3] Dowling, A. P. & Stow, S. R., "Acoustic Analysis of Gas Turbine Combustors", *J. Prop. Power* **19**(5) (2003) 751-764.

[4] Ducruix, S., Schuller, T., Durox, D. & Candel, S. M., "Combustion Dynamics and Instabilities- Elementary Coupling and Driving Mechanisms", *J. Prop. Power* **19**(5) (2003) 722-734

[5] Paschereit, C. O., Gutmark, E. & Weisenstein, W., "Control of Thermo-Acoustic Instabilities and Emissions in an Industrial Type Gas Turbine Combustor", *Proc. Comb. Inst.* **27** (1998) 1817-1824

[6] Rayleigh, J.S.W., *The Theory of Sound*, Vol. 2, New York, 1945.

[7] Lieuwen, T., "Modeling Premixed Combustion- Acoustic Wave Interactions: A Review ", *J. Prop. Power* **19**(5) (2003) 765-781.

[8] Dowling, A. P., "Nonlinear Self-Excited Oscillations of a Ducted Flame", *J. Fluid Mech* **346**: (1997) 271-290.

[9] Bellows, B., Zhang, Q., Neumeier, Y., Lieuwen, T. & Zinn, B. T., "Forced Response Studies of a Premixed Flame to Flow Disturbances in a Gas Turbine Combustor", *AIAA*.# 2003-0824.

[10] Lee, J. G. & Santavicca, D. A., "Experimental Diagnostics for the Study of Combustion Instabilities in Lean Premixed Combustors", *J. Prop. Power* **19**(5) (2003) 735-750.

[11] Lieuwen, T. & Neumeier, Y., "Nonlinear Pressure-Heat Release Transfer Function Measurements in a Premixed Combustor", *Proc. Comb. Inst.* **29**(1): (2002) 99-105.

[12] Poinsot, T. & Candel, S., "A Nonlinear Model for Ducted Flame Combustion Instabilities", *Comb. Sci. Tech.* **61**.(1988) 121-153

[13] Keller, D. & Peters, N., "Transient Pressure Effects in the Evolution Equation for Premixed Flame Fronts", *Theoret. Comput. Fluid Dynamics* **6** (1994) 141-159

[14] McIntosh, A. C., "Deflagration Fronts and Compressibility", *Phil. Trans. R. Soc. Lond. A.* **357** (1999) 3523-3538.

[15] Peters, N. & Ludford, "The Effect of Pressure Variations on Premixed Flames", G. S. S., *Comb. Sci. Tech.* **34** (1983) 331-344.

[16] Van Harten, A., Kapila, A. & Matkowsky, B. J., "Acoustic Coupling of Flames", *SIAM J. Appl. Math.* **44**(5) (1984) 982-995.

[17] Dowling, A. P., "A Kinematic Model of a Ducted Flame", *J. Fluid Mech.* **394** (1999): 51-72.

[18] Peracchio, A. A. & Proscia, W. M., "Nonlinear Heat Release/Acoustic Model for Thermoacoustic Instability in Lean Premixed Combustors", *ASME. paper* # 98-GT-269

[19] Straub, D. L. & Richards, G. A., "Effect of Fuel Nozzle Configuration on Premix Combustion Dynamics", *ASME. paper* # 98-GT-492

[20] Baillot, F., Durox, D. & Prud'homme, R., "Experimental and Theoretical Study of a Premixed Vibrating Flame", *Comb. Flame* **88**(2) (1992) 149-168.

[21] Lieuwen, T., "Nonlinear Kinematic Response of Premixed Flames to Harmonic Velocity Disturbances", *Proc. Comb. Inst.* **30**(2) (2005) 1725-1732.

[22] Stow, S.R., Dowling, A.P., "Low-Order Modelling of Thermoacoustic Limit Cycles", *ASME paper #GT2004-54245*, 2004.

[23] Durox, D., Schuller, T. & Candel, S., "Combustion Dynamics of Inverted Conical Flames", *Proc. Comb. Inst* **30** (2005) 1717-1724.

[24] Bourehla, A. & Baillot, F., "Appearance and Stability of a Laminar Conical Premixed Flame Subjected to an Acoustic Perturbation", *Comb. Flame* **114**(3-4) (1998): 303-318

[25] Durox, D., Baillot, F., Searby, G. & Boyer, L., "On the Shape of Flames under Strong Acoustic Forcing: a Mean Flow Controlled by an Oscillating Flow", *J. Fluid Mech.* **350** (1997) 295-310.

[26] Baillot, F., Bourehla, A. & Durox, D., "The Characteristics Method and Cusped Flame Fronts", *Comb. Sci Tech.* **112** (1996) 327-350.

[27] Blackshear, P. L., "Driving Standing Waves by Heat Addition", *Proc. Comb. Symp.* **4** (1953) 553-566.

[28] Birbaud, A.L., Durox, D., Candel, S., "Upstream Flow Dynamics of a Laminar Premixed Conical Flame Submitted to Acoustic Modulations", *Comb. Flame* **146**(3) (2006) 541-552.

[29] Birbaud, A.L., Durox, D., Ducruix, S. & Candel, S., "Dynamics of Confined Premixed Flames Submitted to Upstream Acoustic Modulations", *Proc. Comb. Inst* **31** (2007) 1257-1265.

[30] Markstein, G. H., *Nonsteady flame Propagation*, Pergamon (1964)

[31] Marble, F. E. & Candel, S. M., "An Analytical Study of the Non-steady Behavior of Large Combustors", *Proc. Comb. Inst.* **17** (1978) 761-769.

[32] Matalon, M. & Matkowsky, B., "Flames as Gasdynamic Discontinuities", *J. Fluid Mech.* **124** (1982) 239-260.

[33] Subbaiah, M. V., "Nonsteady Flame Spreading in Two-dimensional Ducts", *AIAA* **21**(11) (1983) 1557-1564.

[34] Ducruix, S., Durox, D. & Candel, S., "Theoretical and Experimental Determinations of the Transfer Function of a Laminar Premixed Flame", *Proc. Comb. Inst* **28** (2000) 765-773.

[35] Schuller, T., Durox, D. & Candel, S., "A Unified Model for the Prediction of Laminar Flame Transfer Functions-Comparisons between Conical and V-Flame Dynamics", *Comb. Flame* **134**(1-2) (2003) 21-34.

[36] Clanet, C., Searby, G. & Clavin, P., "Primary Acoustic Instability of Flames Propagating in Tubes - Cases of Spray and Premixed Gas Combustion", *J. Fluid Mech.* **385** (1999) 157-197.

[37] Cho, J. H. & Lieuwen, T., "Laminar Premixed Flame Response to Equivalence Ratio Oscillations", *Comb. Flame* **140**(1) (2005) 116-129.

[38] Lieuwen, T., "Theoretical Investigation of Unsteady Flow Interactions with a Premixed Planar Flame", *J. Fluid Mech.* **435** (2001) 289-303.

[39] Lee, D. H. & Lieuwen, T., "Premixed Flame Kinematics in a Longitudinal Acoustic Field", *J. Prop. Power* **19**(5) (2003) 837-846.

[40] Fleifel, M., Annaswamy, A. M., Ghoniem, Z. A. & Ghoniem, A. F., "Response of a Laminar Premixed Flame to Flow Oscillations: A Kinematic Model and Thermoacoustic

Instability Results", *Comb. Flame* **106**: 487-510.

[41] Lee, D. H. & Lieuwen, T., "Acoustic Near-field Characteristics of a Conical Premixed Flame", *J. Acoust. Soc. Am.* **113**(1) (2003) 167-177.

[42] Michalke, A., "Instability of a Compressible Circular Jet Considering the Influence of the Thickness of the Jet Boundary Layer", *Z. Flugwiss.(in German)* **19** (1971).

[43] Bechert, D. & Pfizenmaier, E., "On Wavelike Perturbations in a Free Jet Travelling Faster than the Mean Flow in the Jet", *J. Fluid Mech.* **72** (1975) 341-352.

[44] Ferguson, D., Richards, G., Woodruff, S., Bernal, S. & Gautam, M., "Effect of Surface Area Variation on Heat Release Rates in Premixed Flames", *Proc. 2nd Joint Meeting U.S. Sections Comb. Inst.* (2001)

[45] Hubbard, S. and Dowling, A.P., "Acoustic Instabilities in Premix Burners", *AIAA Paper* # 98-2272

[46] Rajaram, R. & Lieuwen, T., "Parametric Studies of Acoustic Radiation from Premixed Flames", *Combust. Sci. Technol.* **175**, (2003) 2269-2298.

[47] Preetham, Thumuluru, S.K. & Lieuwen, T., "Linear Response of Premixed Flames to Flow Oscillations: Unsteady Stretch Effects", *AIAA Paper* # 2007-0176

[48] Kuramoto, Y. & Tsuzuki, T., "On the Formation of Dissipative Structures in Reaction-Diffusion Systems -Reductive Perturbation Approach", *Prog. Theo. Phys* **54**(3) (1975) 687-699.

[49] Sivashinsky, G. I., "Instabilities, Pattern Formation and Turbulence in Flames", *Ann. Rev. Fluid Mech* **15** (1983) 179-199

[50] Searby, G. & Clavin, P., "Weakly Turbulent, Wrinkled Flames in Premixed Gases", *Comb. Sci. Tech.* **46**(3-6) (1986) 167-193.

[51] Searby, G. & Rochwerger, D., "A Parametric Acoustic Instability in Premixed Flames", *J. Fluid Mech.* **231** (1991) 529-543

[52] Vaezi, V. & Aldredge, R., "Premixed Flame Propagation in Turbulent Taylor-Couette Flow", *Comb. Flame* **121** (2000) 356-366

[53] Bychkov, V., "Analytical Scalings for Flame Interaction with Sound Waves", *Phys. Fluids* **11**(10) (1999) 3168-3173

[54] S.H. Chung & C.K. Law, "An Integral Analysis of the Structure and Propagation of Stretched Premixed Flames", *Combust. Flame* 72 (1988) 325-336.

[55] Jiang, G. & Peng, D., "Weighted ENO Schemes for Hamilton-Jacobi Equations", *SIAM J. Sci. Comput.* **21** (2000) 2126-2143.

[56] Gottlieb, S. & Shu, C., "Total Variation Diminishing Runge-Kutta Schemes", *Math. Comput.* **67**: (1998) 73-85.

[57] Wicker, J. M., Greene, W. D., Kim, S. & Yang, V., "Triggering of Longitudinal Combustion Instabilities in Rocket Motors- Nonlinear Combustion response", *J. Prop. Power* **12**(6) (1996).

[58] Joulin, G., "On The Response of Premixed Flames to Time-Dependent Stretch and Curvature", *Combust. Sci. and Tech.*, **97** (1994) 219-229.

[59] Fedkiw, R. P., Merriman, B & Osher, S., "Simplified Discretization of Systems of Hyperbolic Conservation Laws Containing Advection Equations", *J. Comput. Phys*, **157**, (2000) 302-326.

[60] Fedkiw, R. P., Aslam. T., Merriman., B. & Osher, S., "A Non-oscillatory Eulerian Approach to Interfaces in Multimaterial Flows (the Ghost Fluid Method)", *J. Comput. Phys*, **152**, (1999) 457-492.

[61] Fedkiw, R. P., Aslam. T. & Xu, S., "The Ghost Fluid Method for Deflagration and Detonation Discontinuities", *J. Comput. Phys*, **154**, (1999) 393-427.

[62] Sussman, M., Smereka, P. & Osher, "A Level Set Method for Computing Solutions to Incompressible Two-phase Flow", S., *J. Comput. Phys*, **114**, (1994) 146-159.

[63] Rastigejev, Y. & Matalon, M., "Nonlinear Evolution of Hydrodynamically Unstable Premixed Flames", *J. Fluid Mech.* **554,** (2006) 371-392.

[64] Schmidt, H. & Klein, R., "A Generalized Level-set/in-cell-reconstruction Approach for Accelerating Turbulent Premixed Flames", *Combust. Theory Modeling,* **7**, (2003) 243-267.

[65] Jiang, G. S. & Shu, C. W., "Efficient Implementation of Weighted ENO Schemes", *J. Comput. Phys*, **126**, (1996) 202-228.

[66] Harten, A., Engquist, B., Osher, S. & Chakravarthy, S., "Uniformly High Order Essentially Non-oscillatory Schemes", *J. Comput. Phys*, **71**, (1987) 231-303.

[67] Shu, C. W., & Osher, S., "Efficient Implementation of Essentially Non-oscillatory Shock-wave Schemes", *J. Comput. Phys*, **83**, (1989) 32-78

[68] Adams, N. & Shariff, K., "A High-Resolution Hybrid Compact-ENO Scheme for Shock-Turbulence Interaction Problems", *J. Comput. Phys*, **127**, (1996) 27-51

[69] Roe, P. L., "Approximate Riemann Solvers, Parameter Vectors and Difference Schemes", *J. Comput. Phys*, **43**, (1981) 357-372.

[70] Santosh, H., Preetham & Lieuwen, T., "Response of Turbulent Premixed Flames to Harmonic Acoustic Forcing", T. C., *Proc. Comb. Inst.*, **31** (2007) 1427-1434.

[71] Peng, D., Merriman, B., Osher, S., Zhao, H. & Kang, M., "A PDE-based fast local level set method', *J. Comput. Phys*, **155** (1999) 410-438.

[72] Smereka, P., "The Numerical Approximation of a Delta Function with Application to Level Set Methods", *J. Comput. Phys*, **211** (2006) 77-90.

[73] Smiljanovski, V., Moser, V., & Klein, R., "A Capturing-Tracking Hybrid Scheme for Deflagration Discontinuities", *Combust. Theory Modeling,* **1**, (1997) 183-215.

[74] Poinsot, T. & Lele,S., "Boundary Conditions for Direct Numerical Simulations of Compressible Viscous Flows", *J. Comput. Phys*, **101** (1992) 104-129.

[75] Shu, C. W., "High-order Finite Difference and Finite Volume WENO Schemes and Discontinuous Galerkin Methods for CFD", *Int. J. Comput. Fluid Dynam.*, **17** (2) (2003) 107-118.

[76] Bychkov, V. V. & Liberman, M.A., "Dynamics and Stability of Premixed Flames", *Physics Reports*, **325** (2000) 115 - 237.